Dissertation

Development of Automated Phase Transition Path Search Method for Systematically Predicting Structures and Properties of Crystal

(結晶構造とその物性の系統的予測へ向けた
相転移経路自動探索法の開発)

Makito Takagi

Hokkaido University

2019

Contents

Chapter 1.
General introduction

Properties of materials depend on their composition and their crystal structure. For example, graphite and *h*-BN are isoelectronic structures and have a similar layered structure that build from six membered rings. Even though graphite is a conductor, *h*-BN is an insulator. Furthermore, graphite and diamond are composed only of carbon atoms, but their properties are dramatically different because their crystal structure is different. In recent years, not only from experiments, but also attention is focused on predicting the crystal structure and phase transition route by calculation and efficiently developing materials.

In order to calculate the materials (crystals and surface), a modeling is necessary because the system is semi-infinitely spread. For this purpose, the following two methods are mainstream; (i) Periodic boundary conditions (PBCs) can represent an infinite system that repeats the unit structure periodically and is one of the ideal calculation method. In order to describe the localized structure or reaction with PBCs calculation cost is high because it is necessary to use a large unit structure. (ii) A cluster model that extracts a finite number of atoms by assuming the locality of the structure or the reaction. To describe a crystal structure that delocalized in general, the calculation cost is high because it is necessary to deal with a very large number of atoms. In this study, PBCs are adopted because crystal structures are focused.

In this context, crystal structure prediction from first principles has become one of active fields in materials science.[1-7] Until now, various methods have been developed.[8-28] For example, graph,[8-15] simulated annealing,[16] grid search,[17] molecular dynamics,[18-19] evolutionary algorithm,[20-22] minima hopping,[23] particle swarm optimization algorithm,[24] MAC algorithm,[25] etc. have been successfully employed in crystal structure prediction. Methods based on data mining and/or ranking[26-28] approaches have also been proposed recently.

To treat the phase-transition, nudged elastic band (NEB) method[29] and molecular dynamics (MD) simulation[30] were commonly used. In the case of NEB method, the calculator has to specify the start point and the end point, then the path between the start point and the end point is obtained. In the case of an unknown system that the calculator could not specify the start point and the end point, it is difficult to

apply the NEB method. There is also a danger of overlooking the route which the calculator did not expect. In the case of MD simulations, there is a limit on the time scale that can be treated. So that it is difficult to deal with systems that include various time scales.

Recently, anharmonic downward distortion following (ADDF) method[31] and artificial force induced reaction (AFIR) method[32] have been develop by Maeda *et. al*. ADDF method is an efficient method for searching the isomers and reaction paths by following the anharmonic downward distortion on the potential energy surface (PES). AFIR method is also an efficient method for searching the isomers and reaction paths by just optimized on the model function that assumed pushes fragments A and B together or pull them apart. The minimization path of this function, termed the AFIR path, is a good approximation of the reaction path of the corresponding structural rearrangement. Although the first-order saddle point along the path can also be determined by geometry optimization starting from the highest energy point along the AFIR path. Systematic search can be realized by applying the both of ADDF method and AFIR method continuously to the obtained structures. However, these methods could not be applied to periodic system such as crystals and surfaces, because these methods are developed for the molecular systems. In this study, AFIR method is used because ADDF method frequently requires to Hessian calculation that high cost for periodic systems.

I thought an efficient crystal structure search and phase-transition path search are realized by using AFIR method. Merits of crystal structure search and phase-transition path search by AFIR method are bellow; Initial structure guess by the calculator is not required by exhaustive search. A Hessian calculation is not required during search. A good convergence of SCF is also expected by the search along the reaction paths. Not only structures but also the reaction paths can be obtained and there is no limitation about the timescale.

A discussion of the kinetic stability of molecules has become possible in recent years[33] by exhaustively searching reaction paths. A discussion of the luminous property of molecules is also has become possible by searching the all accessible crossing point on the PES[34]. It is difficult to discuss with PBCs such a properties since it was difficult to exhaustive search for crystal structures and reaction paths. So the stability of the material remained based on thermodynamic stability and phonon

calculation. It was also difficult to discuss whether the material can be luminescent or not, and it was only discussed the luminescent color based on HOMO - LUMO gap. I thought by combining the AFIR method and PBCs, such discussion about such properties is also realized.

In this study, AFIR method is extended to PBCs (PBC/AFIR method) and its applications were performed.

In **Chapter 2**, development of PBC/AFIR method and applications to search crystal structure and two- or one-dimensional periodic structures are proposed and applied to the well-known system C_8/unit-cell with the slab model.

In **Chapter 3**, a database of small carbon crystal (C_1-C_{16}/unit-cell) including their properties (density, sp^2/sp^3 ratio and band gap) is built by using PBC/AFIR method and some interesting structures are picked up from the database.

In **Chapter 4**, the PBC/AFIR method was applied to not only crystal structure search but also, global Phase-transition Route Mapping. An application to C_4/unit-cell was shown.

In **Chapter 5**, the kinetic stability of Cco-C_8 (*Z*-carbon), which predicted theoretically but still not synthesized, was discussed by PBC/AFIR method.

In **Chapter 6**, intersystem crossing pathways in the benzene crystal was discussed by combining PBC/AFIR method with Gradient Projection (GP) method which general method of searching energy crossing region on the PESs.

In **Chapter 7**, general conclusion, this study is summarized finally.

REFERENCE

[1] J. Maddox, Nature **335**, 201 (1988).

[2] R. Martoňák, A. R. Oganov, and C. W. Glass, Phase Transitions **80**, 277 (2007).

[3] S. M. Woodley, and R. Catlow, Nat. Mater. **7**, 937 (2008) .

[4] G. M. Day, T. G. Cooper, A. J. Cruz-Cabeza, K. E. Hejczyk, H. L. Ammon, S. X. M. Boerrigter, J. S. Tan, R. G. Della Valle, E. Venuti, J. Jose, S. R. Gadre, G. R. Desiraju, T. S. Thakur, B. P. van Eijck, J. C. Facelli, V. E. Bazterra, M. B. Ferraro, D. W. M. Hofmann, M. A. Neumann, F. J. J. Leusen, J. Kendrick, S. L. Price, A. J. Misquitta, P. G. Karamertzanis, G. W. A. Welch, H. A. Scheraga, Y. A. Arnautova, M. U. Schmidt, J. van de Streek, A. K. Wolf, and B. Schweizer, Acta. Cryst. **B65**, 107 (2009).

[5] A. R. Oganov, Modern methods of crystal structure prediction. John Wiley & Sons (2011).

[6] Y. Wang and Y. Ma, J. Chem. Phys. **140**, 040901 (2014).

[7] T. Gu, W. Luo, and H. Xiang, WIREs Comput. Mol. Sci. (2016). doi: 10.1002/wcms.1295.

[8] A. F. Wells, Acta Cryst. **7**, 535 (1954).

[9] A. Wells, Three-Dimensional Nets and Polyhedra, Wiley, (1977).

[10] A. F. Wells, Am. Math. Soc. **84**, 446 (1978).

[11] M. V. Nikerov, D. A. Bochvar, and I. V. Stankevich, J. Struct. Chem. **23**, 150 (1982).

[12] A. T. Balaban, J. Chem. Inform. Comput. Sci. **35**, 339 (1995).

[13] M. J. Bucknum, and E. A. Castro, Solid State Sci. **10**, 1245 (2008).

[14] M. O'keeffe, M. A. Peskov, S. J. Ramsden, and O. M. Yaghi, ACCOUNTS OF CHEMICAL RESEARCH, **41**, 1782 (2008).

[15] O. D. Friedrichs, M. O'Keeffe, and O. M. Yaghi, Acta Cryst. **A59**, 22 (2003).

[16] M. W. Deem and J. M. Newsam, Nature **342**, 260 (1989).

[17] J. R. Holden, Z. Y. Du, and H. L. Ammon, J. Comput. Chem. **14**, 422 (1993).

[18] R. Martoňák, A. Laio, and M. Parrinello, Phys. Rev. Lett. **90**, 075503 (2003).

[19] E. Zurek and W. Grochala, Phys. Chem. Chem. Phys. **17**, 2917 (2015).

[20] A. R. Oganov and C. W. Glass, J. Chem. Phys. **124**, 244704 (2006).

[21] A. R. Oganov and C. W. Glass, J. Phys.: Condens. Matter **20**, 064210 (2008).

[22] S. Bahmann, J. Kortus, Comput. Phys. Commun. **184**, 1618 (2013).

[23] M. Amsler, and S. Goedecker, J. Chem. Phys. **133**, 224104 (2010).

[24] Y. Wang, J. Lv, L. Zhu, and Y. Ma, Phys. Rev. B **82**, 094116 (2010).

[25] Z.-L. Liu, Comput. Phys. Commun. **185**, 1893 (2014).

[26] C. C. Fischer, K. J. Tibbetts, Nat. Mater. **5**, 641 (2006).

[27] K. Sanderson, Nature **450**, 771 (2007).

[28] M. A. Neumann, F. J. J. Leusen, and J. Kendrick, Angew. Chem. Int. Ed. **47**, 2427 (2008).

[29] D. Sheppard, P. H. Xiao, W. Chemelewski, D. D. Johnson, and G. Henkelman, J. Chem. Phys. **136**, 8, 074103 (2012).

[30] M. Iannuzzi, A. Laio, and M. Parrinello, Phys. Rev. Lett. **90**, 4, 238302 (2003).

[31] S. Maeda, T. Taketsugu, K. Morokuma, K. Ohno, Bull. Chem. Soc. Jpn., **87**, 1315 (2014).

[32] S. Maeda, Y. Harabuchi, M. Takagi, K. Saita, K. Suzuki, T. Ichino, Y. Sumiya, K. Sugiyama, and Y. Ono, J. Comput. Chem., **39**, 233 (2018).

[33] Y. Sumiya and S. Maeda, Chem. Eur. J. **24**, 12264 (2018).

[34] Y. Harabuchi, T. Taketsugu, and S. Maeda, Phys. Chem. Chem. Phys. 17, 22561 (2015).

Chapter 2.
Global search for low-lying crystal structures using the artificial force induced reaction method: A case study on carbon

Abstract: We propose a novel approach to perform the global search for low-lying crystal structures from first principles, by combining the artificial force induced reaction (AFIR) method and the periodic boundary conditions (PBCs). The AFIR method has been applied extensively to molecular systems to elucidate the mechanism of chemical reactions such as homogeneous catalysis. The present PBC/AFIR approach found 274 local minima for carbon crystals in the C_8/unit-cell described by the GGA/PBE functional. Among many newly predicted structures, three low-lying structures, which exhibit somewhat higher energy compared with those previously predicted, such as Cco-C_8 (*Z*-carbon) and *M*-carbon, are further discussed with calculations of phonon and band dispersion curves. Furthermore, approaches to systematically explore two- or one-dimensional periodic structures are proposed and applied to the C_8/unit-cell with the slab model. These results suggest that the present approach is highly promising for predicting crystal structures.

2-1. INTRODUCTION

Properties of materials depend not only on their composition but also on their crystal structure. Different crystal structures are formed depending on the generation conditions. For example, carbon can take various forms,[1] such as diamond, graphite, lonsdaleite (hexagonal diamond), fullerene, carbon nanotube (CNT), graphene, graphene nanoribbon (GNR), and so on. Furthermore, many stable structures have been predicted theoretically. *M*-carbon,[2,3] Cco-C_8 (or *Z*-carbon[4,5]), and so forth have been predicted recently from first principles. About 500 different structures have already been registered to the Samara carbon allotrope database (SACADA),[6] and there has been a debate regarding how to handle newly predicted structures.[7,8] Two- or one-dimensional periodic structures, such as graphene and CNT, have also attracted attention as novel materials and catalysts.

In this context, the crystal structure prediction from first principles has become one of the active fields in materials science. To date, various methods have been developed.[9-12] Methods for the searching of two-dimensional periodic structures have also been proposed.[13] In one sense, the crystal structure prediction is to find the most stable structure of a given atomic composition. Finding only the most stable structure would be easy in a small system like C_8 in which the number of atoms in the unit-cell is only 8. Development of methods that can find the lowest energy structure in more complex systems therefore is an important research direction. On the other hand, there would be another direction; that is to exhaustively enumerate possible low-lying structures of a given atomic composition. This still is not a trivial task even in a small system like C_8/unit-cell which is the focus of the present study.

In this study, we combined the artificial force induced reaction (AFIR)[14-16] method with the periodic boundary conditions (PBCs). The AFIR method has previously been employed extensively in automated exploration of structures and reaction pathways in molecular systems such as homogeneous catalysis.[17] The present extension enables the exhaustive search for low-lying crystal structures by the AFIR method. As a case study, crystal structures of carbon described by the C_8/unit-cell were explored by the PBC version of the AFIR method. The search generated 274 local minimum (MIN) crystal structures starting from a single initial structure. The obtained extensive structural database includes not only known structures but also many unreported structures. Additional implementations for the exploration of two- or

one-dimensional periodic structures with the slab model were also introduced and applied to carbon in the C_8/unit-cell. The search yielded 122 and 49 local minimum structures for the two- and one-dimensional periodic systems, respectively. These results demonstrate the usefulness of the present approach in a systematic exploration of unknown crystal structures from first principles.

2-2. METHOD

2-2-1. AFIR method

The AFIR method pushes fragments A and B together or pulls them apart to induce a structural rearrangement. In **Fig. 2-1**, a schematic of the AFIR method is shown. The product can be reached easily simply by minimizing a model function, termed the AFIR function (dotted curve), which is composed of the potential energy surface (PES) and the force term (for the form of the force term, see ref. 14). As demonstrated previously,[14-16] the minimization path of this function, termed the AFIR path, is a good approximation of the reaction path of the corresponding structural rearrangement. Although the first-order saddle point along the path can also be determined by geometry optimization starting from the highest energy point along the AFIR path, the saddle point optimization was not performed in this study because the present purpose was to explore MIN structures. In this study, the model collision energy parameter γ, which defines the strength of the artificial force,[14] was set to a sufficiently large value, i.e., 1000.0 kJ/mol, so as not to limit the search area.

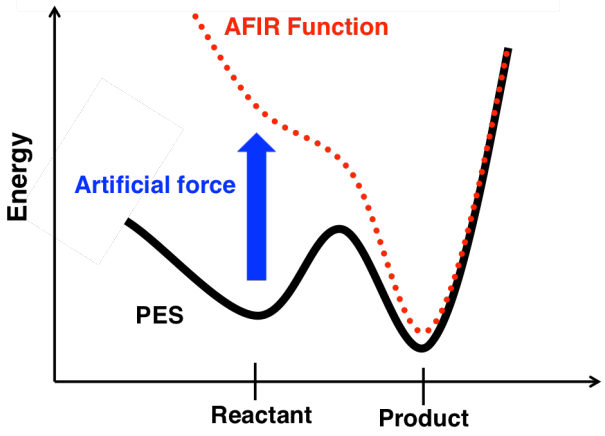

Figure. 2-1. A schematic of the AFIR method. Starting from the reactant region, the

product region can be easily found by minimizing the AFIR function (dotted curve), which is composed of the PES and the force term (for the form of the force term, see ref. 14). By repeating the minimization of the AFIR function with systematically generated different force terms, it is possible to obtain many different products starting from a given initial structure.

There are two modes in the AFIR method, i.e., the multicomponent mode (MC-AFIR) and the single-component mode (SC-AFIR). The MC-AFIR was not described in this study because it has been employed in the exploration of pathways of bimolecular or multicomponent reactions.[14,16] In the SC-AFIR, fragments A and B were systematically defined in a given structure. The AFIR path was then computed for all the automatically defined fragment pairs. The systematic procedure to generate fragment pairs has been described in our previous reports.[15,16] The force term with a given γ is uniquely determined at any structure when the fragment pair is defined. By computing AFIR paths for different fragment pairs, various pathways that depart from the initial structure and lead to new MINs can be obtained. Further applications of the same procedure to newly obtained MINs produce many more structures.

By applying the SC-AFIR to all obtained MINs, a full network of reaction pathways in the PES area accessible by a given γ can be generated. Though such an exhaustive search can be highly demanding, some limiting search options are also available. Two such options have mainly been employed previously: a stochastic search targeted to low-energy structures and a restricted search targeted to structures having a specified chemical bond connectivity. The stochastic search option was adopted in this study to efficiently search for low-lying crystal structures, where the model temperature parameter T_R,[16] which determines how frequently high-energy MINs are chosen, was set to a very large value of 10000.0 K to explore a wide variety of structures. In the stochastic search, the calculation was terminated if the last P AFIR paths did not update the set of lowest M MINs. In this study, M and P were set to f and $3f$, respectively, where f is the number of internal degrees of freedom defined below.

2-2-2. Internal degrees of freedom

The PBCs are used to describe periodic systems. In the search of three-dimensional crystal structures, Cartesian coordinates of three translation vectors (TVs) and all N atoms in the unit-cell, i.e., $3N + 9$ Cartesian coordinates, were considered as variables. In each optimization step, a set of $3N + 3$ orthonormal vectors was defined, by eliminating 3 modes for the translational motions of all atoms along the x-, y-, and z-axes and 3 modes for the rotational motions of the whole system around the x-, y-, and z-axes from the $3N + 9$ Cartesian coordinates. Then, geometrical displacements were invoked in the $3N + 3$ dimensional hyperspace, since neither the three translational motions of all atoms nor the three rotational motions of the whole system changed the total energy of a system without any external field.

In the case where two-dimensional periodic structures were searched, one TV was fixed on the z-axis and the other two TVs were restricted on the xy-plane. In other words, the x and y coordinates of the two TVs and all N atoms in the unit-cell, i.e., $3N + 4$ Cartesian coordinates, were considered as variables. In this study, the length of the TV fixed on the z-axis was set to 20.0 Å. In each optimization step, a set of $3N$ orthonormal vectors was defined, by eliminating 3 modes for the translational motions of all atoms along the x-, y-, and z-axes and 1 mode for a rotational motion of the whole system around the z-axis from the $3N + 4$ Cartesian coordinates. Then, geometrical displacements were invoked in the $3N$ dimensional hyperspace.

In the case where one-dimensional periodic structures were searched, two TVs were fixed on the z- and y-axes, respectively, and the remaining TV was restricted on the x-axis. Hence, the x coordinate of one TV and all N atoms in the unit-cell, i.e., $3N + 1$ Cartesian coordinates, were considered as variables. In this study, the lengths of the two TVs fixed on the y- and z-axes were both set to 20.0 Å. In each optimization step, a set of $3N - 3$ orthonormal vectors was defined, by eliminating 3 modes for the translational motions of all atoms along the x-, y-, and z-axes and 1 mode for a rotational motion of the whole system around the x-axis from the $3N + 1$ Cartesian coordinates. Then, geometrical displacements were invoked in the $3N - 3$ dimensional hyperspace.

Many electronic structure calculation programs provide the force acting on atoms in the unit-cell and the stress tensor acting on the unit-cell. To perform the search in the

abovementioned coordinate system, the first-derivative of the total energy for TVs, i.e., $\partial E/\partial h$, is required. In this study, $\partial E/\partial h$ was obtained with the following equation

$$\left.\frac{\partial E}{\partial \mathbf{h}}\right|_{\mathbf{h}_0} = -V_0 \sigma^t \mathbf{h}_0^{-1}, \quad (1)$$

where E is the potential energy, $\mathbf{h}$ is the unit-cell, $\mathbf{h}_0$ is the unit cell with which the stress is calculated., V_0 is the volume of the unit-cell, and $\boldsymbol{\sigma}$ is the stress tensor..

2-2-3. SC-AFIR method with PBCs

In the conventional SC-AFIR, fragments A and B that are composed of several atoms in a given molecular system are pushed together or pulled apart by minimizing the AFIR function, as illustrated in **Fig. 2-2 (a)** and **(b)**. In the present implementation, a similar procedure was applied to the atoms in the unit-cell, where atoms in fragments A and B were pushed together or pulled apart as depicted in **Fig. 2-2 (c)** and **(d)**, respectively. The algorithm to define fragments automatically was exactly the same as that proposed previously for molecular systems.[15,16] In addition, assuming that there were dummy atoms at the origin and also at the positions of TVs, a pair of dummy atoms were also pushed together or pulled apart as illustrated in **Fig. 2-2 (e)** and **(f)**, to consider the deformation of the unit-cell.

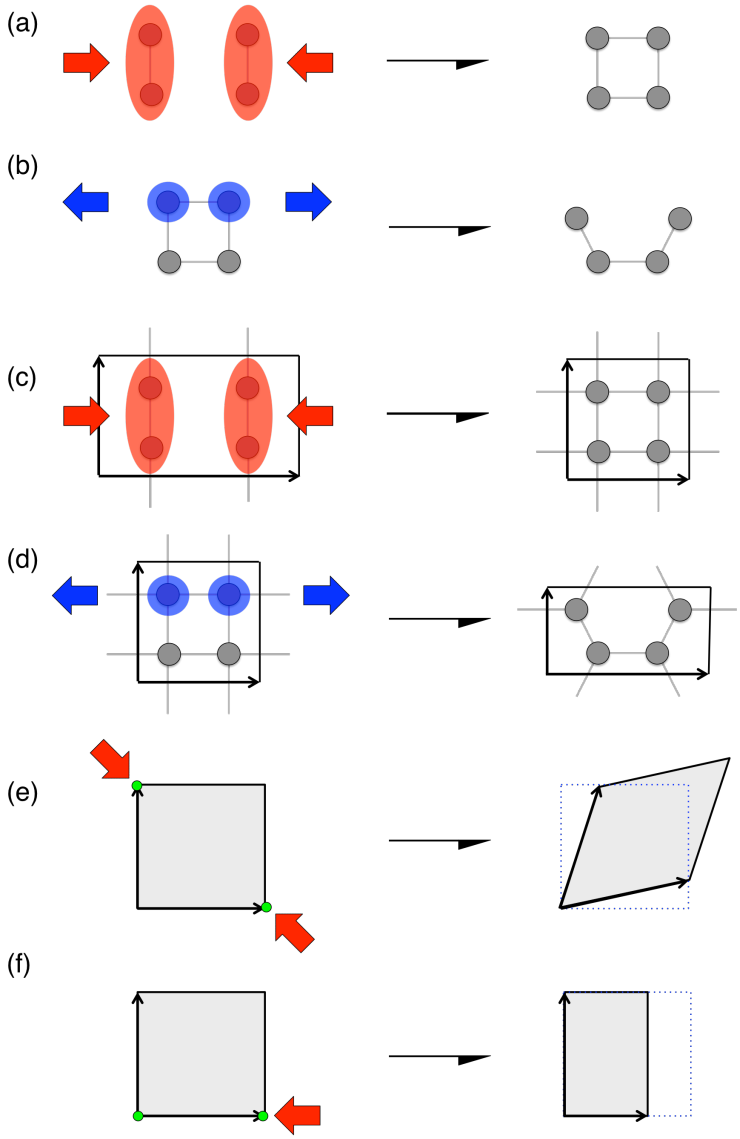

Figure. 2-2. Schematic of the SC-AFIR method: (a) a positive force applied to a molecular system, (b) a negative force applied to a molecular system, (c) a positive force applied to atoms in a periodic system, (d) a negative force applied to atoms in a periodic system, (e) a positive force applied to a pair of TVs, and (f) a positive force applied to the origin and one of the TVs. A green circle indicates a dummy atom.

2-2-4. Structural clustering

A crystal structure can be expressed by a number of different ways regarding the shape of the unit-cell and atomic arrangements in the unit-cell. For example, there were a number of ways to describe the crystal structure of graphite. With the C_8/unit-cell, graphite can be written with a nearly cubic unit-cell, a largely elongated cuboid unit-cell, a highly distorted rhombohedral unit-cell, and many others. These graphite structures have similar but slightly different energies owing to numerical errors in the first principles calculations. Without any care, the SC-AFIR search, which was targeted to low-energy structures, tended to be applied only to graphite (or lowest-lying structures in a given system). This is because the probability that the lowest-lying structures are selected is typically large in the stochastic algorithm,[16] and in most cases, the SC-AFIR is applied to one of the lowest-lying structures expressed with different unit-cells.

To overcome this problem, structural clustering was performed during the automated search. A similarity between two structures was checked by comparing them with a super-cell, and those judged to be similar were regarded to belong to the same group. From each group, the following structures were selected as representatives.

i. The most stable structure.
ii. The structure which has the largest χ, where χ is a quantity defined as the length of shortest TV divided by the longest TV.
iii. The structure which has the smallest φ, where φ is the sum of absolute values of inner products between all pairs of normalized TVs.
iv. The structure which has the smallest λ, where $\lambda = (1 - \chi + \varphi) / 2$.

The other structures were then excluded from the search. Structures that had a highly distorted unit-cell, in which an angle between a pair of TVs was smaller than $\pi/4$ or larger than $3\pi/4$, were also excluded from the search .

Some structures that can be described only with highly elongated or largely distorted unit-cells may be missed, because the above conditions avoid searches starting from structures having such unit-cells. Actually, one previously reported structure, which is written with a highly elongated unit-cell, was missed in the present automated search, as discussed in Section 2-3-4. This is a serious problem when only a small unit-cell is applicable. However, even those with an elongated and/or distorted unit-cell in a given cell-size can be obtained with nearly cubic unit-cells with a larger cell-size.

Any periodic structure can be described by a nearly cubic unit-cell, when a sufficiently large unit-cell is applied.

2-2-5. Flow of the SC-AFIR search

The search generates a set of MINs. The list of MINs obtained by the search is termed as the MIN-list. The search proceeds as follows.

1. Start from initial structure(s).
2. Choose a pair of fragments in one of the MINs in the MIN-list by the procedure described in Section 2-2-1 combined with the structural clustering introduced in Section 2-2-4.
3. Minimize the AFIR function for the chosen fragment pair to obtain the AFIR path, which is the approximate reaction path.
4. Optimize the MINs starting from local minima along the AFIR path, and add newly obtained MINs to the MIN-list.
5. Exit from the automated search if the latest P AFIR paths did not update the set of lowest M MINs.
6. Return to the step 2, and continue the search.

The initial structure can either be one or more of the optimized MIN(s), or one or more random structure(s). In the case where the optimized MINs are given, these MINs are added to the MIN-list directly. Otherwise, randomly generated initial structures are optimized, and then these optimized MINs are added to the MIN-list.

In step 4, the MINs are optimized on the PES. Therefore, MINs in the MIN-list are all local minima on the PES. Minimization of both the PES in step 4 and the AFIR function in step 3 are done by the rational function optimization (RFO) method[18], where the RFO step is determined for the $3N + 3$, $3N$, or $3N - 3$ internal degrees of freedom in three-, two-, or one-dimensional periodic systems, respectively, as discussed in Section 2-2-2. In addition, steps 2 to 6 can be done in parallel.

After completion of the SC-AFIR calculation, not only the most stable structure but also a huge database of low-lying structures is generated. Furthermore, their network via the AFIR path is also obtained without any additional calculation. First-order saddle points can be located by optimizing the AFIR path by any path-optimization method. It is also possible to obtain the reaction path network via the

steepest descent path (SDP) starting from the first-order saddle points, by the additional SDP calculations. Systematic study on the path network in the crystal system generated by the SC-AFIR method will be the future subject.

2-2-6. Electronic structure calculation

SIESTA3.2[19-21] was used to compute the energy, force acting on atoms, and stress tensor acting on a unit-cell. These calculations were performed using density functional theory (DFT) with the PBE functional and the DZP basis set. Grimme's dispersion correction[22], with the parameters R_0 = 2.904 Å and $C6$ = 4.0 kJ·Å^6·mol^{-1}, was added, where the value of $C6$ was adjusted so that the present computation reproduced the inter-layer distance of graphite of 3.4 Å. The pseudopotential of carbon was prepared using the parameters in the GGA Pseudopotential Database[23], where the core correction was not considered. A Monkhorst–Pack grid was, respectively, set to 4×4×4, 4×4×1, or 4×1×1, including the Γ point in the searches for three-, two-, or one-dimensional periodic structures for the *k*-point sampling. Collinear spin alignment was taken into account. The electronic temperature was set to 5.0 K. The mesh cutoff value was set to 50.0 Ry in the automated search, and finally increased to 200.0 Ry; all structures discussed below are optimized MINs on the PES with the higher mesh cut off value.

2-2-7. Computational procedures

The concrete procedure in this study of searching for low-lying crystal structures of the carbon systems proceeds along the following five steps.

(a) Generate an initial structure in the C_4/unit-cell by optimizing a random structure.

(b) Search for MINs with the C_4/unit-cell by the SC-AFIR starting from the single initial structure generated in step (a).

(c) Generate initial structures in the C_8/unit-cell by extending the unit-cell in MINs obtained for the C_4/unit-cell in step (b) along the shortest TV of each MIN, and then re-optimizing them in the C_8/unit-cell.

(d) Search for MINs with the C_8/unit-cell by the SC-AFIR starting from the initial structures obtained in step (c).

(e) Re-optimize all structures generated in step (d) in the C_8/unit-cell with the

higher mesh cutoff value (200.0 Ry).

Finally, further analyses were conducted for the important crystal structures obtained. Spglib-1.8.3 was used to determine the space group of the obtained crystal structures[24]. Phonopy-1.10.8 was used to calculate the phonon dispersion.[25,26] Prior to the band and phonon calculations, the corresponding structure was reoptimized with a Monkhorst–Pack grid of 12×12×12. Gnubans in SIESTA3.2 was used to calculate the band dispersion. The k paths were determined according to the method previously described in the literature.[27]

2-3. RESULTS

2-3-1. Three-dimensional crystal structures of carbon with the C_8/unit-cell

The search was initiated from a single MIN obtained by optimizing a randomly generated structure in the C_4/unit-cell. In total, 274 MINs were obtained after the five steps (a)–(e) described in Section 2-2-7. **Table 2-1** shows degrees of freedom in each system, the numbers of AFIR paths and MINs obtained after each step and the number of gradient calculations required to finish each step.

Table 2-1. Degrees of freedom f, the number of obtained AFIR paths N_{path}, obtained MIN structures N_{MIN} and gradient calculations required in each step $N_{gradient}$, in the search of three-dimensional structures of carbon.[a]

Step [b]	f	N_{path}	N_{MIN}	$N_{gradient}$
(a)	15	–	1	34
(b)	15	158	35	46,838
(c)	27	–	24	2,010
(d)	27	697	377	323,321
(e)	27	–	274	19,653

[a] a single gradient calculation includes calculations of the energy, force, and stress tensor.

[b] the steps (a)–(e) are described in Section 2-2-7.

The 30 most stable MINs among the 274 MINs are shown in **Fig. 2-3**, where the *N*th lowest MIN is labeled as 3D-min*N*. The names of those known previously, either experimentally or theoretically, are also shown in the structural labels. The space group indicated in the structural labels were determined by spglib-1.8.3. The energy values are relative to the most stable structure, hexagonal graphite (**3D-min0**). Both of the known graphite structures, hexagonal (alpha) and rhombohedral (beta), were obtained as **3D-min0** and **3D-min2**, respectively. The former, with *AB*-stacking, showed a lower energy than the latter having *ABC* stacking, consistent with the previously acquired knowledge. Hexagonal graphite (**3D-min0**) showed a lower energy than cubic diamond (**3D-min1**), and this was also consistent with the known trend. The structure with *AA*-stacking was not a local minimum with the present setup for electronic structure calculation, where the geometry optimization starting from such an initial structure collapsed into hexagonal graphite. Note that cubic diamond was energetically more stable than hexagonal graphite when the original PBE-D2 parameters were used together with the present setup for electronic structure calculation. This would arise from the parameters such as the DZP basis set, or the parameters such as the pseudopotential, charge density cutoff, and *k*-mesh and so forth that were adopted in this study. In this study, by adjusting the *C*6 value of the PBE-D2 parameters, the energetics in **Fig. 2-3**, which was consistent with the previously acquired knowledge, was obtained. We also notice that the energy difference between hexagonal graphite and cubic diamond in **Fig. 2-3** is still smaller than that in the more elaborate calculation (~3 kJ/mol·atoms).[28]

Many previously reported structures, such as hexagonal graphite (**3D-min0**), cubic diamond (**3D-min1**), rhombohedral graphite (**3D-min2**), lonsdaleite (or hexagonal diamond) (**3D-min3**), Cco-C_8 or *Z*-carbon (**3D-min4**),[4,5] crossed graphene (**3D-min5**),[29] *M*-carbon (**3D-min6**),[2,3] 8-tetra(2,2) tubulane or bct C_4 (**3D-min7**),[30-39] LA5 or Y carbon (**3D-min8**),[38,40] *C*2/*m*-16 (**3D-min9**),[41] 3D-(5,0) (**3D-min14**),[39] *oI*16-carbon (**3D-min20**),[42] *mC*16-carbon (**3D-min22**),[42] 3D-(4,4) carbon or squaroglitter (**3D-min23**),[39,43] isoglitter (**3D-min29**),[44] 8-tetra(3,3) tubulane or E (**3D-min33**),[30,36,38,45] LA7 (**3D-min52**),[38] diam_cr43_bo (**3D-min57**),[46] LA10 (**3D-min69**),[47] a hypothetical metallic allotrope of carbon or bct-4 carbon (**3D-min82**) [2,48-51], and F (**3D-min196**),[36] were found in the automated search. The correspondence between the previously reported structures and those obtained by the present search was

determined by comparing our structures with those with 2, 4, 8, and 16 atoms per unit-cell in the SACADA,[6] except for the case of **3D-min5** and **3D-min11**. **3D-min11** is a structure in which net2b,[52] a two-dimensional sheet composed of five- and seven-membered rings, is stacked.

In **Fig. 2-3**, 8-tetra(3,3) tubulane (**3D-min33**), LA7(**3D-min52**), diam_cr43_bo (**3D-min57**), LA10 (**3D-min69**), hypothetical metallic allotrope of carbon (**3D-min82**), and F (**3D-min196**), are not shown because these structures have higher energies of 35.2, 39.7, 41.1, 46.1, 50.1, and 80.2 kJ/mol·atoms, respectively. To the best of our knowledge, the other structures have not previously been reported. This demonstrates that the present approach is useful for exploring unknown crystal structures.

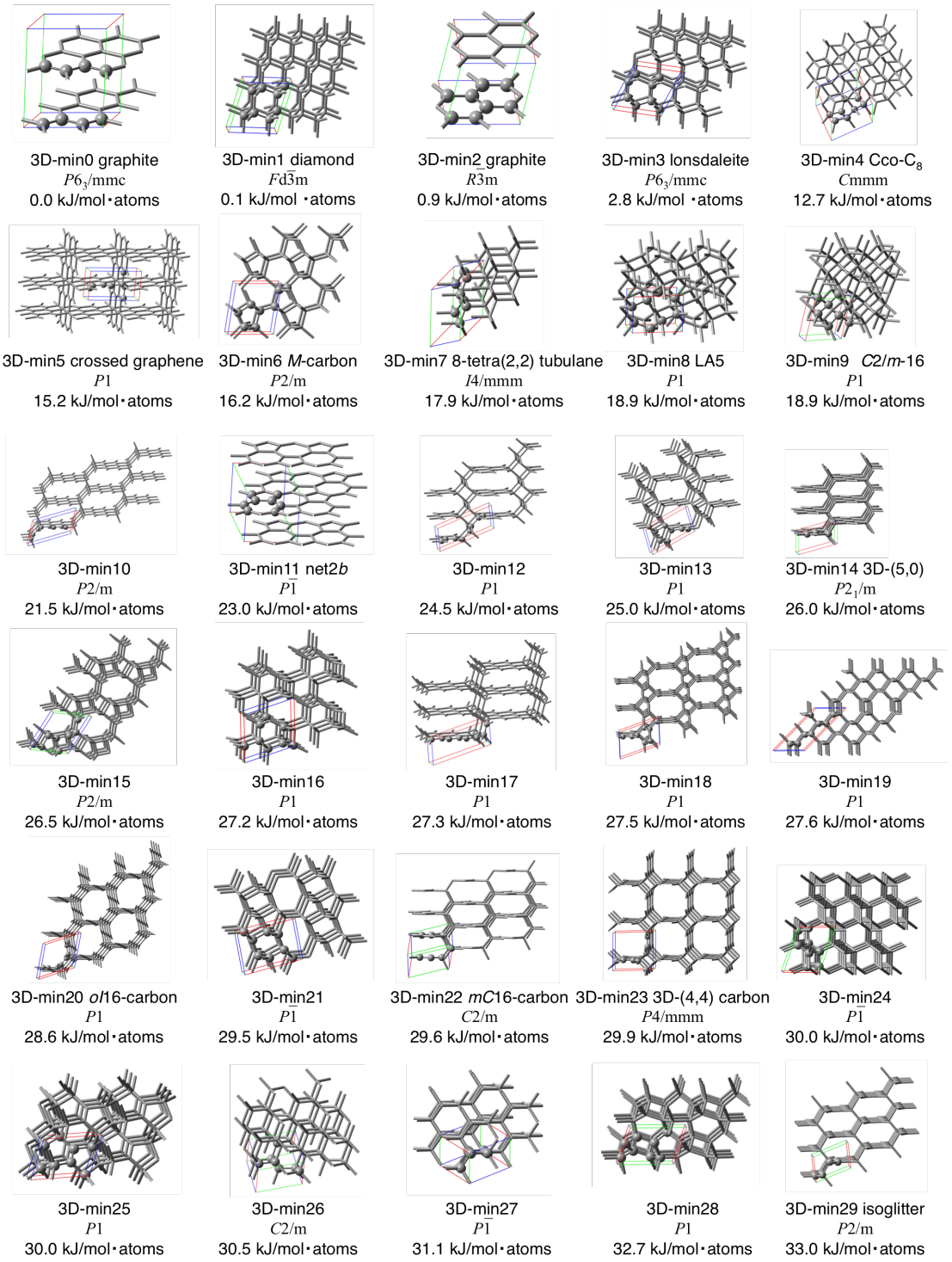

Figure. 2-3. Thirty of the most stable crystal structures of carbon with the C_8/unit-cell. The names of structures (if available), space groups, and relative energies are shown in the labels. TVs are shown as red, green, and blue lines. Atoms in a unit-cell are highlighted by the ball model.

2-3-2. Two-dimensional periodic structures of carbon with the C_8/unit-cell

The search for the two-dimensional structures was also initiated from a single MIN obtained by optimizing a randomly generated structure in the C_4/unit-cell. In total, 122 MINs were obtained after the five steps (a)–(e) described in Section 2-2-7. **Table 2-2** shows degrees of freedom in each system, the numbers of AFIR paths and MINs obtained after each step and the numbers of gradient calculations required to finish each step.

Table 2-2. Degrees of freedom f, the number of obtained AFIR paths N_{path}, obtained MIN structures N_{MIN} and gradient calculations required in each step $N_{gradient}$, in the search of two-dimensional structures of carbon. [a]

Step [b]	f	N_{path}	N_{MIN}	$N_{gradient}$
(a)	12	–	1	42
(b)	12	87	28	16,623
(c)	24	–	24	1,524
(d)	24	572	237	153,965
(e)	24	–	122	14,082

[a] a single gradient calculation includes calculations of the energy, force, and stress tensor.

[b] the steps (a)–(e) are described in Section 2-2-7.

The low-lying 15 structures are shown in **Fig. 2-4**. The Nth lowest structure is labeled as 2D-min$N$. The names of those known previously, either experimentally or theoretically, are shown in the structural labels. The energy values are relative to the most stable structure, hexagonal graphite (**3D-min0**).

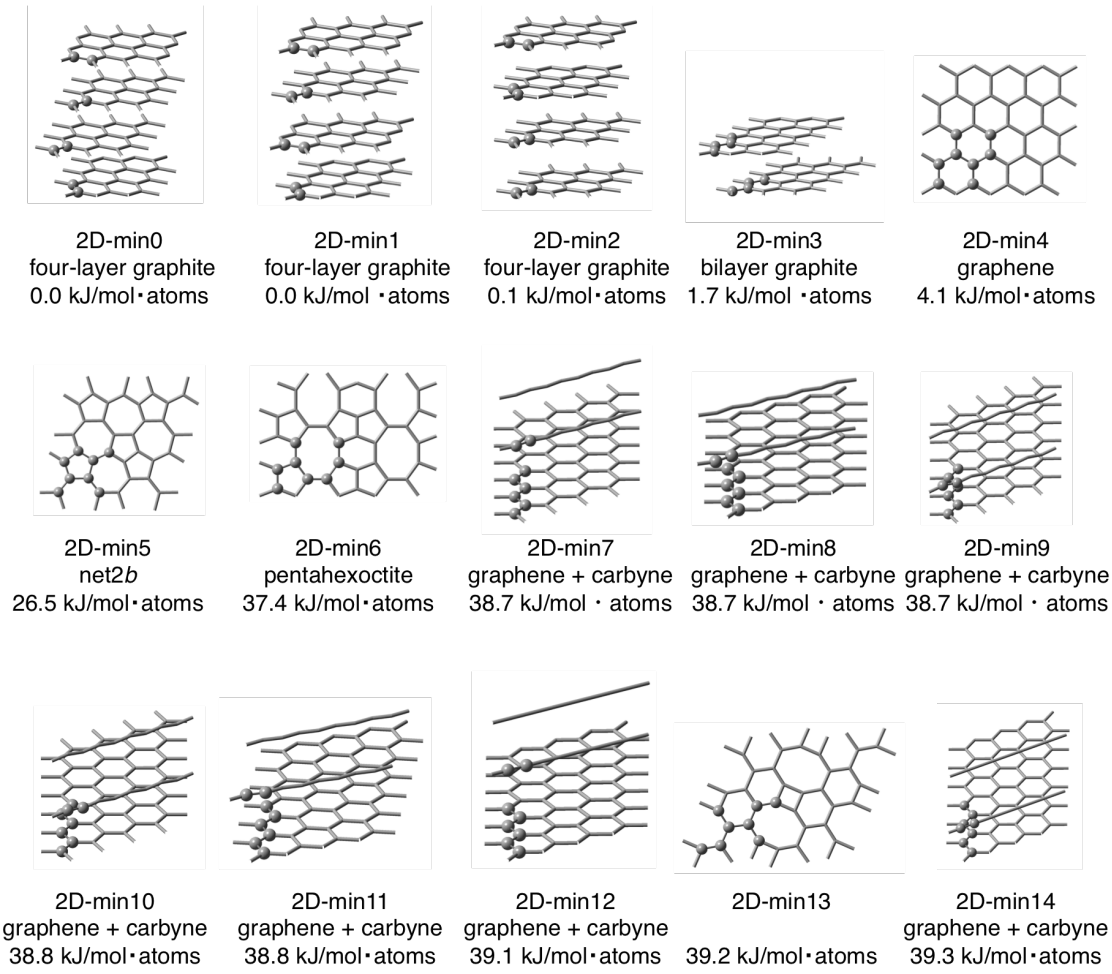

Figure 2-4. Fifteen low-lying two-dimensional periodic structures of carbon with the C_8/unit-cell. The names of the structures (if available) and relative energies are shown in the labels. Atoms in a unit-cell are highlighted by the ball model.

The lowest-lying structure is the four-layer graphite (**2D-min0-2**). A graphene sheet can be written with a unit-cell including two carbon atoms. With eight carbon atoms, not only graphene but also four-layer and bilayer graphite can be obtained. The stacking type of **2D-min0** is *ABCA*. In 2D-min1, the bottom three layers adopt an *ABC* stacking. The top layer is similar to, but slightly deviated from *B*. In **2D-min2**, the bottom three layers show an *ABB* stacking, although the top layer is deviated from all the other three. The slight deviation from the *ABC*-layers seen in **2D-min1** and **2D-min2** arises from the present setup of the electronic structure calculation, which is not very accurate for describing weak interactions. Bilayer graphite (**2D-min3**) with an *AB*-stacking and graphene (**2D-min4**) are the next most stable structures. In addition, a

lot of sheet structures that contain three-, four-, five-, six-, seven-, eight-, nine-, and/or ten-membered rings were obtained, where some of them correspond to those predicted from graph theory, such as net2*b* (**2D-min5**)[52-55], pentahexoctite (**2D-min6**),[56] and network7 (**2D-min23**).[53,57-61] Carbynes are stabilized by interacting with a graphene (**2D-min7-12**, **2D-min14-18**). Although they all are clusters between graphene and carbyne, they are different to each other in their interaction sites. In addition, two-dimensional sheets with a certain thickness, such as layered-diamond[62] (**2D-min19**) and related structures (**2D-min20-22**), were also found.

2-3-3. One-dimensional periodic structures of carbon with the C_8/unit-cell

The search for one-dimensional structures was initiated from a single MIN obtained by optimizing a randomly generated structure in the C_4/unit-cell. In total, 49 MINs were obtained after the five steps (a)–(e) described in Section 2-2-7. **Table 2-3** shows degrees of freedom in each system, the numbers of AFIR paths and MINs obtained after each step and the numbers of gradient calculations required to finish each step.

Table 2-3. Degrees of freedom *f*, the number of obtained AFIR paths N_{path}, obtained MIN structures N_{MIN} and gradient calculations required in each step $N_{gradient}$, in the search of one-dimensional structures of carbon. [a]

Step [b]	*f*	N_{path}	N_{MIN}	$N_{gradient}$
(a)	9	–	1	16
(b)	9	114	63	13,499
(c)	21	–	42	2,992
(d)	21	447	201	66,230
(e)	21	–	49	10,901

[a] a single gradient calculation includes calculations of the energy, force, and stress tensor.

[b] the steps (a)–(e) are described in Section 2-2-7.

The low-lying 15 structures are shown in **Fig. 2-5**. The *N*th lowest structure is labeled as 1D-min*N*. The names of the structures known previously, either experimentally or theoretically, are shown in the structural labels. The energy values are relative to the most stable structure, hexagonal graphite (**3D-min0**).

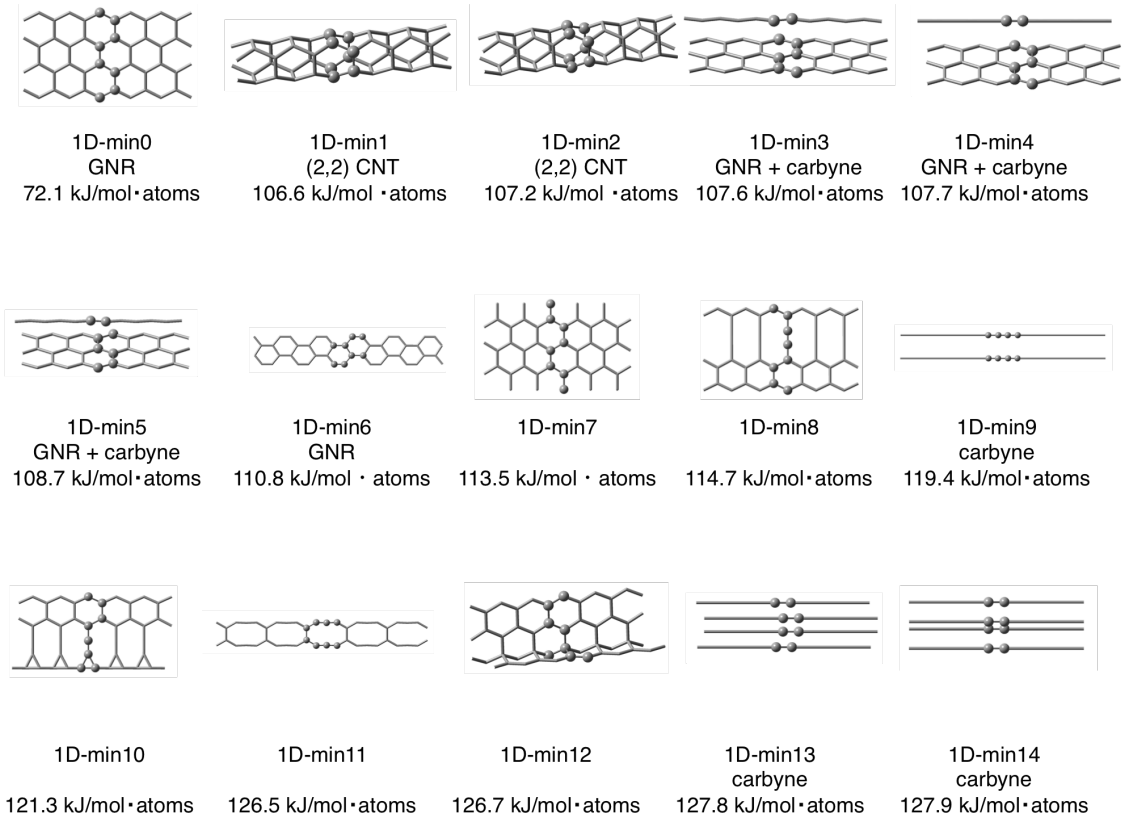

Figure 2-5. Fifteen low-lying one-dimensional periodic structures of carbon with the C_8/unit-cell. Names of structures (if available) and relative energies are shown in labels. Atoms in a unit-cell are highlighted by the ball model.

The most stable structure is GNR (**1D-min0**). Another stable structure is the (2,2)-CNT (**1D-min1**, **1D-min2**), which is the smallest CNT. **1D-min2** is elongated along the *x*-axis compared with **1D-min1**. **1D-min3-5** are clusters of GNR and carbyne that resemble each other. These three are different in their interaction sites. Carbyne (**1D-min9**, **1D-min13**, **1D-min14**) is less stable than the GNR-carbyne clusters (**1D-min3-5**). The polyacene-like thinnest GNR (**1D-min25**) was found as the 26th most stable structure. Some structures containing three-, four-, five-, six-, seven-, eight-, nine-, and/or ten-membered rings were also found as higher-energy structures.

2-4. DISCUSSION

Among the newly found crystal structures, **3D-min10** is the most stable. Its structure is shown in various ways in **Fig. 2-6**. Its primitive lattice contains eight carbon atoms, and its space group is *P*2/m. This structure is composed of sp^2 and sp^3 carbons and corresponds to a structure in which graphene sheets in graphite are connected to each other by C-C bonds. We note that a similar structure has previously been reported as diam_cr43_bo (**3D-min57**).[46] The difference is whether or not the structures contain four-membered rings, where **3D-min10** does not have a four-membered ring and thus is more stable than **3D-min57**. The phonon dispersion shows that **3D-min10** is a local minimum structure. The band structure in **Fig. 2-7** suggests that this structure is metallic. Furthermore, a Dirac cone was found between the A and X points in the band structure of **3D-min10**.

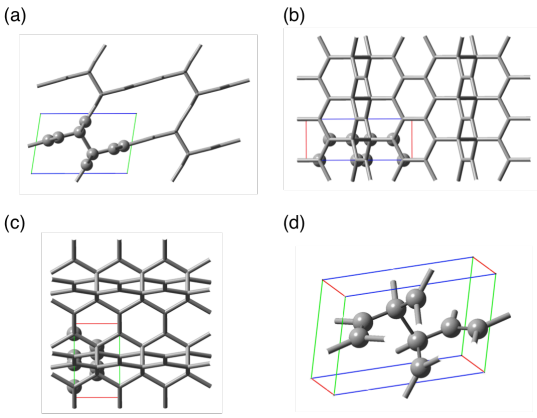

Figure 2-6. Views along the *a*-axis (a), *b*-axis (b), and *c*-axis (c), and the primitive-cell (d) of **3D-min10**. TVs are shown as red, green, blue lines.

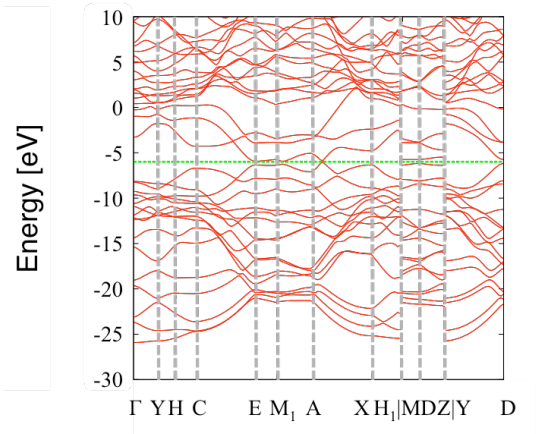

Figure 2-7. Band structure of **3D-min10**. The Fermi level is shown by a green line. The definition of k point is described in ref. 27.

The second most stable structure among those newly found in this study, i.e., **3D-min12**, is depicted in **Fig. 2-8**. The space group of this structure is *P*1. It includes eight carbon atoms in its primitive lattice. This structure is composed of sp^2 and sp^3 carbons and is similar to 3D-(4,4) carbon (**3D-min23**).[39,42] Both of these structure have a large hollow, and the size and shape of the hollow are different for **3D-min12** and **3D-min23**. Phonon dispersion indicates that **3D-min12** is a local minimum structure. The band structure in **Fig. 2-9** shows that this structure is metallic.

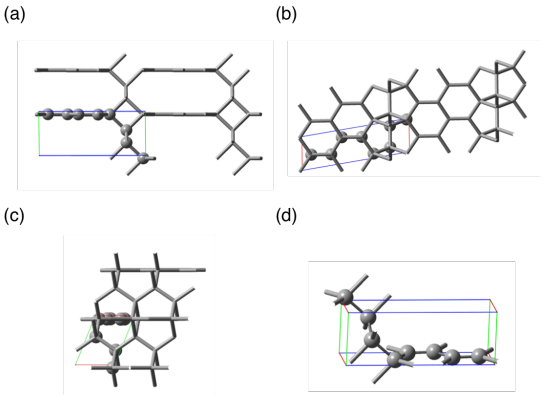

Figure 2-8. Views along the *a*-axis (a), *b*-axis (b), and *c*-axis (c), and the primitive-cell (d) of **3D-min12**. TVs are shown as red, green, blue lines.

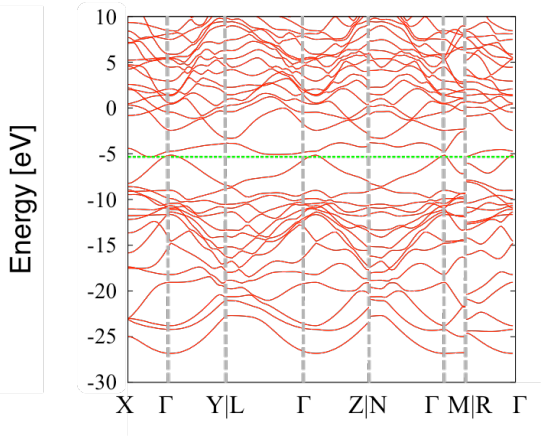

Figure 2-9. Band structure of **3D-min12**. The Fermi level is shown by a green line. The definition of k point is described in ref. 27.

The third most stable structure among those newly found in this study is **3D-min13**. Its structure is depicted in **Fig. 2-10** in various ways. The space group of this structure is *P*1. It includes eight carbon atoms in its primitive lattice. This structure is composed of sp^2 and sp^3 carbons and is similar to C_{CAS}.[63] Although both of these structure have five-membered rings and a large hollow, they are different to each other in their size of the hollow. Phonon dispersion indicates that **3D-min13** is a local minimum structure. The band structure in **Fig. 2-11** shows that this structure also is metallic. Furthermore, two Dirac cones were found around the Y point and the L point in the band structure of **3D-min13**.

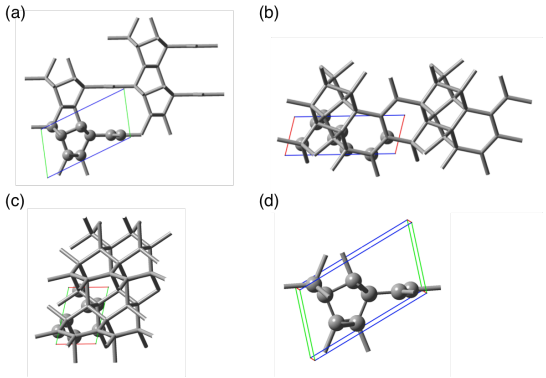

Figure 2-10. Views along the *a*-axis (a), *b*-axis (b), and *c*-axis (c), and the primitive-cell (d) of **3D-min13**. TVs are shown as red, green, blue lines.

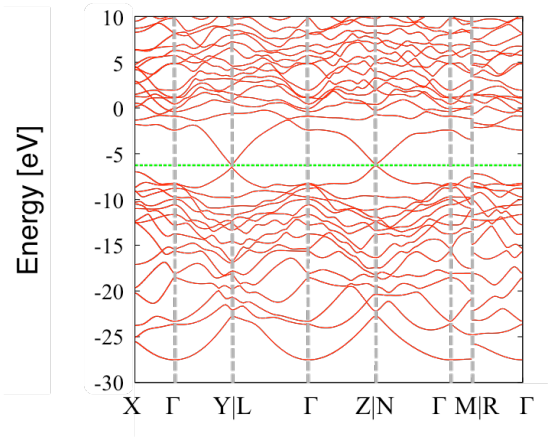

Figure 2-11. Band structure of **3D-min13**. The Fermi level is shown by a green line. The definition of k point is described in ref. 27.

Carbyne, shown in **Fig. 2-12 (a)**, was obtained as the 266th lowest MIN (**3D-min265**) with a high relative energy of 112.3 kJ/mol·atoms. Carbyne is a linear, pure-carbon chain described as a resonance structure of polyyne $(–C{\equiv}C–)_n$ and polycumulene $(=C=)_n$. Although short carbon chain molecules have been studied extensively,[64-67] the production of very long chains composed of more than 6000 atoms has been achieved only recently in a double-walled CNT.[68] The present search found a structure, shown in **Fig. 2-12 (b)**, in which carbyne is sandwiched by graphene sheets (3D-min36). Intriguingly, the relative energy of the sandwiched structure of 37.5 kJ/mol·atoms is lower than the average energy of graphite and carbyne, which is 56.2 kJ/mol·atoms. This suggests that carbyne is also stabilized by graphene sheets.

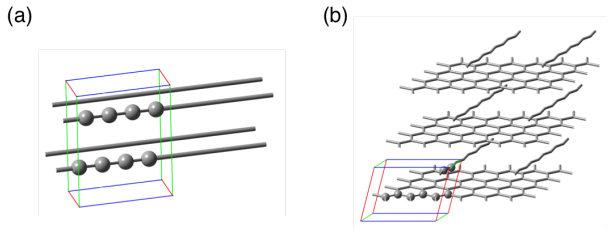

Figure 2-12. The structures of (a) carbyne and (b) sandwiched carbyne. TVs are shown in red, green, blue lines.

The present search missed a previously reported structure called 4H-diamond[69] even though it can be written with the C_8/unit-cell. In 4H-diamond, structures of diamond and hexagonal diamond co-exist, and its unit-cell is highly elongated. The 4H-diamond was missed because of the structural clustering, which was introduced in Section 2-2-4. The algorithm restricts the search to areas in which the shape of the unit-cell is not far from cubic. As discussed in Section 2-2-4, this structure is expected to be found with the present algorithm if a larger unit-cell is used. The other structures which were missed were K_4[70-72] and D_{6h} prism-C_{12}.[73] This is because these structures have a much higher energy than **3D-min0**. Hence, the present search, which is targeted to low-energy strictures,[16] was unable to find them. These structures can be found when a larger *P* and *M* values are adopted, where *P* and *M* are the parameters of the stochastic search algorithm as defined in Section 2-2-1. We note that a K_4-like structure was predicted in the present search as **3D-min223**, where its energy 88.9 kJ/mol·atoms is slightly higher than K_4 83.3 kJ/mol·atoms at the present computational level.

2-5. CONCLUSION

In this study, the AFIR method was combined with the PBCs. The AFIR method has been used extensively in the exploration of reaction pathways in molecular systems. The combined PBC/AFIR approach was applied to the carbon crystals described by the C_8/unit-cell. The search automatically generated the previously reported low-lying structures. Furthermore, a lot of unreported structures were found. This suggests that the AFIR method is effective not only in molecular systems but also for the global exploration of low-lying crystal structures of a given atomic composition.

Among the many newly found structures, three low-lying structures were further studied. These three structures have a slightly higher energy than those predicted previously, such as Cco-C_8 (Z-carbon) and M-carbon. All the three structures did not exhibit a band-gap and were predicted to behave as a metal. Furthermore, Dirac cones were discovered in the band structures of two of these structures.

In addition, the present approach was extended for the exploration of two- or one-dimensional periodic structures. A search of two-dimensional periodic structures with C_8/unit-cell gave many structures, such as two-dimensional sheets, composed of three-, four-, five-, six-, seven-, eight-, nine-, and/or ten-membered rings including graphene. Another search of the one-dimensional periodic structures with a C_8/unit-cell

found GNR, the thinnest CNT, carbyne, and so forth.

The present results suggest that this PBC/AFIR approach is promising in exploring low-lying periodic structures systematically. Furthermore, this approach, in principle, is applicable to any periodic systems. Applications to systems including two or more elements and/or to molecular crystals will be interesting future avenues for research.

2-6. APPENDIX

A2-1. Forces on TVs

In general, fractional coordinates are used in the field of solid physics. SIESTA and VASP programs outputs forces on unit-cell (or forces on the TVs) as stress tensor. On the other hands, Gaussian and Turbomole uses Cartesian coordinate. GRRM program are also used Cartesian coordinate, because it's main target was molecular systems. Therefore we need the forces on the TVs in Cartesian coordinate even in the case SIESTA and VASP programs are used.

The basis conversion of Fractional coordinate to Cartesian coordinate is described bellow,

$$\mathbf{x}_{\mathrm{c}} = \mathbf{h}^{t}\mathbf{x}_{\mathrm{f}}, \tag{A1}$$

Here, $\mathbf{x}_{\mathrm{c}}$ is Cartesian coordinate, $\mathbf{h}$ is unit-cell, $\mathrm{x_f}$ is fractional coordinate, respectively. Therefore, the basis conversion of Cartesian coordinate to fractional coordinate is

$$\mathbf{x}_{\mathrm{f}} = \left(\mathbf{h}^{t}\right)^{-1}\mathbf{x}_{c}, \tag{A2}$$

To perform the search in the abovementioned coordinate system, the first-derivative of the total energy for TVs, i.e., $\partial E/\partial h$, is required. In this study, $\partial E/\partial h$ was obtained with the following equation

$$\left.\frac{\partial E}{\partial \mathbf{h}}\right|_{\mathbf{h}_0} = -V_0\sigma^{t}\mathbf{h}_0^{-1}, \tag{A3}$$

where E is the potential energy, $\mathbf{h}_0$ is the unit cell with which the stress is calculated, V_0 is the volume of the unit-cell, and $\boldsymbol{\sigma}$ is the stress tensor.

A2-2. Coupling of the forces on atoms

By using **Eq. A3**, stress is converted to fractional coordinate to Cartesian coordinate. Note that this convert is just the basis conversion, i.e., converted forces on TVs (stress) still contained coupling of the forces on atoms. Let's consider the case where TVs slightly changes (**TV'** = **TV** + **h**) as shown in **Fig. A2-1**. In the case of Cartesian coordinate, when the TVs slightly change, atoms in the cell are not changed. On the other hands, in the case of fractional coordinate, when the TVs slightly change, atoms in the cell are also moved. Therefore when converting the stress from fractional coordinate to Cartesian coordinate, coupling of the forces on atoms should be removed from converted forces on TVs (**Fig. A2-2**).

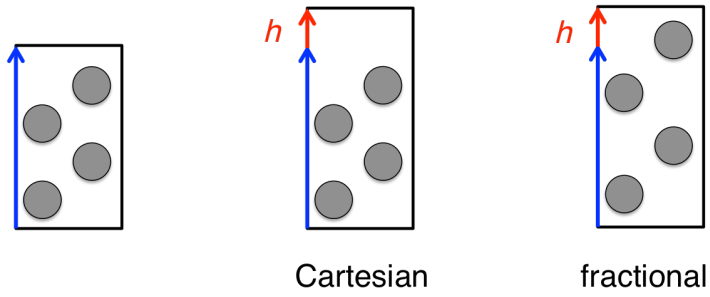

Figure A2-1. The difference between the Cartesian coordinate and fractional coordinate when TVs slightly changes.

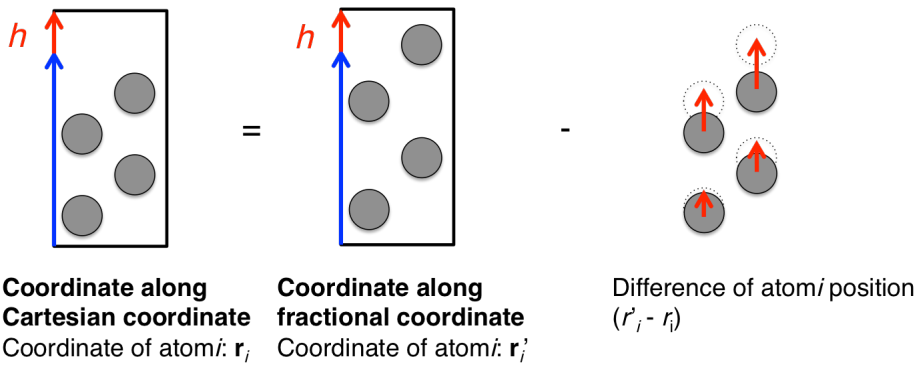

Figure A2-2. Schematic of coupling of the forces on atoms removed from converted stress.

In this study, the true forces on TVs in the Cartesian coordinate are obtained by the difference method differentiated the energy that estimated by the first order Taylor expansion. Here, energy deference caused by **h** ($\mathrm{d}E_{\mathbf{h}}$) was obtained with the following equation

$$\mathrm{d}E_h = \mathbf{G}^{TV}\mathbf{h} - \sum_{i}^{allAtoms} \mathbf{G}_i(\mathbf{r}'_i - \mathbf{r}_i) \qquad \text{(A4)}$$

,

where, $\mathbf{G}^{TV}$ is converted stress (forces on TVs, but its direction along fractional coordinate)) and $\mathbf{G}_i$ is forces on *i*th atoms, $\mathbf{r}'_i$ is *i*th atom positions along fractional coordinate, $\mathbf{r}_i$ is *i*th atom positions in Cartesian coordinate.

2-7. REERENCE

[1] V. Georgakilas, J. A. Perman, J. Tucek, and R. Zboril, Chem. Rev. **115**, 4744 (2015).

[2] A. R. Oganov and C. W. Glass, J. Chem. Phys. **124**, 244704 (2006).

[3] Q. Li, Y. Ma, A. R. Oganov, H. Wang, H. Wang, Y. Xu, T. Cui, H.-K. Mao, and G. Zou, Phys. Rev. Lett. **102**, 175506 (2009).

[4] Z. Zhao, B. Xu, X.-F. Zhou, L.-M. Wang, B. Wen, J. He, Z. Liu, H.-T. Wang, and Y. Tian, Phys. Rev. Lett. **107**, 215502 (2011).

[5] M. Amsler *et al.*, Phys. Rev. Lett. **108**, 065501 (2012).

[6] SACADA, http://sacada.sctms.ru.

[7] R. Hoffmann, A. A. Kabanov, A. A. Golov, and D. M. Proserpio, Angew. Chem. Int. Ed. **55**, 10962 (2016).

[8] Supplemental Material of PRB(Takagi).

[9] D. J. Wales and H. A. Scheraga, Science **285**, 1368 (1999).

[10] K. Sanderson, Nature **450**, 771 (2007).

[11] A. R. Oganov, *Modern Methods of Crystal Structure Prediction* (John Wiley & Sons, Hoboken, NJ, , 2011).

[12] C. J. Pickard and R. J. Needs, Journal of Physics-Condensed Matter **23**, 053201 (2011).

[13] T. Gu, W. Luo, and H. Xiang, Wiley Interdisciplinary Reviews-Computational Molecular Science **7**, UNSP e1295 (2017).

[14] S. Maeda, K. Ohno, and K. Morokuma, Phys. Chem. Chem. Phys. **15**, 3683 (2013).

[15] S. Maeda, T. Taketsugu, and K. Morokuma, J. Comput. Chem. **35**, 166 (2014).

[16] S. Maeda, Y. Harabuchi, M. Takagi, T. Taketsugu, and K. Morokuma, Chemical Record **16**, 2232 (2016).

[17] W. M. C. Sameera, S. Maeda, and K. Morokuma, Acc. Chem. Res. **49**, 763 (2016).

[18] A. Banerjee, N. Adams, J. Simons, and R. Shepard, J. Phys. Chem. **89**, 52 (1985).

[19] D. SanchezPortal, P. Ordejon, E. Artacho, and J. M. Soler, Int. J. Quantum Chem **65**, 453 (1997).

[20] J. M. Soler, E. Artacho, J. D. Gale, A. Garcia, J. Junquera, P. Ordejon, and D. Sanchez-Portal, Journal of Physics-Condensed Matter **14**, 2745, Pii s0953-8984(02)30737-9 (2002).

[21] D. Sanchez-Portal, P. Ordejon, and E. Canadell, in *Principles and Applications of Density in Inorganic Chemistry Ii*, edited by N. Kaltsoyannis, and J. E. McGrady2004), pp. 103.

[22] S. Grimme, J. Comput. Chem. **27**, 1787 (2006).

[23] GGA Pseudopotential Database, http://departments.icmab.es/leem/siesta/Databases/Pseudopotentials/periodictable-gga-abinit.html (Accessed accessed May 3, 2016).

[24] computer code spglib, https://atztogo.github.io/spglib/ (Accessed accessed January 12, 2016).

[25] computer code phonopy, https://atztogo.github.io/phonopy/ (Accessed accessed June 16, 2016).

[26] A. Togo, F. Oba, and I. Tanaka, Phys. Rev. B **78**, 134106 (2008).

[27] W. Setyawan and S. Curtarolo, Computational Materials Science **49**, 299 (2010).

[28] T. Bucko, J. Hafner, S. Lebegue, and J. G. Angyan, J. Phys. Chem. A **114**, 11814 (2010).

[29] S. Bahmann, T. Weissbach, and J. Kortus, Physica Status Solidi-Rapid Research Letters **7**, 639 (2013).

[30] R. H. Baughman and D. S. Galvao, Chem. Phys. Lett. **211**, 110 (1993).

[31] P. A. Schultz, K. Leung, and E. B. Stechel, Phys. Rev. B **59**, 733 (1999).

[32] K. Umemoto, R. M. Wentzcovitch, S. Saito, and T. Miyake, Phys. Rev. Lett. **104**, 125504 (2010).

[33] H. S. Domingos, Journal of Physics-Condensed Matter **16**, 9083, Pii s0953-8984(04)81075-0 (2004).

[34] R. H. Baughman, A. Y. Liu, C. Cui, and P. J. Schields, Synth. Met. **86**, 2371 (1997).

[35] J. V. Badding and T. J. Scheidemantel, Solid State Commun. **122**, 473, Pii s0038-1098(02)00136-9 (2002).

[36] R. T. Strong, C. J. Pickard, V. Milman, G. Thimm, and B. Winkler, Phys. Rev. B **70**, 045101 (2004).

[37] X.-F. Zhou, G.-R. Qian, X. Dong, L. Zhang, Y. Tian, and H.-T. Wang, Phys. Rev. B **82**, 134126 (2010).

[38] V. A. Greshnyakov and E. A. Belenkov, Journal of Experimental and Theoretical Physics **113**, 86 (2011).

[39] Z. Zhao, B. Xu, L.-M. Wang, X.-F. Zhou, J. He, Z. Liu, H.-T. Wang, and Y. Tian, Acs Nano **5**, 7226 (2011).

[40] Q. Zhu, Q. Zeng, and A. R. Oganov, Phys. Rev. B **85**, 201407 (2012).

[41] X. Zhang, Y. Wang, J. Lv, C. Zhu, Q. Li, M. Zhang, Q. Li, and Y. Ma, J. Chem. Phys. **138**, 114101 (2013).

[42] M. Hu, J. He, Q. Wang, Q. Huang, D. Yu, Y. Tian, and B. Xu, Journal of Superhard Materials **36**, 257 (2014).

[43] D. L. V. K. Prasad, N. M. Gerovac, M. J. Bucknum, and R. Hoffmann, J. Chem. Theory Comput. **9**, 3855 (2013).

[44] M. J. Bucknum, E. A. Castro, and B. Wen, J. Math. Chem. **50**, 2281 (2012).

[45] C. Cheng, Z.-L. Lv, Y. Cheng, X.-R. Chen, and L.-C. Cai, Diamond Relat. Mater. **43**, 49 (2014).

[46] J. Fayos, J. Solid State Chem. **148**, 278 (1999).

[47] E. A. Belenkov and V. A. Greshnyakov, Journal of Experimental and Theoretical Physics **119**, 101 (2014).

[48] R. Hoffmann, T. Hughbanks, M. Kertesz, and P. H. Bird, JACS **105**, 4831 (1983).

[49] G. M. Rignanese and J. C. Charlier, Phys. Rev. B **78**, 125415 (2008).

[50] R. H. Baughman and D. S. Galvao, Nature **365**, 735 (1993).

[51] M. J. Xing, B. H. Li, Z. T. Yu, and Q. Chen, Commun. Theor. Phys. **64**, 237 (2015).

[52] A. F. Wells, Acta Crystallogr. **7**, 535 (1954).

[53] A. T. Balaban, C. C. Rentia, and E. Ciupitu, Rev. Roum. Chim. **13**, 231 (1968).

[54] V. H. Crespi, L. X. Benedict, M. L. Cohen, and S. G. Louie, Phys. Rev. B **53**, 13303 (1996).

[55] M. Deza, P. W. Fowler, M. Shtogrin, and K. Vietze, J. Chem. Inf. Comput. Sci. **40**, 1325 (2000).

[56] B. R. Sharma, A. Manjanath, and A. K. Singh, Sci. Rep. **4**, 7164 (2014).

[57] H. Y. Zhu, A. T. Balaban, D. J. Klein, and T. P. Zivkovic, J. Chem. Phys. **101**, 5281 (1994).

[58] M. J. Bucknum and E. A. Castro, Solid State Sciences **10**, 1245 (2008).

[59] X.-Q. Wang, H.-D. Li, and J.-T. Wang, Phys. Chem. Chem. Phys. **14**, 11107 (2012).

[60] X.-L. Sheng, H.-J. Cui, F. Ye, Q.-B. Yan, Q.-R. Zheng, and G. Su, J. Appl. Phys. **112**, 074315 (2012).

[61] Z. Zhu and D. Tomanek, Phys. Rev. Lett. **109**, 135501 (2012).

[62] F. J. Ribeiro, P. Tangney, S. G. Louie, and M. L. Cohen, Phys. Rev. B **72**, 214109 (2005).

[63] Z.-J. Wei, H.-Y. Zhao, J. Wang, and Y. Liu, J. Appl. Phys. **120**, 165101 (2016).

[64] R. I. Kaiser, Chem. Rev. **102**, 1309 (2002).

[65] F. Cataldo, *Polyynes: Synthesis, Properties, and Applications* (CRC Press/Taylor & Francis, Boca Raton, FL, 2005).

[66] C. S. Casari, M. Tommasini, R. R. Tykwinski, and A. Milani, Nanoscale **8**, 4414 (2016).

[67] Y. Taguchi, H. Endo, T. Kodama, Y. Achiba, H. Shiromaru, T. Wakabayashi, B. Wales, and J. H. Sanderson, Carbon **115**, 169 (2017).

[68] L. Shi *et al.*, Nature Materials **15**, 634 (2016).

[69] K. E. Spear, A. W. Phelps, and W. B. White, J. Mater. Res. **5**, 2277 (1990).

[70] B. Winkler, C. J. Pickard, V. Milman, and G. Thimm, Chem. Phys. Lett. **337**, 36 (2001).

[71] T. Sunada, The American Mathematical Society **55**, 208 (2008).

[72] M. Itoh, M. Kotani, H. Naito, T. Sunada, Y. Kawazoe, and T. Adschiri, Phys. Rev. Lett. **102**, 055703 (2009).

[73] K. Ohno, H. Satoh, and T. Iwamoto, Chem. Phys. Lett. **633**, 120 (2015).

Chapter 3.

Building a Crystal Structure Data List including Properties by using PBC/AFIR Method: A Case Study on Carbon

Abstract: In this chapter, a data list of small carbon crystal (C_1-C_{16}/unit-cell) is built by using PBC/AFIR method and some interesting structures are picked up from the data list. At first, exhaustive search for carbon crystal (C_1-C_{16}/unit-cell) by PBC/AFIR method were performed. As results, 14265 structural data of carbon crystal structures were generated. Then properties (sp^3/sp^2 ratio, density, band gap) were also calculated. The obtained structural data list includes the previously reported structures. Moreover, even in carbon crystals that are well examined, many new structures were obtained. By using this data list, some interesting structures were found with four search conditions based on properties.

3-1. INTRODUCTION

Properties of materials depend not only on their composition but also on their crystal structure. Carbon can take various forms, such as diamond, graphite, lonsdaleite (hexagonal diamond), fullerene, carbon nanotube (CNT), graphene, graphene nanoribbon (GNR), and so on. Furthermore, many stable structures have been predicted theoretically. *M*-carbon,[1,2] Cco-C_8 (or *Z*-carbon)[3,4] and so forth have been predicted recently from first principles. Up to now, more than five hundred structures have already been registered to the Samara carbon allotrope database (SACADA).[5,6] In material development, a data list of crystal structures and their properties, if available, would be very useful.[7,8] Structures are always required before computing their properties, and hence, crystal structure prediction would be the first step to build such a data list. In this context, the crystal structure prediction from first principles has become one of the active fields in materials science. To date, various methods have been developed. [9-12] Recently, we developed PBC/AFIR method[13] by combined artificial force induced reaction (AFIR) method with periodic boundary conditions (PBCs). This method enables global search for low-lying crystal structures.

In this study, to build a data list of small carbon crystal (C_1-C_{16}/unit-cell) including properties, at first exhaustive searches were performed by using PBC/AFIR method, then additional calculations for the properties (sp^3/sp^2 ratio, density, band gap) of obtained structures were performed. Some interesting structures were found by searching the data list with four search conditions based on properties.

3-2. METHOD

3-2-1. Overlap structures

A crystal structure can be expressed even if it is not a primitive-cell. For example, graphite can be described at least C_2/unit-cell. Therefore, graphite can also be described by even number carbon atoms in the unit cell (C_{2n}/unit-cell). We call such structures as "overlap structures". In this study, the smallest one is left in the data list and the other overlap structures were removed from the data list. Note that the random stacking structures such as AB-staking graphite or ABC-staking graphite were judged as independent structures and both of them were left in the data list.

3-2-2. Artifact structures

In general, a minimum on a Potential Energy Surface (PES) with PBCs may not be a minimum on a PES of its super-cell ($MIN_{super\text{-}cell}$). We call such an unstable structure as the artifact structure. Our results also include artifact structures because the PBC/AFIR method is method for searching minima on given PES. In this study, artifact structures were removed from the data list by the following procedure; at first, structure optimization calculation with 2×2×2 super-cell is performed for all obtained structures by the steepest descent method up to 20 steps. Then, those with large structural change, root mean square (RMS) of a structural change is larger than 0.05 Å or maximum distance change is larger than 0.07 Å, were regarded as the artifact structures.

3-2-3. sp^3/sp^2 ratio

In this study, sp^3/sp^2 ratio is determined by equation (1),

$$sp^3 / sp^2 \text{ratio} = \frac{N_{sp^3}}{N_{sp^2} + N_{sp^3}}, \qquad (1),$$

where, $N_{sp}{}^2$ and $N_{sp}{}^3$ are the numbers of the sp^2 carbon and the sp^3 carbon in the unit-cell, respectively. The sp^2 carbon and the sp^3 carbon were distinguished by using the number of bonds of atoms; if the C-C distance less than 1.85 Å, it is regarded as bonded.

3-2-4. Setting of PBC/AFIR method

The calculation setting of crystal structure search by PBC/AFIR method is the same as our previous study[13]; the model collision energy parameter γ was set to 1000.0 kJ/mol. To perform priority search for lower energy structure, the model temperature parameter T_R[14] was set to 10000.0 K and the search was terminated if the last P AFIR paths did not update the set of lowest M MINs. Here, M and P were set to f and $3f$, respectively, where f is the number of internal degrees of freedom. The crystal structure searches were performed with the developer version on the GRRM program.[15]

3-2-5. Electronic structure calculation

Self-consistent charge density functional tight-binding (SCC-DFTB) calculation[16] were performed by using DFTB3/pbc-0-3 parameter[17] and empirical dispersion (D3).[18] The k-point sampling for Monkhorst–Pack is set to 4×4×4 for crystal structure searches, 30×30×30 for the band gap calculations. Electric state calculation and band gap calculation were performed with the dftb+ program.[19,20]

3-2-6. Computational procedures

The concrete procedure in this study of searching for low-lying crystal structures of the carbon systems proceeds along the following five steps.

(a) Generate an initial structure in the each system (C_1 - C_{16}/unit-cell) by optimizing a random structure.

(b) Search for MINs of each system by the SC-AFIR starting from the single initial structure generated in step (a).

(c) The structure optimization calculations with 2×2×2 super-cell are performed for all structures obtained in step (b) by the steepest decent method up to 20 steps.

(d) Remove the overlap structures and artifact structures from the data list.

(e) Calculate the properties (sp^3/sp^2 ratio, density, band gap) for the all crystal structures in data list.

Finally, some interesting structures were found by searching this data list with four search conditions based on properties.

3-3. RESULTS

3-3-1. The numbers of obtained structures

In total, 14265 unique structures were obtained by the procedure described in Section 3-2-6. A much more structure was obtained than registered in SACADA. The numbers of overlap structures, artifact structures and features of the artifact structures of carbon crystal are discussed in **APPENDIX**. Famous previously reported structures, such as diamond, lonsdaleite (hexagonal diamond), graphite, Cco-C_8, *M*-carbon, etc., are included in the data list.

3-3-2. The energy distribution of the obtained structures

In this data list, the energy of obtained structures distributed from 0.00 eV/atoms to 3.07 eV/atoms. The energy is relative values to the most stable structure, diamond. In the range of 2.00 eV/atoms or more, a few structures of C_1/unit-cell and C_3/unit-cell are distributed. The histograms of the energy distribution of obtained structures, up to 2.00 eV, are shown in **Fig. 3-1**. The energy distribution of C_{2i+1} is shown in **Fig. 3-1 (a)**, and the one of C_{2i} is shown in **Fig. 3-1 (b)**. The color of the histogram correspond to the composition. According to **Fig. 3-1**, relatively lower energy structures were searched efficiently. In both case of C_{2i-1} and C_{2i}, as system become larger, the distribution of lower energy structures also increases. This means, lower energy structures that could not be described in a small system were efficiently searched on a large system. In the case of **Fig. 3-1 (b)**, the most stable structures, diamond (0.00 eV/atoms) and graphite (0.10 eV/atoms) and their polytype structures[21] are exist in the lower energy regions. On the other hands, in the case of **Fig. 3-1 (a)**, the structure does not exist below 0.30 eV/atoms because the most stable structures, diamond and graphite, could not described by C_{2i+1}.

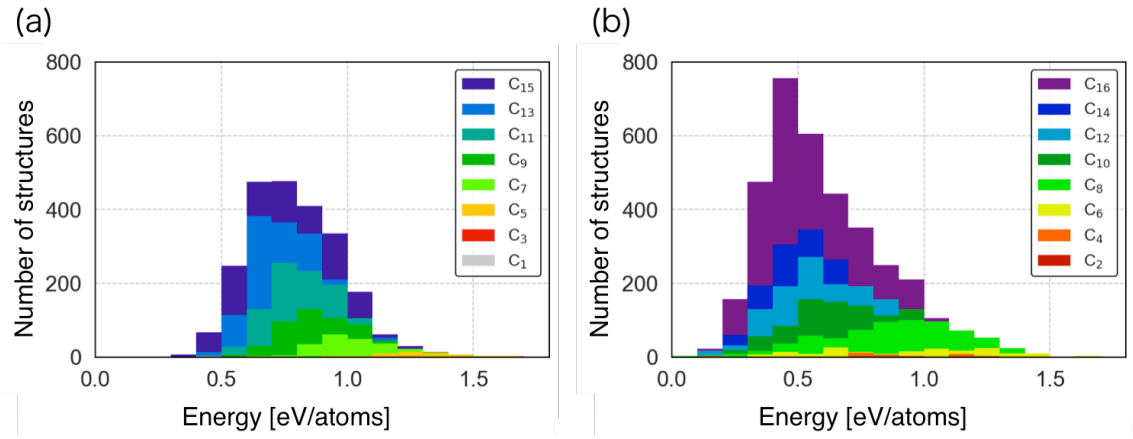

Figure 3-1. The histograms of energy destribution of the obtain structures. (a) C_{2i+1}/unit-cell (b) C_{2i}/unit-cell. The color correspond to the composition.

3-3-3. The density distribution

In this data list, the density distributed from 1.26 g/cm^3 to 3.62 g/cm^3. The density distribution of obtained structures with respect to sp^3/sp^2 ratio is shown in **Fig. 3-2**. The density distribution was plotted with Gaussian function, equation (2).

$$Z_i \exp\left(-\left(\frac{(x-R_i)^2}{2\sigma_x^2}+\frac{(y-D_i)^2}{2\sigma_y^2}\right)\right), \tag{2}$$

$$Z_i = \frac{e\exp\left(\frac{-E_i}{k_B T}\right)}{\sum_j^{allMINs}\exp\left(\frac{-E_j}{k_B T}\right)}, \tag{3}$$

where, Z_i is the assumed Boltzmann distribution of MINi described in equation (3). R_i, D_i, E_i is sp^3/sp^2 ratio, density and relative energy of MINi, respectively. σ_x and σ_y was set to 0.01 and 0.04. k_B is the Boltzmann constant, and T was set to 1000.0 [K]. In **Fig. 3-2**, the color corresponds to the population. The graphite region (0.0 %, 2.56 g/cm^3) and diamond region (100.0 %, 3.56 g/cm^3) have the largest distribution. Most of the other distributions are distributed on the line connecting the graphite region and the diamond region.

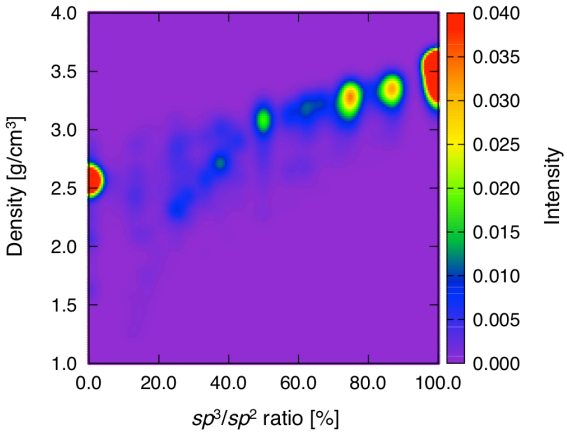

Figure 3-2. The density distribution of obtained structures with respect to sp^3/sp^2 ratio. The color corresponds to the population. Note that these values are calculated from C_1-C_{16}/unit-cell, so the sp^3/sp^2 ratio takes a discrete value.

3-3-4. The band gap distribution

In this data list, the band gap distributed from 0.00 eV to 9.07 eV. The band gap distribution of obtained structures with respect to sp^3/sp^2 ratio is shown in **Fig. 3-3**. The band gap distribution is plotted with Gaussian function, equation (4).

$$Z_i \exp\left(-\left(\frac{\left(x-R_i\right)^2}{2\sigma_x^2}+\frac{\left(y-Eg_i\right)^2}{2\sigma_y^2}\right)\right), \tag{4}$$

where Z_i is weight function assumed Boltzmann distribution, shown in equation (3). R_i and E_{gi} is sp^3/sp^2 ratio and band gap of MINi, respectively. σ_x and σ_y was set to 0.091 and 0.009. T was set to 1000.0 [K]. In **Fig. 3-3**, the color corresponds to the population. The graphite region (0.0 %, 0.00 eV) and the diamond region (100.0 %, 7.00 eV) have the largest distribution.

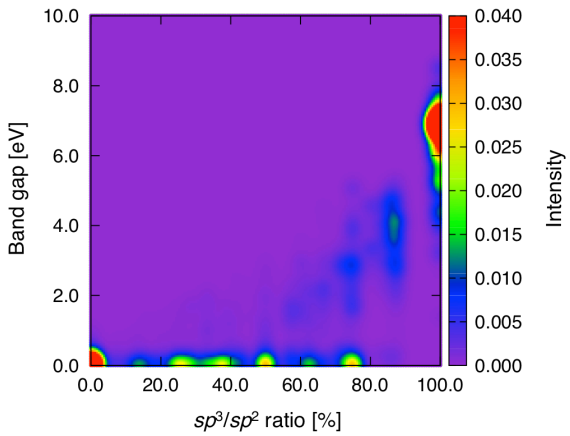

Figure 3-3. The band gap distribution of obtained structures with respect to sp^3/sp^2 ratio. The color corresponds to the population. Note that these values are calculated from C_1-C_{16}/unit-cell, so the sp^3/sp^2 ratio takes a discrete value.

3-4. DISCUSSION

We searched the structure from data list by following four conditions.

3-4-1. Structures based on density

As shown in **Fig. 3-2**, the density distributed from 1.26 g/cm^3 to 3.62 g/cm^3, but most of the population is distributed in the range from graphite to diamond (2.56 - 3.56 g/cm^3). Here, the most stable structures in each density regions in range (2.50 - 3.60 g/cm^3) were searched from the data list. Obtained structures are depicted in **Fig. 3-4** and the properties of these structures are shown in **Table 3-1,** where the *N*th -lowest MIN of C_n is labeled as C_nMIN*N*. In this range, graphite is the most stable structure in the lowest density region. In the density middle range, the structures that sp^3 carbon inserted in graphite are obtained (**C_{16}MIN87** and **C_{14}MIN18**). In the higher density region, the structures that have higher sp^3 ratio such as **C_{12}MIN17** and diamond are obtained.

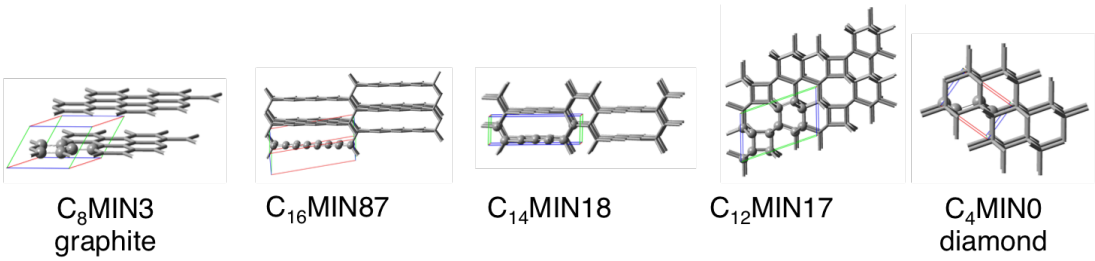

Figure 3-4. The most stable structures in each density region (2.50 – 3.60 g/cm^3). TVs are shown as red, green, and blue lines. Atoms in a unit cell are highlighted by the ball model.

Table 3-1. The properties of the most stable structures in each density regions (2.5 - 3.6 g/cm^3).

	energy [eV/atoms]	sp^3/sp^2 ratio [%]	density [g/cm^3]	band gap [eV]
C_8MIN3	0.10	0.0	2.57	0.00
C_{16}MIN87	0.25	25.0	2.92	0.25
C_{14}MIN18	0.22	57.1	3.17	0.57
C_{12}MIN17	0.11	100.0	3.50	1.00
C_4MIN0	0.00	100.0	3.56	1.00

Next, the structures that have lower density than graphite (< 2.50 g/cm^3) were picked up from the data list and depicted in **Fig. 3-5** and the properties of these structures are shown in **Table 3-2**. The structural framework of **C_{16}MIN61**, **C_{14}MIN29**, **C_{12}MIN34**, **C_{10}MIN18** and **C_8MIN18** are called crossed graphene[22] (or Z-type interpenetrating graphene networks (IGNs)[23]) which graphite (or GNR) are cross-linked by diamond-like junction. Therefore, these structures have lower sp^3/sp^2 ratio and lower densities. According to Ref. 23, the framework is denoted as Z(i,j), where i and j are the number of zigzag chains in the GNR parts. It is reported that such frameworks may exists in glassy carbon.[24] In our data list, all crossed graphene that can be described up to C_{16}/unit-cell were included; Z(1,1), Z(1,2), Z(1,3), Z(2,2), Z(1,4), Z(2,3), Z(1,5), Z(2,4), Z(3,3), Z(1,6), Z(2,5), Z(3,4)). We found that when the system is small, graphene sheet in these structures is a flat, but when it gets larger, there are wavy conformer such as Z(1,6) (**C_{16}MIN61**). The flexibility of such a structure might be the origin of elasticity of the glassy carbon. In addition, the new structures that have combinations of the crossed graphene frameworks were found. For example, **C_{16}MIN103** and **C_{14}MIN39** in **Fig. 3-5** are combined structures of Z(1,1) and Z(1,3), Z(1,1) and Z(1,2), respectively. **C_{16}MIN113** is combined structures of Z(1,4) and the crossed graphene-like structure that have the connected junctions without GNR, it might be called Z(0,1).

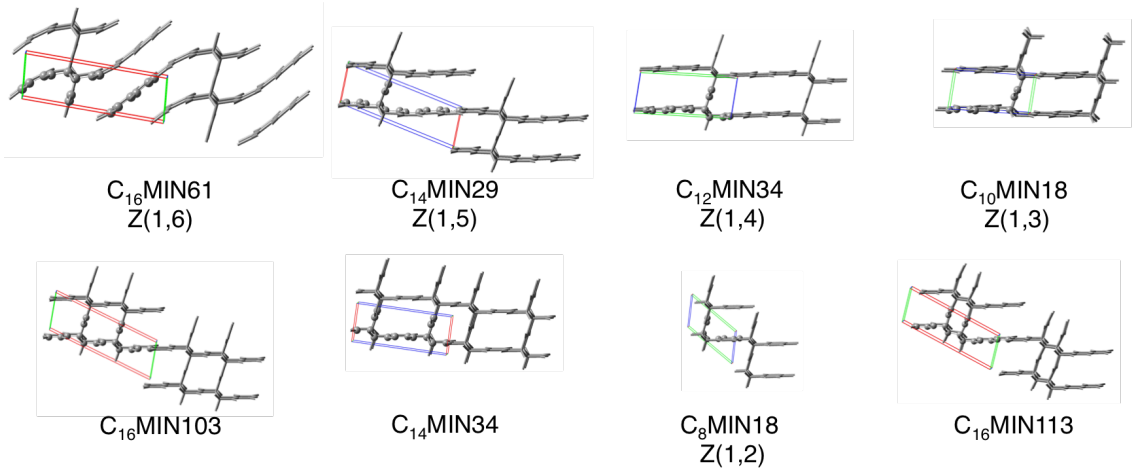

Figure 3-5. The lower energy structure that have lower density than graphite (< 2.50 g/cm^3). TVs are shown as red, green, and blue lines. Atoms in a unit cell are highlighted by the ball model.

Table 3-2. The properties of the lowest energy structures that have lower density than graphite (< 2.50 g/cm^3).

	energy [eV/atoms]	sp^3/sp^2 ratio [%]	density [g/cm^3]	band gap [eV]
C_{16}MIN61	0.23	12.5	2.43	0.00
C_{14}MIN29	0.24	14.3	2.08	0.01
C_{12}MIN34	0.25	16.7	2.12	0.01
C_{10}MIN18	0.25	20.0	2.20	0.07
C_{16}MIN103	0.25	25.0	2.33	0.00
C_{14}MIN39	0.26	28.6	2.44	0.02
C_8MIN18	0.26	25.0	2.33	0.01
C_{16}MIN113	0.26	25.0	2.34	0.00

Moreover, new frameworks similar to the crossed graphene were found in lower density region. The minimal structure of this framework is **C_{12}MIN48** (**Fig. 3-6**). The difference between the crossed graphene and **C_{12}MIN48** is the direction of the junction. The direction of the junctions in the crossed graphene are same, while the junctions are faced each other in the **C_{12}MIN48**. Note that the structures that have alternated junctions were reported as bct-C_{12}.[25] As shown here, various varieties of porous structures might be designed by not only the elongation of the GNR part but also the changing the orientation of the junction or combination of these frameworks.

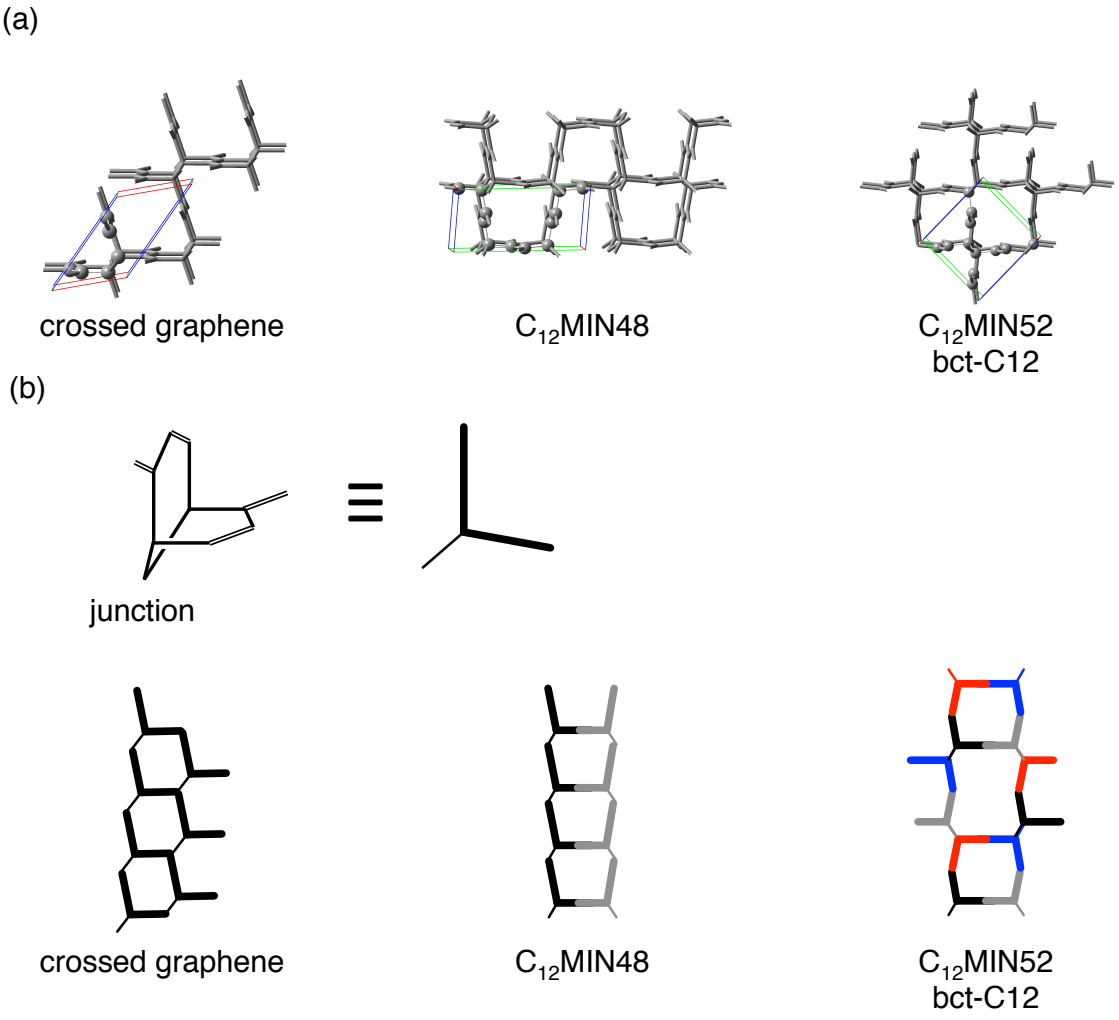

Figure 3-6. (a) Structure of crossed graphene and similar structures. TVs are shown as red, green, and blue lines. Atoms in a unit cell are highlighted by the ball model.
(b) Schematic of crossed graphene and similar structures. The color corresponding to the direction of the junction.

3-4-2. Structures based on band gap

As shown in **Fig. 3-3**, in a smaller band gap structures the distribution of graphite region is large, and in a larger band gap structures the one of diamond region is large. Here, semiconductor materials (1.00 eV < band gap <1.50 eV) were searched from the data list. The lower energy structures that satisfied the conditions were shown in **Fig. 3-7** and the properties of these structures are shown in **Table 3-2**. The most stable one is **C_{12}MIN42** (3D-(7,0)[26]) that includes small width armchair GNR. The second stable one is **C_{16}MIN182** that contains four-, five-, six-membered rings. The third stable one is **C_{16}MIN199** that has the structure in which the sheets that only contains five-membered rings and seven-membered rings are inserted in diamond. **C_{12}MIN78** include zigzag GNR and four- and eight-membered rings. This structure is a combined structure of 3D-min12[13] and bct-C_4.[26-35]

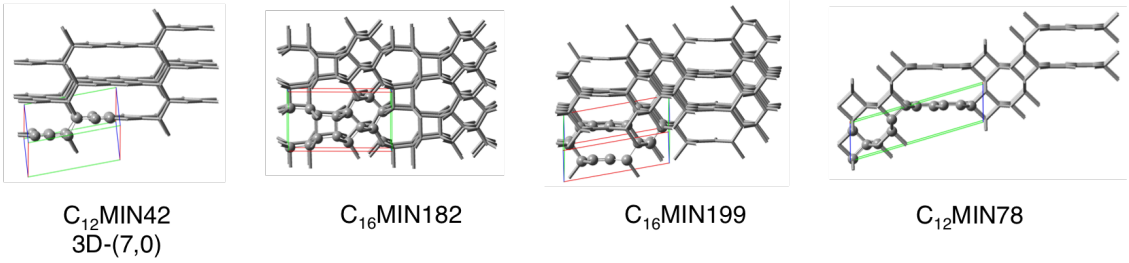

Figure 3-7. The lower energy semiconductor structures (1.00 eV < band gap < 1.50 eV). TVs are shown as red, green, and blue lines. Atoms in a unit cell are highlighted by the ball model.

Table 3-3. The properties of lower energy semiconductor materials.

	energy [eV/atoms]	sp^3/sp^2 ratio [%]	density [g/cm^3]	band gap [eV]
C_{12}MIN42	0.26	33.3	2.57	1.01
C_{16}MIN182	0.29	100.0	2.92	1.40
C_{16}MIN199	0.29	62.5	3.17	1.21
C_{12}MIN78	0.31	66.7	3.50	1.33

3-4-3. Compound conditions

As shown above, most of the population distributed in diamond region (high density, large band gap) and graphite region (lower density, small band gap). Here, we picked up the structures from the region that opposite to these trends, i.e., higher density metallic region and lower density insulator region.

3-4-3-1. Higher density metallic structures

The higher density (semi) metallic structures (density > 3.00 g/cm^3, band gap < 0.01 eV) were searched from data list and the lower energy structures satisfied the conditions were depicted in **Fig. 3-8** and the properties of these structures are shown in **Table 3-4**. All of the structures in **Fig. 3-8** have the structure in which armchair GNRs are inserted in diamond. These structures are similar to hybrid diamond-graphite structures.[36] These structures distribute in wide density range because there are varieties of the size of the diamond domain and the size of graphite domain variations.

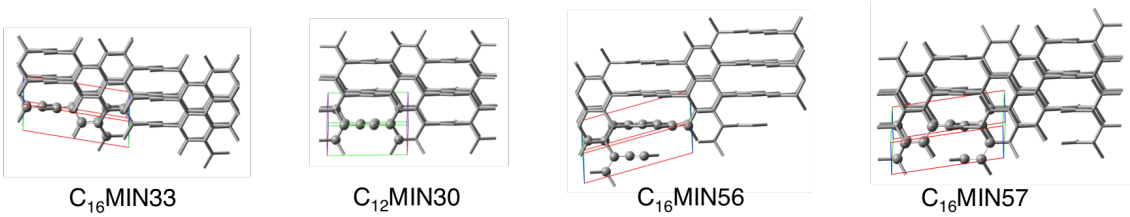

Figure 3-8. The lower energy structures of the higher density (> 3.00 g/cm^3) metallic structures. TVs are shown as red, green, and blue lines. Atoms in a unit cell are highlighted by the ball model.

Table 3-4. The properties of the higher density (semi) metallic structures.

	energy [eV/atoms]	sp^3/sp^2 ratio [%]	density [g/cm^3]	band gap [eV]
C_{16}MIN33	0.16	75.0	3.34	0.00
C_{12}MIN30	0.21	66.7	3.27	0.00
C_{16}MIN56	0.22	50.0	3.12	0.00
C_{16}MIN57	0.23	75.0	3.30	0.00

3-4-3-2. Lower density insulator structures

The lower density insulator structures (density < 3.00 g/cm^3, band gap > 5.00 eV) were searched from data list and the lower energy structures were depicted in **Fig. 3-9** and the properties of these structures are shown in **Table 3-5**. The most stable structure is **C_{14}MIN515** that has voids build from four-, five-, and six- membered rings. The second stable one is **C_6MIN32** (16-truncated octahedral[37] or other names[30,35,38,39]) in which spheres consisting of four- and six-membered rings are adjacent. As a similar structure, CFS that has spheres consisting of only five-membered rings has reported[40]. The third stable one is **C_8MIN171** that includes three-, five-, and six-membered rings and large voids. **C_8MIN193** (called 3D (4,0)-I[30,41] or TA6[35]) has boat form six-membered rings (or planer eight-membered rings) combined by four membered rings in a bellows shape. The structure of this region have higher sp^3/sp^2 ratio but they have voids, therefore their densities relatively lower. They also contain three- or four- membered rings, and the structure is not very stable. Note that there is a possibility that to describe the variety of lower density structures, the degrees of freedom may not be enough in the range up to C_{16}/unit-cell.

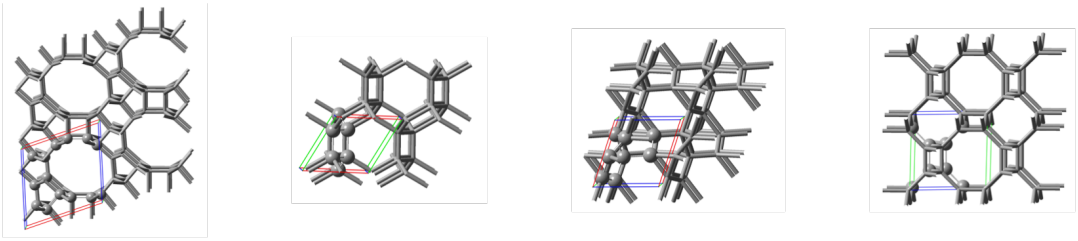

Figure 3-9. The lower energy structures of the lower density (< 3.00 g/cm^3) insulator. TVs are shown as red, green, and blue lines. Atoms in a unit cell are highlighted by the ball model.

Table 3-5. The properties of the lower density insulator structures.

	energy [eV/atoms]	sp^3/sp^2 ratio [%]	density [g/cm^3]	band gap [eV]
C_{14}MIN515	0.45	100.0	2.98	6.42
C_{10}MIN183	0.47	100.0	2.98	4.20
C_6MIN32	0.50	100.0	2.91	9.07
C_8MIN171	0.60	100.0	2.97	6.29

3-5. CONCLUSION

In this study, 14265 structural list of carbon crystal structures were generated by PBC/AFIR method and related properties (sp^3/sp^2 ratio, density, band gap) were calculated. The obtained structural data list includes the previously reported structures. According to the energy distribution of the structures, efficient searches for low-lying structures were performed. Interesting structures were found by searching the data list with four search conditions based on properties. Furthermore, this approach, in principle, is applicable to any periodic system. The vast amount of data obtained by this approach would be useful for materials informatics.

3-6. APPENDIX

A3-1. The numbers of overlap structures and artifact structures

The numbers of overlap structures and artifact structures is shown in **Table. A3-1.** In the case of atoms in the unit cell is odd (C_{2i+1}), the proportion of artifact structures tends to be larger than the case of atoms in the unit cell is even (C_{2i}).

Table. A3-1. The numbers of obtained structures for C_1-C_{16}/unit-cell. Number of the obtained structures (N_{search}), Number of the overlap structures ($N_{overlup}$), Number of the overlap structures ($N_{artifact}$), and Number of the total structures (N_{tot}).

Composition [unit-cell]	N_{search}	$N_{overlup}$	$N_{artifact}$	N_{tot}
C_1	13	0	1	12
C_2	7	1	4	3
C_3	53	6	48	5
C_4	50	1	22	27
C_5	185	9	127	58
C_6	253	9	56	188
C_7	577	48	337	227
C_8	983	44	245	703
C_9	1001	51	461	534
C_{10}	1572	49	506	1042
C_{11}	2006	123	1960	1017
C_{12}	2102	54	601	1449
C_{13}	2784	150	1157	1605
C_{14}	2698	51	980	1675
C_{15}	4018	290	1689	2289
C_{16}	5519	161	1937	3431
Total	23821	1047	10131	14265

A3-2. Artifact structures of carbon crystal

Many of artifact carbon crystal structures have features the following; they have partial structure(s) with (i) carbine type or (ii) methyl radical type or in close proximity each other (**Fig. A3-1**). The distance between the partial structures to themselves in adjacent cells is close because of the elongated cell. However, as the degrees of freedom are not enough to describe it, they could not react with each other. So, the structures easily change in the super-cell. For these types of artifact structures, their density is almost the same as the corresponding $MIN_{super\text{-}cell}$. However, their band gap tends to be small because the partial structures having radical-like character are periodically arranged.

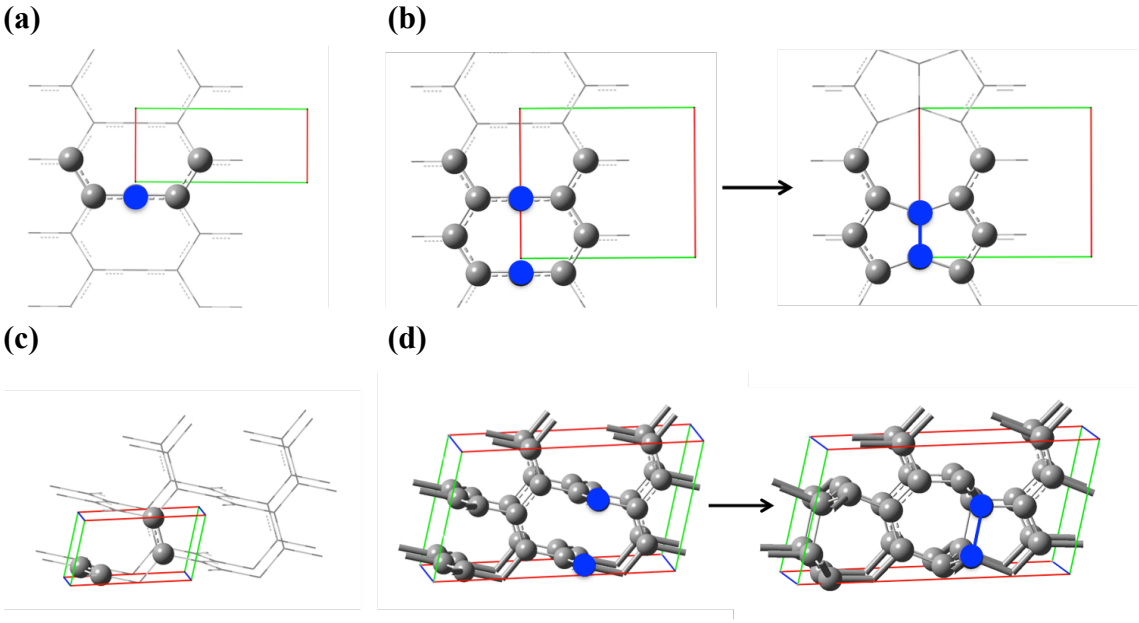

Figure A3-1. Schematic of main artifact structure of carbon crystal. (a)(b) carybene type. (c)(d) metyle radical type. In the case of small unit-cell (a)(b), it is the minimum on the PES. However, in the case of super-cell (c)(d), the structures easily change.

3-7. REFERENCE

[1] A. R. Oganov and C. W. Glass, J. Chem. Phys. **124**, 244704 (2006).

[2] Q. Li, Y. Ma, A. R. Oganov, H. Wang, H. Wang, Y. Xu, T. Cui, H.-K. Mao, and G. Zou, Phys. Rev. Lett. **102**, 175506 (2009).

[3] Z. Zhao, B. Xu, X.-F. Zhou, L.-M. Wang, B. Wen, J. He, Z. Liu, H.-T. Wang, and Y. Tian, Phys. Rev. Lett. **107**, 215502 (2011).

[4] M. Amsler *et al.*, Phys. Rev. Lett. **108**, 065501 (2012).

[5] R. Hoffmann, A. A. Kabanov, A. A. Golov, and D. M. Proserpio, Angew. Chem. Int. Ed. **55**, 10962 (2016).

[6] SACADA, http://sacada.sctms.ru.

[7] The Novel Materials Discovery (NOMAD) Laboratory, https://nomad-coe.eu.

[8] MatNavi, https://mits.nims.go.jp.

[9] D. J. Wales and H. A. Scheraga, Science **285**, 1368 (1999).

[10] K. Sanderson, Nature **450**, 771 (2007).

[11] A. R. Oganov, *Modern Methods of Crystal Structure Prediction* (John Wiley & Sons, Hoboken, NJ, , 2011).

[12] C. J. Pickard and R. J. Needs, Journal of Physics-Condensed Matter **23**, 053201 (2011).

[13] M. Takagi, T. Taketsugu, H. Kino, Y. Tateyama, K. Terakura, and S. Maeda, Phys. Rev. B **95**, 11, 184110 (2017).

[14] S. Maeda, Y. Harabuchi, M. Takagi, K. Saita, K. Suzuki, T. Ichino, Y. Sumiya, K. Sugiyama, and Y. Ono, J. Comput. Chem. **39**, 233 (2018).

[15] development version of GRRM.

[16] M. Elstner, D. Porezag, G. Jungnickel, J. Elsner, M. Haugk, T. Frauenheim, S. Suhai, and G. Seifert, Phys. Rev. B **58**, 7260 (1998).

[17] C. Kohler and T. Frauenheim, Surf. Sci. **600**, 453 (2006).

[18] S. Grimme, J. Comput. Chem. **27**, 1787 (2006).

[19] B. Aradi, B. Hourahine, and T. Frauenheim, J. Phys. Chem. A **111**, 5678 (2007).

[20] dftb+, http://www.dftbplus.org/about-dftb/.

[21] B. B. Zvyagin, Comput. Math. Appl. **16**, 569 (1988).

[22] S. Bahmann, T. Weissbach, and J. Kortus, Physica Status

Solidi-Rapid Research Letters **7**, 639 (2013).

[23] Y. Z. Lin, Z. S. Zhao, T. A. Strobel, and R. E. Cohen, Phys. Rev. B **95**, 1, 039903(e) (2017).

[24] M. Hu *et al.*, Sci. Adv. **3**, 7, e1603213 (2017).

[25] X. Dong, M. Hu, J. L. He, Y. J. Tian, and H. T. Wang, Sci. Rep. **5**, 7, 10713 (2015).

[26] Z. Zhao, B. Xu, L.-M. Wang, X.-F. Zhou, J. He, Z. Liu, H.-T. Wang, and Y. Tian, Acs Nano **5**, 7226 (2011).

[27] R. H. Baughman and D. S. Galvao, Chem. Phys. Lett. **211**, 110 (1993).

[28] P. A. Schultz, K. Leung, and E. B. Stechel, Phys. Rev. B **59**, 733 (1999).

[29] K. Umemoto, R. M. Wentzcovitch, S. Saito, and T. Miyake, Phys. Rev. Lett. **104**, 125504 (2010).

[30] H. S. Domingos, Journal of Physics-Condensed Matter **16**, 9083, Pii s0953-8984(04)81075-0 (2004).

[31] R. H. Baughman, A. Y. Liu, C. Cui, and P. J. Schields, Synth. Met. **86**, 2371 (1997).

[32] J. V. Badding and T. J. Scheidemantel, Solid State Commun. **122**, 473, Pii s0038-1098(02)00136-9 (2002).

[33] R. T. Strong, C. J. Pickard, V. Milman, G. Thimm, and B. Winkler, Phys. Rev. B **70**, 045101 (2004).

[34] X.-F. Zhou, G.-R. Qian, X. Dong, L. Zhang, Y. Tian, and H.-T. Wang, Phys. Rev. B **82**, 134126 (2010).

[35] V. A. Greshnyakov and E. A. Belenkov, Journal of Experimental and Theoretical Physics **113**, 86 (2011).

[36] F. J. Ribeiro, P. Tangney, S. G. Louie, and M. L. Cohen, Phys. Rev. B **72**, 214109 (2005).

[37] A. T. Balaban, C. C. Rentia, and E. Ciupitu, Rev. Roum. Chim. **13**, 231 (1968).

[38] F. J. Ribeiro, P. Tangney, S. G. Louie, and M. L. Cohen, Phys. Rev. B **74**, 4, 172101 (2006).

[39] H. J. Cui, Q. B. Yan, X. L. Sheng, D. L. Wang, Q. R. Zheng, and G. Su, Carbon **120**, 89 (2017).

[40] C. J. Pickard and R. J. Needs, Phys. Rev. B **81**, 5, 014106 (2010).

[41] M. Hu *et al.*, Sci. Rep. **3**, 7, 1331 (2013).

Chapter 4.

Global Phase-transition Route Mapping using the artificial force induced reaction method: A case study on carbon

Abstract: In this chapter, the phase transition network of C_4/unit-cell was generated by PBC/AFIR method. Even though such a small system, 95 local minima and 1087 transition states were obtained. The phase transition pathways from diamond were also discussed. The fastest decay path of diamond is the path to graphite that is consistent with previous studies. In this approach, crystal structure search and phase transition pathway search are performed at the same time. Therefore it is able to apply this method to an unknown system. Any crystal phase transition such as heteroatoms or molecular crystals could be treated by the same procedure.

4-1. INTRODUCTION

In the previous chapters, crystal structure search by PBC/AFIR method and its application are focused. In this chapter, not only crystal structure search but also phase transition paths (in this chapter, it is defined as a first order saddle point on the potential energy surface (PES) with periodic boundary conditions (PBCs)) search by PBC/AFIR method is performed. A phase transition path of a material includes the information, which could not be obtained from only crystal structures, about synthetic paths and kinetic stability. Therefore, searching phase transition path is also an important subject. In the conventional method, nudged elastic band (NEB) method[1] and molecular dynamics (MD) simulation[2] were commonly used. How ever, in the case of NEB method, the calculator should specify a starting point and end point. So, it is difficult to apply to unknown systems. In MD simulation, it is difficult to apply to the system including multi-timescale reactions such as global phase-transition map. On the other hands, the AFIR method[3] has been applied extensively to molecular systems to elucidate the mechanism of chemical reactions such as homogeneous catalysis. There are no limitations on timescale. More over this method can be applied to unknown system because by exhaustive searches. AFIR method has been extended to the Periodic boundary systems (PBC/AFIR method) as described in **Chapter 2** and this framework can be applied to not only crystal structure searches but also phase-transition searches.

In this study, the global phase transition map of the carbon crystal described by four carbon atoms in the unit-cell (C_4/unit-cell) is created by PBC/AFIR method.

4-2. METHOD

4-2-1. PBC/AFIR method

The settings of AFIR method are almost same as the one in **Chapter 2**. However, in this study, exhaustive search was performed, i.e., no stochastic search options were used. In the other word, AFIR method applied to all obtained structures. All calculations were performed with a developmental version of the GRRM program[4].

4-2-2. Electronic structure calculation

SIESTA3.2[5-7] was used to compute the energy, force acting on atoms, and stress tensor acting on a unit-cell. These calculations were performed using density functional theory (DFT) with the PBE functional and the DZP basis set. Grimme's dispersion

correction[8], with the parameters R_0 = 2.904 Å and $C6$ = 4.0 kJ·Å^6·mol^{-1}, was added, where the value of $C6$ was adjusted so that the present computation reproduced the inter-layer distance of graphite of 3.4 Å. The pseudopotential of carbon was prepared using the parameters in the GGA Pseudopotential Database[9], where the core correction was not considered. A Monkhorst–Pack grid was set to 4×4×4 for the *k*-point sampling. Collinear spin alignment was taken into account. The electronic temperature was set to 5.0 K. The mesh cutoff value was set to 50.0 Ry. When determining the transition state, numerical differentiation of energy was used for Hessian calculation on the transition vectors (TVs).

4-2-3. Computational procedures

The concrete procedure in this study of searching for carbon crystal structures and the reaction paths between systems proceeds along the following three steps.

(a) Generate an initial structure in the each system by optimizing a diamond structure (C_4/unit-cell).

(b) Search for MINs and approximate TSs with the C_4/unit-cell by the SC-AFIR starting from the diamond structure optimized in step (a).

(c) Approximate TSs are optimized by Locally update plane method (LUP) method. [10]

4-3. RESULTS AND DISCUSSION

4-3-1. Global Phase-transition Route Map of C_4/unit-cell

The present PBC/AFIR approach generated 95 local minima and 1087 transition states for C_4/unit-cell. 119 paths are obtained by put together the paths that connect the same MIN pair. The global phase-transition network of C_4/unit-cell is shown in **Fig. 4-1**. Nodes and edges correspond to crystal structures and phase-transition paths, respectively. The *N*th lowest min is labeled as min*N*. This *N* is printed in the corresponding node in the map. Colors of nodes and edges correspond to the energy of the structures. The MINs that has no connections and the paths returning back to the same MIN are omitted. Even though such a small system, the network is complicated. This network includes present reported structures, such as graphite (**min0**, **min1**, **min2**), diamond (**min3**), lonsdaleite (hexagonal diamond, **min4**) and Isoglitter[11], 8-tetra(2,2) tubulane or bct C_4 (**min5**),[12-21] network7 (**min8**),[22-27] a hypothetical metallic allotrope of carbon or bct-4 carbon (**min11**)[28-32] and others. The representative structures emphasized with black line in the map of **Fig. 4-1** are shown in **Fig. 4-2**. Lower energy structures were same as the structures described C_4/unit-cell in **Chapter 2.** The higher energy structures, depicted on the right hand side of the map, were almost carbyne or layered structures that have many stacking types.

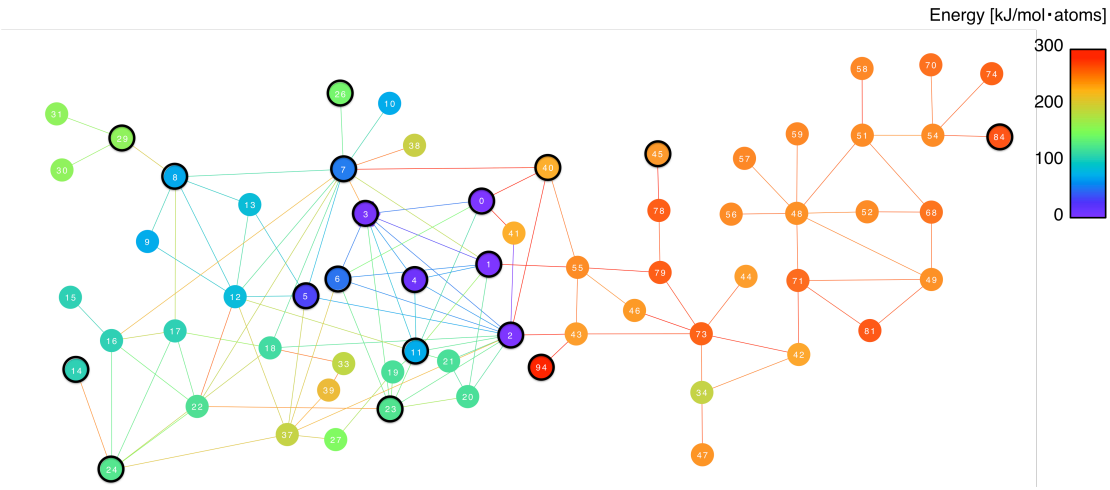

Figure. 4-1. Global Phase-transition Route Map of Carbon Crystal (C_4/unit-cell). Nodes and edges correspond to crystal structures and phase-transition paths, respectively. The *N*th lowest min is labeled as min*N*. This *N* is printed in the corresponding node in the map. Colors of nodes and edges correspond to the energy of the structures. The network was drawn by using Cytoscape software.[33]

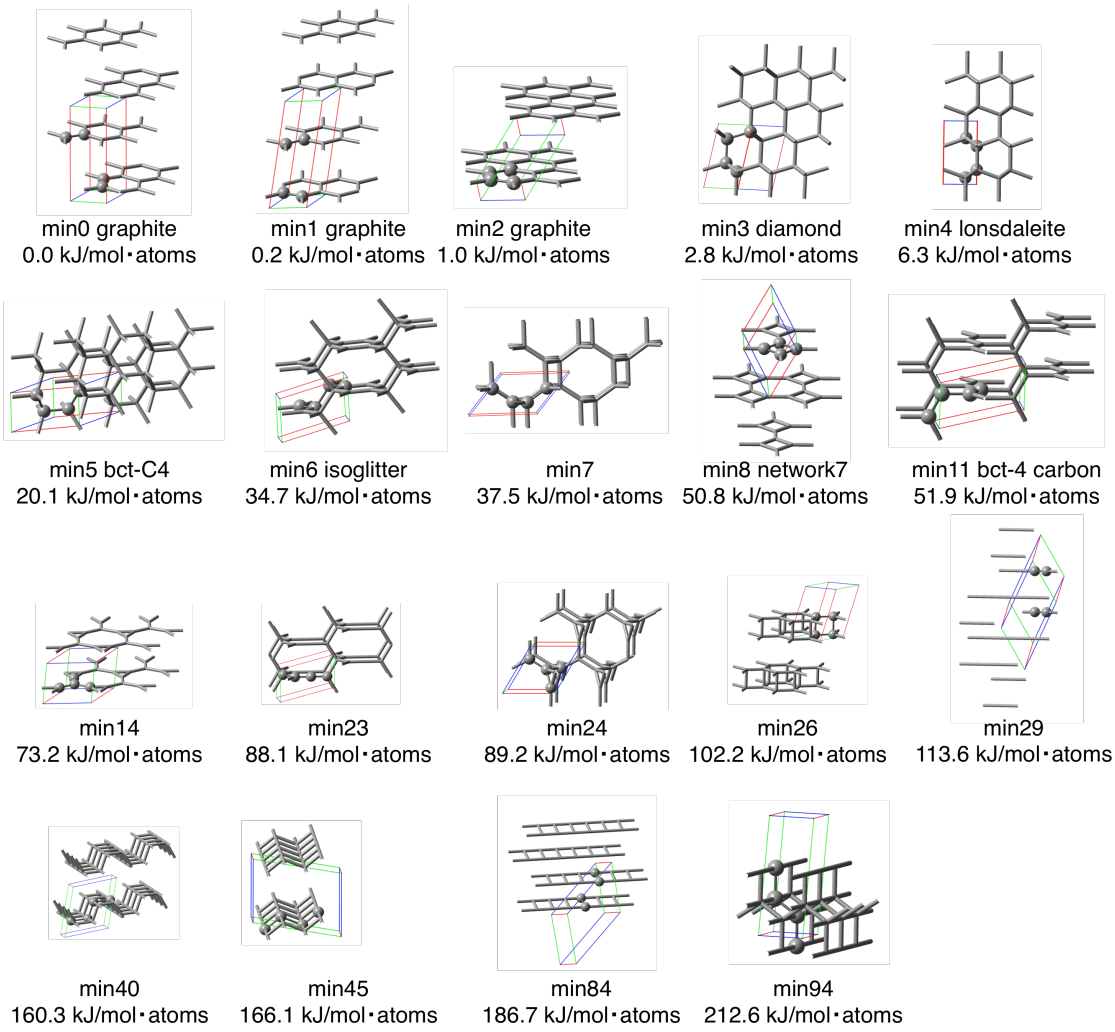

Figure 4-2. The representative structures in the map. The names of structures (if available), relative energies are shown in the labels. TVs are shown as red, green, and blue lines. Atoms in a unit-cell are highlighted by the ball model.

4-3-2. The paths connected from diamond

There are eight paths connected from diamond. Energy diagram of the eight paths are shown in **Fig. 4-3**. Structures of TSs and reacted structures are shown in **Fig. 4-4**. Here, the TS which connect MIN*i* and MIN*j* is termed TS*i*/*j*. The three of the lower energy pathways described the phase transition of diamond to graphite. In these three cases, even though the shapes of cells for diamond are different for each other, the shapes of TS structures are almost same. The barrier height is about 36.1 kJ/mol・atoms and this value is in good agreement with the ones of the previous study.[34] The dependence of cell shapes is discussed in the next chapter. The next fastest path is the path that connected to the isoglitter (36.3 kJ/mol・atoms). However, this pathway is not important for diamond because isoglitter is less stable than diamond so that the reaction rate constant of diamond to isoglitter is smaller than the reaction ratio return form isoglitter to diamond. The minimum energy path of diamond to a stable structure than the one is the diamond-graphite. This result is in good agreement with the fact that diamond is kinetically stable in the real system. The paths that connect diamond to lonsdaleite and bct-C_4 carbon were also obtained.

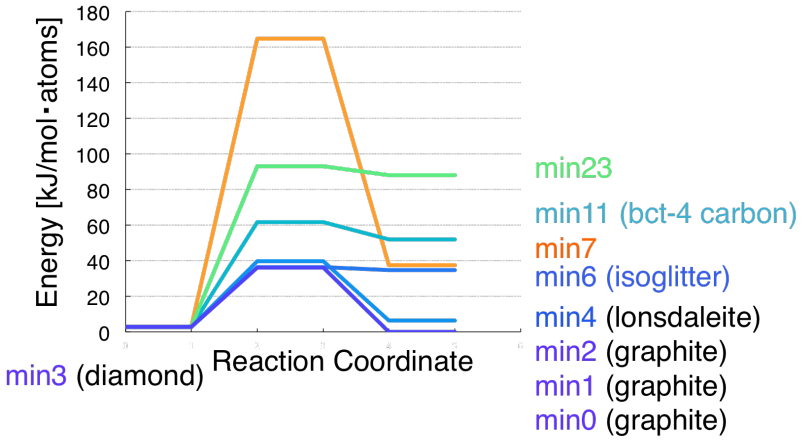

Figure 4-3. The energy diagram of the paths from diamond to other structures.

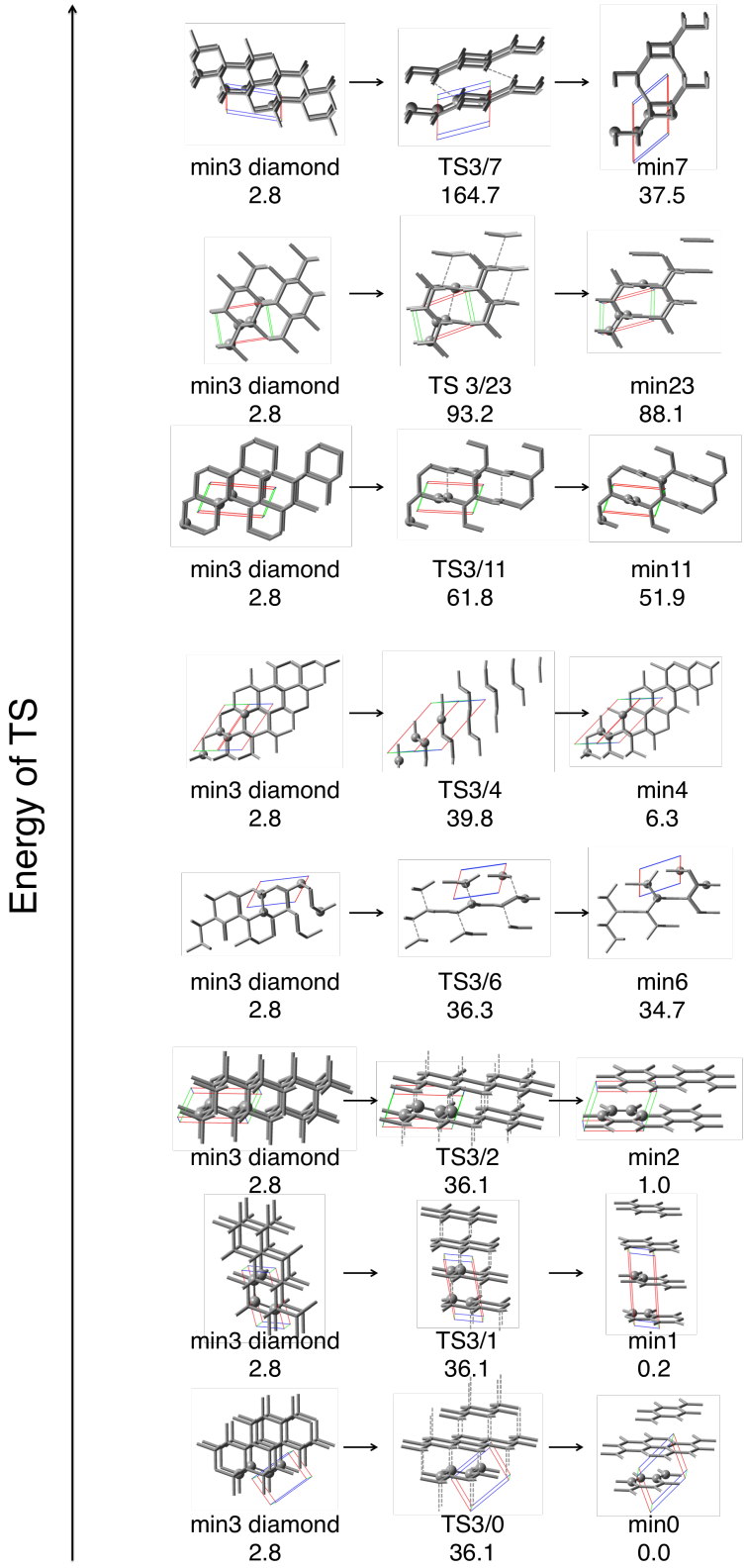

Figure 4-4. The structures along the paths from diamond (left hand side) to other structures.

4-4. CONCLUSION

The phase transition network of C_4/unit-cell was generated by PBC/AFIR method. Even though such a small system, 95 local minima and 1087 transition states were obtained. The phase transition pathways from diamond were also discussed. The fastest decay path of diamond was diamond to graphite that was consistent with previous studies.

In this framework, crystal structure search and phase transition pathway search are performed at the same time. Therefore it is able to apply this method to an unknown system. Any crystal phase transition such as heteroatoms or molecular crystals could be treated by the same procedure.

4-5. REFERENCE

[1] D. Sheppard, P. H. Xiao, W. Chemelewski, D. D. Johnson, and G. Henkelman, J. Chem. Phys. **136**, 8, 074103 (2012).

[2] M. Iannuzzi, A. Laio, and M. Parrinello, Phys. Rev. Lett. **90**, 4, 238302 (2003).

[3] S. Maeda, Y. Harabuchi, M. Takagi, K. Saita, K. Suzuki, T. Ichino, Y. Sumiya, K. Sugiyama, and Y. Ono, J. Comput. Chem. **39**, 233 (2018).

[4] development version of GRRM.

[5] D. SanchezPortal, P. Ordejon, E. Artacho, and J. M. Soler, Int. J. Quantum Chem **65**, 453 (1997).

[6] J. M. Soler, E. Artacho, J. D. Gale, A. Garcia, J. Junquera, P. Ordejon, and D. Sanchez-Portal, Journal of Physics-Condensed Matter **14**, 2745, Pii s0953-8984(02)30737-9 (2002).

[7] D. Sanchez-Portal, P. Ordejon, and E. Canadell, in *Principles and Applications of Density in Inorganic Chemistry Ii*, edited by N. Kaltsoyannis, and J. E. McGrady2004), pp. 103.

[8] S. Grimme, J. Comput. Chem. **27**, 1787 (2006).

[9] GGA Pseudopotential Database, http://departments.icmab.es/leem/siesta/Databases/Pseudopotentials/periodictable-gga-abinit.html (Accessed accessed May 3, 2016).

[10] C. Choi and R. Elber, J. Chem. Phys. **94**, 751 (1991).

[11] M. J. Bucknum, E. A. Castro, and B. Wen, J. Math. Chem. **50**, 2281 (2012).

[12] R. H. Baughman and D. S. Galvao, Chem. Phys. Lett. **211**, 110 (1993).

[13] P. A. Schultz, K. Leung, and E. B. Stechel, Phys. Rev. B **59**, 733 (1999).

[14] K. Umemoto, R. M. Wentzcovitch, S. Saito, and T. Miyake, Phys. Rev. Lett. **104**, 125504 (2010).

[15] H. S. Domingos, Journal of Physics-Condensed Matter **16**, 9083, Pii s0953-8984(04)81075-0 (2004).

[16] R. H. Baughman, A. Y. Liu, C. Cui, and P. J. Schields, Synth. Met. **86**, 2371 (1997).

[17] J. V. Badding and T. J. Scheidemantel, Solid State Commun. **122**, 473,

Pii s0038-1098(02)00136-9 (2002).

[18] R. T. Strong, C. J. Pickard, V. Milman, G. Thimm, and B. Winkler, Phys. Rev. B **70**, 045101 (2004).

[19] X.-F. Zhou, G.-R. Qian, X. Dong, L. Zhang, Y. Tian, and H.-T. Wang, Phys. Rev. B **82**, 134126 (2010).

[20] V. A. Greshnyakov and E. A. Belenkov, Journal of Experimental and Theoretical Physics **113**, 86 (2011).

[21] Z. Zhao, B. Xu, L.-M. Wang, X.-F. Zhou, J. He, Z. Liu, H.-T. Wang, and Y. Tian, Acs Nano **5**, 7226 (2011).

[22] A. T. Balaban, C. C. Rentia, and E. Ciupitu, Rev. Roum. Chim. **13**, 231 (1968).

[23] H. Y. Zhu, A. T. Balaban, D. J. Klein, and T. P. Zivkovic, J. Chem. Phys. **101**, 5281 (1994).

[24] M. J. Bucknum and E. A. Castro, Solid State Sciences **10**, 1245 (2008).

[25] X.-Q. Wang, H.-D. Li, and J.-T. Wang, Phys. Chem. Chem. Phys. **14**, 11107 (2012).

[26] X.-L. Sheng, H.-J. Cui, F. Ye, Q.-B. Yan, Q.-R. Zheng, and G. Su, J. Appl. Phys. **112**, 074315 (2012).

[27] Z. Zhu and D. Tomanek, Phys. Rev. Lett. **109**, 135501 (2012).

[28] A. R. Oganov and C. W. Glass, J. Chem. Phys. **124**, 244704 (2006).

[29] R. Hoffmann, T. Hughbanks, M. Kertesz, and P. H. Bird, JACS **105**, 4831 (1983).

[30] G. M. Rignanese and J. C. Charlier, Phys. Rev. B **78**, 125415 (2008).

[31] R. H. Baughman and D. S. Galvao, Nature **365**, 735 (1993).

[32] M. J. Xing, B. H. Li, Z. T. Yu, and Q. Chen, Commun. Theor. Phys. **64**, 237 (2015).

[33] Cytoscape (Version 3.5.1), The Cytoscape Consortium, http://www.cytoscape.org/.

[34] Y. Tateyama, T. Ogitsu, K. Kusakabe, and S. Tsuneyuki, Phys. Rev. B **54**, 14994 (1996).

Chapter 5.

Kinetic stability prediction of a crystal by PBC/AFIR method: an application to the Cco-C_8 (*Z*-carbon)

Abstract: In this chapter, the kinetic stability of the Cco-C_8 (or *Z*-carbon) that predicted theoretically by previous studies was discussed by PBC/AFIR methods. In a small cell, there is cell shape dependence of decay paths. In this study, C_{16}-conv and its super cell C_{32}-conv has the lower energy pathways. The lifetime estimated by these pathways are 4.5×10^{20} [s] and these results indicate that Cco-C_8 will be kinetic stable, i.e. this structure might be synthesized. Note that there is a possibility that faster decay path exists in larger super-cells. As shown in this study, this approach can be discussed the kinetic stability of a material which predicted theoretically. The true lifetime of the material would be less than the lifetime estimated by targeted system because there is a possibility that it is exists that the faster decay path that could not described in targeted system. Therefore, it can be expected that it can be utilized as one of filters to estimate the lifetime of material.

5-1. INTRODUCTION

In general, it is necessary to be kinetically stable for use as a material. One of the most famous kinetically stable materials is diamond. Note that diamond is unstable than graphite thermodynamically. It is relatively easy to show that a material is kinetically unstable, i.e., it is necessary to show that there is at least one possible decay path. On the other hands, if a material is kinetically stable, it is necessary to show that there is no decay pathway that can occur within the considered timescale. Such a discussion is difficult with the conventional method, and the stability of the material has been discussed only on the thermodynamic stability. Recently, many carbon crystal structures are predicted theoretically[1,2]. Among them, one of the most famous structures is Cco-C_8 (or *Z*-carbon) which reported in 2011 by Zhao *et al.*[3] and Amsler *et al.*[4] The conventional unit cellof Cco-C_8 is shown in **Fig. 5-1**. Cco-C_8 is composed of only sp^3 carbon and the structure contains four-, six- and eight- membered rings. From the view along *b*-axis, the structure is similar to diamond, and only six-membered rings are visible (**Fig. 5-1(b)**). From the view along *c*-axis, all of four-, six- and eight-membered rings are visible (**Fig. 5-1(c)**). However, to the best of our knowledge, the synthesis of Cco-C_8 has not been achieved yet. In previous studies, thermodynamic stability, stability analysis by phonon, stability to pressure, etc., have been investigated, whether Cco-C_8 is kinetically stable is unknown. There is no limit to the time scale that can be handled with the AFIR method, [5] and reaction paths of any reaction can be exhaustively searched. Phase-transition path search can be performed by PBC/AFIR method[6] as shown in the **Chapter 4**.

In this study, kinetic stability of Cco-C_8 is discussed based on minimum energy phase-transition pathways by using PBC/AFIR method. The dependence of a cell shape and cell size is also discussed.

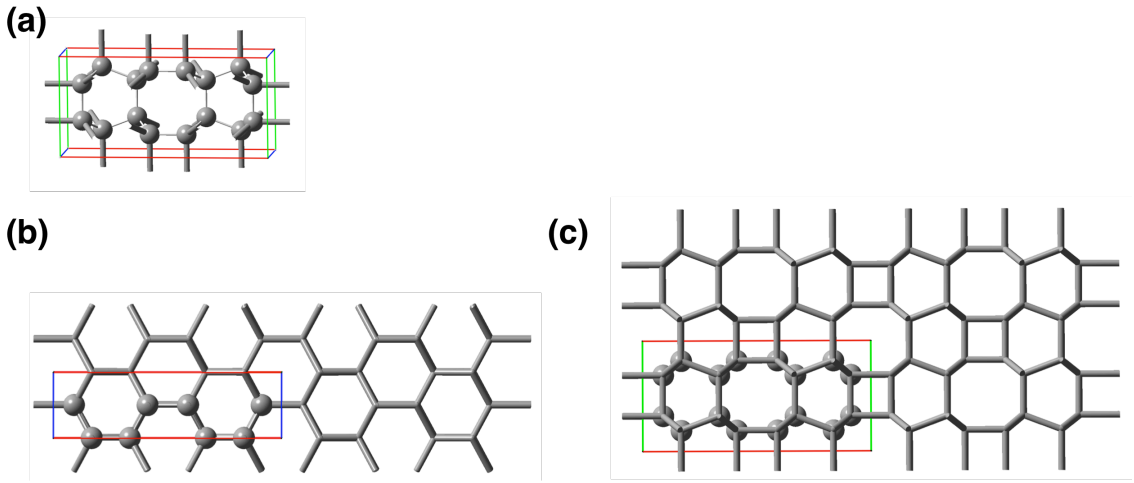

Figure 5-1. (a) Conventional cell described by C_{16}/unit-cell. 2×2×2 super cell of Cco-C_8. The view along (b) *b*-axis, (c) *c*-axis. TVs are shown as red, green, and blue lines. Atoms in a unit-cell are highlighted by the ball model.

5-2. METHOD

5-2-1. Efficient search for the decay paths

As a decay path, the path that has lower energy barrier is important. Moreover, the path is necessary to connect to lower energy structure than target structure. In some case, the decay path is multi step reaction. So, the path search should be applied to a structures, which has higher energy than the target structure (**Fig. 5-2**). Recently, Sumiya *et al*. proposed an efficient search method of the decay path of target structure by using the rate constant matrix contraction (RCMC) method.[7,8] RCMC method is a method for making coarse-graining network by distributes the population of nodes to the others (fuzzy clustering). Finally, the network including super states (SSs) that belonged one or more structures, and edges connecting SSs are obtained. It is common to use the method of reducing the rate constant from the fastest node. In order to search decay path efficiently, RCMC method is applied only the MIN satisfied following condition. Then, AFIR method applied only the structures belonging to the SS including the input (target) structure (MIN_{target}); (1) the MIN is not MIN_{target}, (2) the MIN has a connection to the SS including MIN_{target}, (3) the MIN is (thermodynamically) unstable than MIN_{target}, (4) the MIN is accessible from the SS including MIN_{target} within a timescale $10t_0$, where t_0 is the lifetime of the SS including MIN_{target} estimated by the rate

constant of the fastest escaping path from the SS. In this study, an efficient minimum energy phase-transition pathway search were performed by connecting this method and PBC/AFIR method.

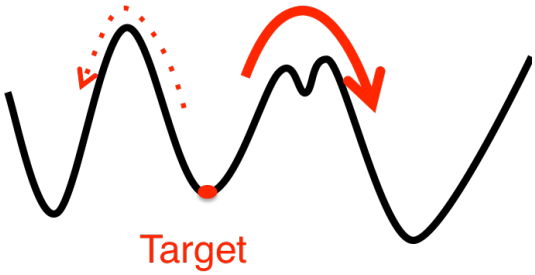

Figure 5-2. Schematic of decay paths.

5-2-2. Electronic structure calculation

The electric structure calculation were SCC-DFTB calculation[9] by using DFTB3/pbc-0-3 parameter and empirical dispersion (D3).[10] The pbc-0-3 parameter[11] have been adjusted for DFTB2, but we found a problem that is underestimation of the energy of carbyne[12] by using these combination and empirical dispersion (D2). The *k*-point sampling for Monkhorst–Pack is set to 4×4×4. Electronic state calculation was performed with the dftb+ program.[13,14] When determining the transition state, numerical differentiation of energy was used for Hessian calculation on the transition vectors (TVs).

5-2-3. Energy corrections

In this calculation level, diamond is stable than graphite. To correct the energy difference between diamond and graphite to the experimental value 2.89 kJ/mol, we assumed virtual pressure,

$$E_{\mathrm{corr}} = E + PV, \tag{2}$$

where E_{corr} is the corrected energy, E is the electronic energy, P is pseudo pressure and the value -6.66 is adopted, and V is the volume of the structure (unit-cell).

In general, in the case of discussing energy of crystal, energy per atoms, for example [eV/atoms(・unit-cell)], is commonly used. This energy should be converted to estimate the reaction rate constant based on the steady-state approximation (transition-state theory),

$$k_{i\to j} = \frac{k_B \cdot T}{\hbar} exp(\frac{\Delta E_{i\to j}}{RT}), \quad (1)$$

where R is the gas constant, T is the temperature, k_B is the Boltzmann constant, and $\hbar$ is the reduced Planck constant. To use this equation, the unit conversion of energy is required. In this study, a barrier of diamond-graphite (30.1 kJ/mol・atoms) is corrected to the experimental value 728 kJ/mol[15] by multiplying the coefficient (24.1 atoms).

5-2-4. Computational procedures

The concrete procedure in this study of searching for carbon crystal structures and the reaction pathways between systems proceeds along the following four steps.

(a) Optimize the Cco-C_8 structures.

(b) Search for MINs and approximate TSs by the SC-AFIR starting from the initial structure optimized in step (a).

(c) Approximate TSs are optimized by Locally update plane method (LUP) method.[16]

(d) The energies of structures are corrected by in Section **5-2-2.**

5-3. RESULTS AND DISCUSSION

5-3-1. Minimum energy paths described by C_8/unit-cell and C_{16}/unit-cell

Phase-transition pathway search by PBC/AFIR method were performed for bellow five-type of unit-cells of Cco-C_8 that depicted in **Fig. 5-3**; a primitive cell (C_8-prim), super-cells of C_8-prim elongated along *a*-axis, *b*-axis, *c*-axis, respectively (C_{16}-a, C_{16}-b, C_{16}-c). And conventional-cell recorded in the SACADA (C_{16}-conv).

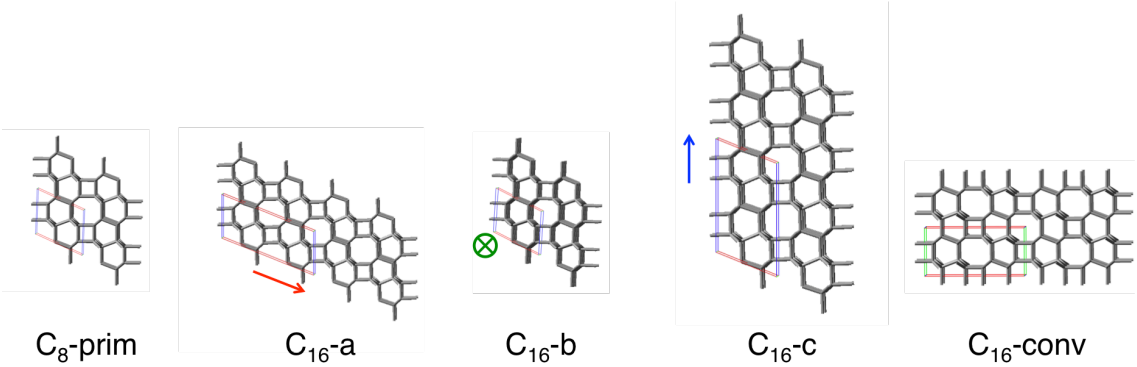

Figure 5-3. Five types of unit-cells of Cco-C_8. TVs are shown as red, green, and blue lines. Atoms in a unit-cell are highlighted by the ball model.

In the **table 5-1**, the number of obtained structure (N_{MIN}) and obtained pathways (N_{path}), the barrier height of the minimum energy decay path (ΔE), lifetime at 300 K (t) in each composition are shown. The structures along the barrier height of the minimum energy decay paths are shown in **Fig. 5-4**.

Table 5-1. The number of obtained structure (N_{MIN}) and obtained pathways (N_{path}), the barrier height of the minimum energy decay path (ΔE), lifetime at 300 K (t) in each cell shapes.

Cell shape	N_{MIN}	N_{path}	Δ E [kJ/mol]	t [s]
C_8-prim	143	444	578.2	1.9×10^{65}
C_{16}-a	1342	2942	521.2	2.6×10^{50}
C_{16}-b	114	201	571.9	3.3×10^{65}
C_{16}-c	834	1425	539.2	3.9×10^{57}
C_{16}-conv	892	1796	308.0	6.7×10^{24}

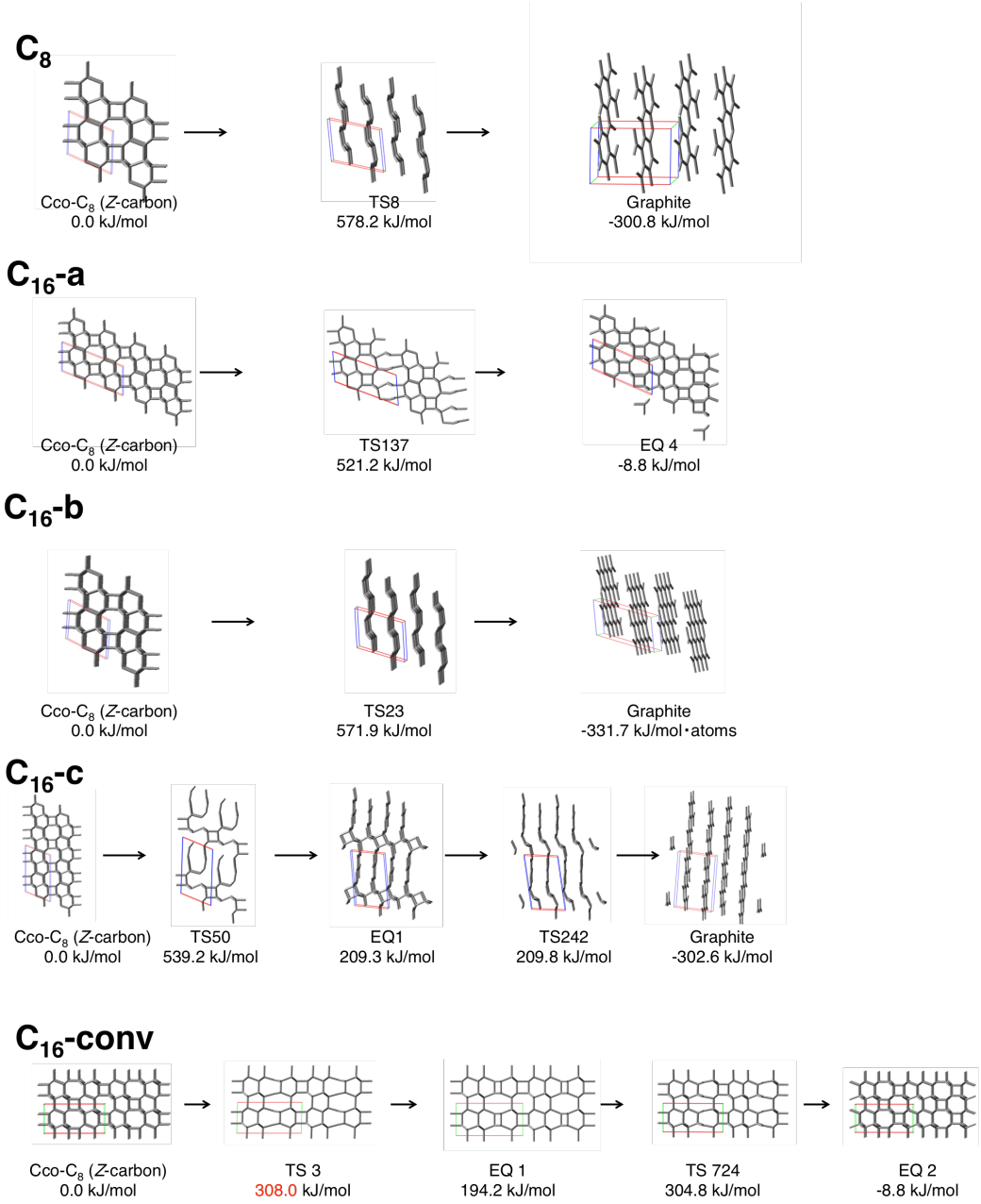

Figure 5-4. The structures along the barrier height of the minimum energy decay path for each cell shape. TVs are shown as red, green, and blue lines. Atoms in a unit-cell are highlighted by the ball model.

In the case of C_8-prim and C_{16}-b, Cco-C_8 decay to graphite directory. This path is reversed process of proposed synthetic path of Cco-C_8.[4] The barrier height of this path is 578.2 kJ/mol and 571.9 kJ/mol, respectively and the lifetime calculated from eq. (1) is 1.9 $\times 10^{65}$ [s] and 3.3 $\times 10^{65}$ [s]. C_{16}-c has a multi-step pathway that collapses

into graphite, which has a lower barrier (521.2 kJ/mol) than the former direct decay path. On the other hands, C_{16}-a has other pathway that the line of four- and eight- membered rings shifting directory to neighbor line of six- membered rings (shifting 4-8 membered rings). The path of C_{16}-conv is same type of shifting 4-8 membered rings, but in this case, through the intermediate (**Im1**) and has lowest barrier height of the five types. A schematic of shifting 4-8 membered rings in C_{16}-conv is shown in **Fig. 5-5**. As shown here, especially when the cell is small, there is a cell shape dependence of decay path.

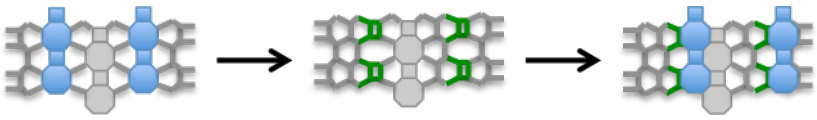

Figure 5-5. A schematic of a minimum energy decay path of C_{16}-conv (shifting four- and eight-membered rings).

5-3-2. Map of C_{16}-conv

Phase-transition pathway map of C_{16}-conv, which has the fastest decay path, is shown in **Fig. 5-6**. Nodes and edges correspond to crystal structures and phase-transition pathways, respectively. The *N*th lowest min is labeled as min*N*. This *N* is printed in the corresponding node in the map. Colors of nodes and edges correspond to the energy of the structures. Cco-C_8 is located at the center of the map and described by diamond mark. In the search, five structures that are stable than were obtained. The five structures and Cco-C_8 are shown in **Fig. 5-7**. The most stable structure is graphite, and diamond and lonsdaleite are also obtained. **MIN23** is similar to **Im1** or Cco-C_8 but stable than **Im1** bacause losdaleite domain of **MIN23** is larger than **Im1**.

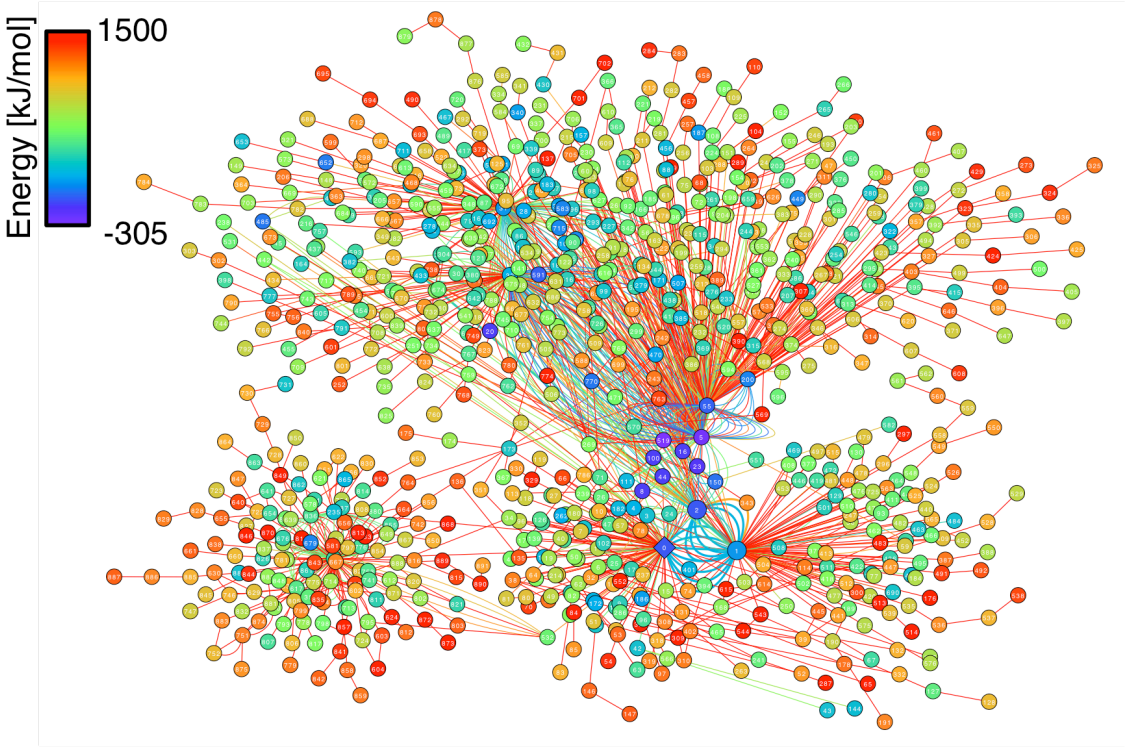

Figure 5-6. The phase-transition map of C_{16}-SACADA. Nodes and edges correspond to crystal structures and phase-transition pathways, respectively. The *N*th lowest min is labeled as min*N*. This *N* is printed in the corresponding node in the map. Colors of nodes and edges correspond to the energy of the structures. The network was drawn by using Cytoscape software.[17]

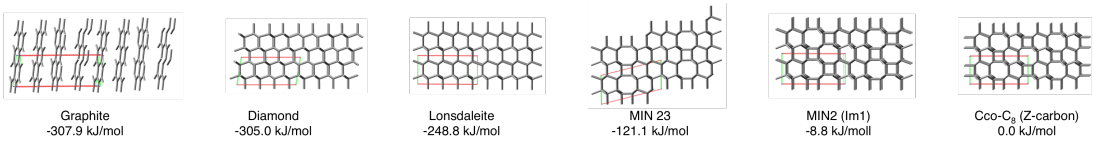

Figure 5-7. The five structures stable than Cco-C_8. The names of structures (if available), relative energies to the Cco-C_8 are shown in the labels. TVs are shown as red, green, and blue lines. Atoms in a unit-cell are highlighted by the ball model.

5-3-3. Minimum energy paths described by C_{32}/unit-cell

C_{32}-conv shown in **Fig. 5-8** is created by extend C_{16}-conv, which has fastest decay path of the five, along shortest axis (*c*-axis). The decay paths of C_{32}-conv are also searched.

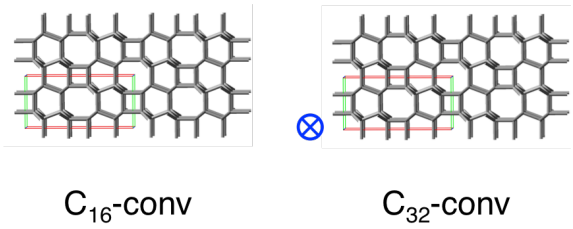

Figure 5-8. The structures of C_{16}-conv and C_{32}-conv. TVs are shown as red, green, and blue lines. Atoms in a unit-cell are highlighted by the ball model.

In the **table 5-2**, the number of obtained structure (N_{MIN}) and obtained pathways (N_{path}), the barrier height of the minimum energy decay path (ΔE), lifetime at 300 K (t) in each composition are shown. The energy diagram of minimum energy decay paths is shown in **Fig. 5-9**. The structures along the minimum energy decay paths are also depicted in **Fig. 5-10**.

The minimum energy decay path of C_{32}-conv is the same type as C_{16}-SACADA, i.e. shifting 4-8 membered rings. In the case of C_{16}-conv, the phase-transition is occurring at the same time. C_{32}-conv is composed from two units of C_{16}-conv. So, these reactions are occur stepwise, i.e., then at first one of the C_{16}-conv becomes **Im1**, then the other part becomes **Im1** and reached **Im1** in total (**Fig. 5-11)**.

In the larger super-cell, the barrier height of this reaction will be decreased by stepwise reactions. However, in this reaction type, the overall barrier height could not be lower than **Im1**. So, assuming this intermediate (**Im1**) as lower limit of the barrier height of this reaction, the lifetime at 300 K is calculated 4.5×10^{20} [s]. According to these results from C_8 to C_{32}, Cco-C_8 seems to be kinetically stable. Note that there is a possibility that other type the more of the fast decay path exists in larger super-cells.

Table 5-2. The number of obtained structure (N_{MIN}) and obtained pathways (N_{path}), the barrier height of the minimum energy decay path (ΔE), lifetime at 300 K (t) in each cell shapes.

Cell shape	N_{MIN}	N_{path}	ΔE [kJ/mol]	t [s]
C_{16}-SACADA	892	1796	308.0	6.7×10^{24}
C_{32}-SACADA	2522	4907	263.2	4.7×10^{19}

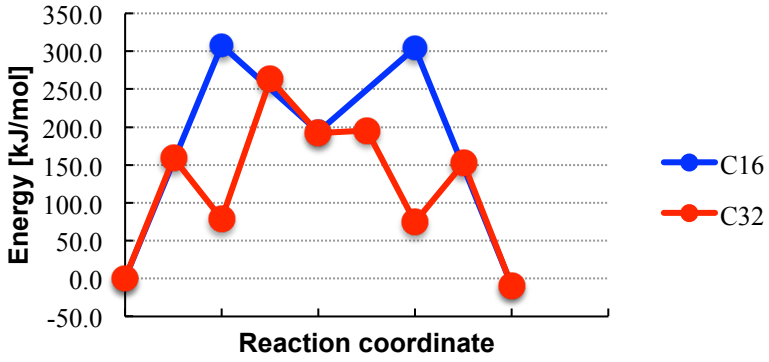

Figure 5-9. The energy diagram of the fastest decay path for C_{16}-conv (blue line) and C_{32}-conv (red line).

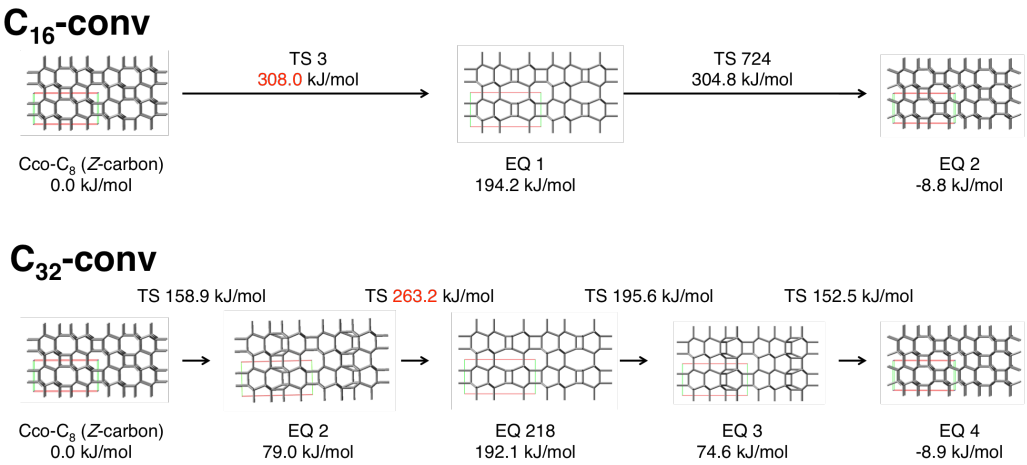

Figure 5-10. The fastest decay path of C_{16}-conv and C_{32}-conv. The names of structures (if available), relative energies to the Cco-C_8 are shown in the labels. TVs are shown as red, green, and blue lines. Atoms in a unit-cell are highlighted by the ball model.

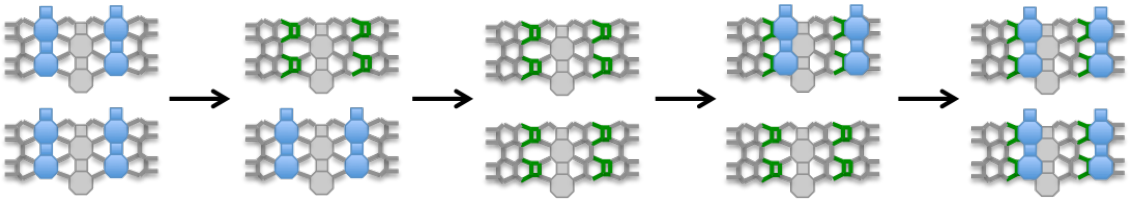

Figure 5-11. A schematic of the fastest decay path of C_{32}-conv.

5-4. CONCLUSION

In this study, the kinetic stability of the Cco-C_8 (or *Z*-carbon) that predicted theoretically by previous studies was discussed by PBC/AFIR method. In such a small cell, there is cell shape dependence of decay paths. In this study, C_{16}-conv and its super cell C_{32}-conv has the lower energy pathways. The lifetime estimated by these pathways are 4.5×10^{20} [s] and these results indicate that Cco-C_8 will be kinetic stable, i.e. this structure might be synthesized. Note that there is a possibility that faster decay path exists in larger super-cells.

As shown in this study, this approach can be discussed the kinetic stability of a material which predicted theoretically. The true lifetime of the material would be less than the lifetime estimated by targeted system because there is a possibility that it is exists that the faster decay path that could not described in targeted system. Therefore, it can be expected that it can be utilized as one of filters to estimate the lifetime of material.

5-5. REFERENCE

[1] SACADA, http://sacada.sctms.ru.

[2] R. Hoffmann, A. A. Kabanov, A. A. Golov, and D. M. Proserpio, Angew. Chem. Int. Ed. **55**, 10962 (2016).

[3] Z. Zhao, B. Xu, X.-F. Zhou, L.-M. Wang, B. Wen, J. He, Z. Liu, H.-T. Wang, and Y. Tian, Phys. Rev. Lett. **107**, 215502 (2011).

[4] M. Amsler *et al.*, Phys. Rev. Lett. **108**, 065501 (2012).

[5] S. Maeda, Y. Harabuchi, M. Takagi, K. Saita, K. Suzuki, T. Ichino, Y. Sumiya, K. Sugiyama, and Y. Ono, J. Comput. Chem. **39**, 233 (2018).

[6] M. Takagi, T. Taketsugu, H. Kino, Y. Tateyama, K. Terakura, and S. Maeda, Phys. Rev. B **95**, 11, 184110 (2017).

[7] Y. Sumiya, Y. Nagahata, T. Komatsuzaki, T. Taketsugu, and S. Maeda, J. Phys. Chem. A **119**, 11641 (2015).

[8] Y. Sumiya and S. Maeda, Chem. Eur. J. **24**, 12264 (2018).

[9] M. Elstner, D. Porezag, G. Jungnickel, J. Elsner, M. Haugk, T. Frauenheim, S. Suhai, and G. Seifert, Phys. Rev. B **58**, 7260 (1998).

[10] S. Grimme, J. Comput. Chem. **27**, 1787 (2006).

[11] C. Kohler and T. Frauenheim, Surf. Sci. **600**, 453 (2006).

[12] L. Shi *et al.*, Nature Materials **15**, 634 (2016).

[13] B. Aradi, B. Hourahine, and T. Frauenheim, J. Phys. Chem. A **111**, 5678 (2007).

[14] dftb+, http://www.dftbplus.org/about-dftb/.

[15] G. Davies and T. Evans, Proc. R. Soc. Lond. A. **328**, 413 (1972).

[16] C. Choi and R. Elber, J. Chem. Phys. **94**, 751 (1991).

[17] Cytoscape (Version 3.5.1), The Cytoscape Consortium, http://www.cytoscape.org/.

Chapter 6.

Exploring potential crossing seams in periodic systems: Intersystem crossing pathways in the benzene crystal

Abstract: The intersystem crossing (ISC) pathways of triplet benzene molecules in a benzene crystal were investigated theoretically. A combination of the gradient projection (GP) method, which is a standard method for optimizing the crossing seam of two potential energy surfaces, and the single-component artificial-force-induced reaction (SC-AFIR) method (GP/SC-AFIR) was used. This is the first reported use of a GP/SC-AFIR calculation using a density functional theory (DFT) calculation with periodic boundary conditions. A systematic search for the minimum-energy structures in the seams of crossing of the singlet (S_0) and triplet (T_1) potential energy surfaces (S_0/T_1-MESX structures) found 39 independent S_0/T_1-MESX structures. Energy barriers between the S_0/T_1-MESX and the stationary structure of the triplet state (T_1-MIN) were computed, and then two competing ISC pathways were extracted; the calculated overall energy barrier to the intermolecular C–C-bonded type (**SX3**) and the out-of-plane bent C–H type (**SX15**) S_0/T_1-MESX structures from T_1-MIN were 0.26 and 0.27 eV, respectively. The rate constants for **SX3** and **SX15** formation were estimated to be 5.07×10^8 and 2.17×10^8 s^{-1} (at 273 K), respectively, or 9.73×10^{-5} and 4.78×10^{-6} s^{-1} (at 77 K), respectively. At 273 K, which is close to the melting point of the benzene crystal (278.5 K), **SX3** and **SX15** are easily accessible from T_1-MIN, and ISC could occur through the S_0/T_1-MESX points. In contrast, at 77 K, T_1-MIN survives long enough for phosphorescence to compete with ISC.

6-1. INTRODUCTION

Molecular luminescence is widely used in optical materials and sensors. In the last decade, organic light-emitting diodes (OLEDs), in particular, have been attracting much attention. In OLEDs, molecules that show phosphorescence[1] or delayed fluorescence[2] can achieve internal quantum efficiencies of 100% because electrically injected charge carriers recombine and singlet and triplet excitons are generated in a 1:3 ratio.[2] Relaxation of the triplet state to the singlet electronic ground state occurs via radiative de-excitation (phosphorescence) or nonradiative decay (intersystem crossing, ISC). Nonradiative relaxation processes occur efficiently near the intersection of two potential energy surfaces.[3-6] The intersection between a triplet- and a singlet-spin state is not an isolated point but rather a $3N - 7$ dimensional seam (where N is the number of atoms) and is called a seam of crossing (SX). In SX characterization, the energy minimum within the seam, known as the minimum-energy seam of crossing (MESX), can be considered as a representative point.[7]

Sampling all energetically accessible MESX structures is important in understanding ISC pathways and phosphorescence abilities. However, completion of all important MESX structures is not trivial because their geometries may not resemble the stable geometries of molecules.[8,9] We have developed a method for automated and systematic exploration of MESX structures by the single-component artificial-force-induced reaction (SC-AFIR) method.[10] Originally, a method that combined SC-AFIR with the seam model function (SMF/SC-AFIR) was developed. Systematic searches of minimum-energy conical intersection (MECI) structures, at which the same spin states (i.e., the ground S_0 and the lowest excited S_1 states) intersect, successfully identified energetically preferable nonradiative decay pathways, and the fluorescence quantum yields of aromatic compounds were investigated.[8,9] MESX structures can also be searched systematically by the SMF/SC-AFIR method, and the ISC pathways from the triplet metal-to-ligand charge-transfer state and reactivity on photochemical ligand substitution in tricarbonyl–Re(I) complexes have been studied.[11] The SMF/SC-AFIR method has been successful but it performs the geometry optimization calculation with a seam model function (a penalty function) and gives an approximate MESX/MECI geometry. The approximate MESX/MECI geometry gives a good estimation of the true MESX/MECI structure, but further optimization calculations with a conventional MESX/MECI optimization method are needed. In

addition, convergence of geometry optimization is slow in the SMF.[12] Recently, the gradient projection (GP) method, which is a conventional MESX/MECI optimization method,[13] has been combined with the SC-AFIR method instead of the SMF method.[12] A search by the GP/SC-AFIR method gives true MESX/MECI structures (the additional optimization steps from the approximate MESXs/MECIs are no longer needed) and the MESX/MECI structures are more reliably converged; therefore the efficiency of the automated investigation is improved. [12,14,15]

A number of studies of nonradiative relaxation pathways have been conducted by the SMF/SC-AFIR or GP/SC-AFIR method. All the studies considered isolated molecules in a vacuum or in a model solvent [as a polarizable continuum model (PCM)]. In electroluminescent devices, however, functional molecules often exist in the solid state as polymers or crystals. In general, intermolecular interactions or steric hindrance between the reactant and adjacent molecules may lead to different reactions. Several theoretical approaches for solution or solid-state studies have been reported[16-18]; nonradiative decay pathways have been examined by MECI/MESX calculations in association with the ONIOM (quantum mechanics/molecular mechanics [QM/MM]) method.[19-21] The QM/MM approach has been successful, but quantum chemistry calculations using periodic boundary conditions (PBCs) have also been widely used as an alternative approach to the computation of material properties. Here, a search for MESX structures by quantum chemistry calculations of a molecular crystal using PBCs was designed. Recently, we combined the SC-AFIR method with PBCs and performed a global search for low-lying crystal structures of carbon.[22] In this study, a systematic search for low-lying MESX structures between the lowest triplet excited state (T_1) and the singlet ground state (S_0) in a benzene crystal was performed by the GP/SC-AFIR method, and the ISC pathways were investigated. The $T_1 \rightarrow S_0$ nonradiative transition in benzene has been studied experimentally[23-27] and theoretically[28-37] in past decades, but this study is believed to be the first report of MESX structures in the benzene crystal.

6-2. COMPUTATIONAL METHODS

6-2-1. The overall reaction rate constant

The overall reaction rate constant $k'_{A\to C}$, based on the steady-state approximation (transition-state theory), is

$$k'_{A\to C} = \frac{k_{A\to B}\cdot k_{B\to C}}{k_{A\to B}+k_{B\to A}+k_{B\to C}} \quad (1)$$

$$k_{i\to j} = \frac{k_B\cdot T}{\hbar}\exp\left(\frac{\Delta E_{i\to j}}{RT}\right), \quad (2)$$

and the overall energy barrier $\Delta E'_{A\to C}$ can be calculated as

$$\Delta E'_{A\to C} \approx -\ln\left(\frac{\hbar}{k_B\cdot T}k'_{A\to C}\right)RT, \quad (3)$$

where R is the gas constant, T is the temperature, k_B is the Boltzmann constant, and $\hbar$ is the reduced Planck constant.

6-2-1. PBC/AFIR methods

In this study, PBCs were used to describe a molecular crystal as a three-dimensional periodic system. As described in our previous paper,[22] three Cartesian coordinates of each translation vector (TV) were considered as variables, as well as those of each atom. In the case of the crystal, geometrical displacements were therefore invoked in $(3N + 3)$-dimensional hyperspaces, and the MESX was located at the $(3N + 2)$-dimensional seams (where N is the number of atoms).

6-2-2. Electronic structure calculation

All calculations were performed with a developmental version of the GRRM program[38]. In the GRRM program, the SIESTA 3.2 program[39] was used to compute the energy, force acting on atoms, and stress tensor acting on a unit cell for each structure. These calculations were performed using density functional theory (DFT) with the Perdew–Burke–Ernzerhof (PBE) functional[40] and the DZP basis set[41].

Grimme's dispersion correction, with the parameters C_6 = 1.75 J nm^6 mol^{-1} and R_0 = 1.452 Å for a carbon atom, and C_6 = 0.14 J nm^6 mol^{-1} and R_0 = 1.001 Å for a hydrogen atom, was added.[42] The pseudopotentials were prepared using parameters in the GGA pseudopotential database.[43] The Fermi–Dirac electronic temperature was set at 100.0 K. The mesh cutoff value was set at 150.0 Ry. The Monkhorst–Pack (MP) grid for the *k*-point sampling was set at 4 × 4 × 4, including the Γ point. An isolated benzene molecule was computed as a slab model, in which a benzene molecule was put in a 20 × 20 × 20 Å^3 unit cell. The MP grid was set at 1 × 1 × 1 (the Γ point only).

6-2-3. Computational procedures

The concrete procedure in this study of searching for carbon crystal structures and the reaction pathway between systems proceeds along the following four steps.

(a) Optimize the benzene (C_6H_6) phase I taken from the literature[44] in the singlet ground (S_0) state. Here, the obtained global-minimum structure is labeled as S_0-MIN.

(b) Starting from S_0-MIN, the minimum-energy structure in the lowest triplet (T_1) state was fully optimized. The optimized structure of the T_1 state is denoted by T_1-MIN. The electronic structure of the T_1 state of the benzene crystal is discussed in **APPENDIX**.

(c) The MESX structures between the T_1 and S_0 states (S_0/T_1-MESXs) were systematically searchd by the GP/SC-AFIR method[12], around T_1-MIN.

(d) From each S_0/T_1-MESX point, a meta-IRC (intrinsic reaction coordinate) calculation (a mass-weighted steepest descent path calculation starting from a non-stationary point)[45,46] was performed in the T_1 state.

(e) The approximate TS geometries between the terminal point of the meta-IRC (T_1-MIN′) and T_1-MIN were searched by the double-sphere AFIR (DS-AFIR) method[15]. If the meta-IRC converges to a structure identical to T_1-MIN, this confirms that no transition state (TS) exists along a coordinate that links the S_0/T_1-MESX and T_1-MIN.

(f) TS geometry is optimized from that of the approximate TS which is relaxed by the locally updated planes (LUP) method.[47] In this study, the lowest-energy approximate TSs were only screened to optimize the exact TSs.

(g) A subsequent IRC calculation from the obtained TS confirms the connectivity between T_1-MIN and T_1-MIN′. In these IRC and meta-IRC calculations, the atomic mass of the TV was assumed to be 300 amu (15 times as heavy as a carbon atom).

6-3. RESULTS AND DISCUSSION

6-3-1. S_0/T_1-MESX structures and ISC pathways for benzene crystal

The S_0/T_1-MESX structures were systematically explored by the GP/SC-AFIR method, around the T_1-MIN structure. The electronic state of T_1-MIN is confirmed in **APPENDIX**.

The 39 independent S_0/T_1-MESX structures were found by the GP/SC-AFIR systematic search. The energies of the 39 obtained S_0/T_1-MESX structures are listed in **appendix**. The calculation required 14567 and 3872 gradient computations for each electronic state in the intramolecular and intermolecular SC-AFIR procedures, respectively. These S_0/T_1-MESX structures were categorized into five groups: intermolecular C–C-bonded type (**SX1**–**SX4**), intermolecular H-atom-transferred type (**SX5**–**SX14**, **SX18**, **SX19**), out-of-plane bent C–H type (**SX15**–**SX17**, **SX20**–**SX27**), benzvalene (out-of-plane bent C–C–C) type (**SX28**–**SX38**), and broken-ring type (**SX39**), in ascending order of electronic energy. The lowest-energy S_0/T_1-MESX structure of each type (**SX1**, **SX5**, **SX15**, **SX28**, **SX39**) are shown in **Fig. 6-1**. The latter three types were similar to the S_0/T_1-MESX structures of the isolated benzene molecule, and the former two were distinctive structures in which chemical bond rearrangement occurred between two adjacent benzene molecules.

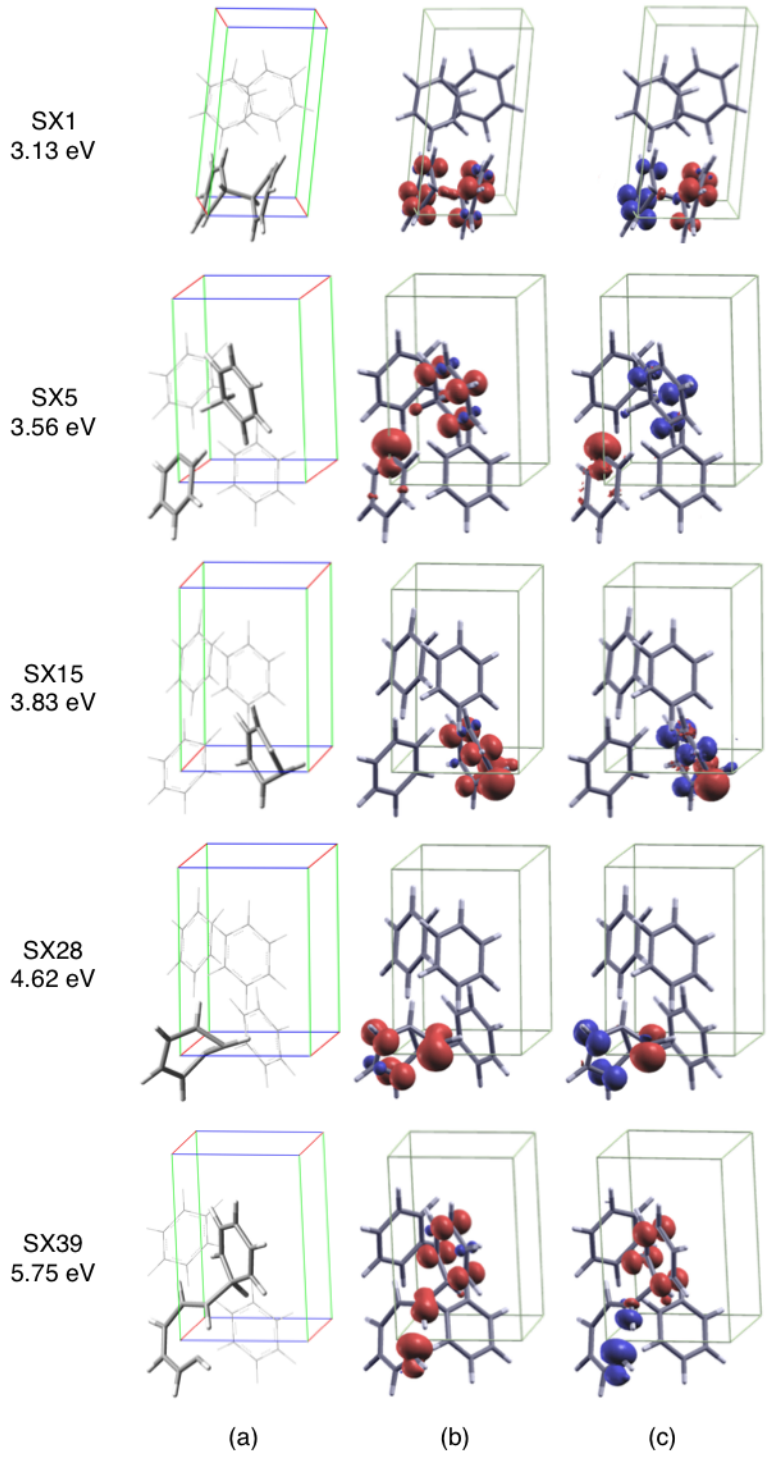

Figure 6-1. Lowest-energy S_0/T_1-MESX structure of intermolecular C–C-bonded type (**SX1**), intermolecular H-atom-transferred type (**SX5**), out-of-plane bent C–H type (**SX15**), benzvalene (out-of-plane bent C–C–C) type (**SX28**), and broken-ring type (**SX39**) in benzene crystal. (a) Molecules in which exciton was localized are highlighted,

(b) spin density difference between α and β spins for T_1 state, (c) spin density difference between α and β spins for S_0 state. The non-zero spin density difference in the S_0 state indicates open-shell singlet state was computed. For clarity, some molecules were translated to equivalent positions by the translational symmetry of the crystal, in the cases of **SX1**, **SX5**, and **SX39**.

The four lowest-energy S_0/T_1-MESX structures (**SX1**–**SX4**) were intermolecular C–C-bonded type, and their energies were lower than those of T_1-MIN. For these S_0/T_1-MESXs, the exciton was delocalized over a benzene complex and the T_1 and S_0 states were diradical-type states (the S_0 state was an open-shell singlet state, as discussed in **APPENDIX**). In addition, each of these S_0/T_1-MESXs was located close to the potential minimum of the diradical-type T_1 state, in which an intermolecular C–C bond exists ($MIN_{C–C\_bonded}$); therefore the meta-IRC in the T_1 state immediately converged to $MIN_{C–C\_bonded}$. The $MIN_{C–C\_bonded}$ structure differed from that of T_1-MIN; subsequent DS-AFIR calculations were performed to determine the (approximate) TSs on the reaction pathways to these S_0/T_1-MESX structures. The energies of the approximate TSs, obtained by DS-AFIR calculations, were 4.38, 3.91, 3.82, and 3.82 eV for **SX1**, **SX2**, **SX3**, and **SX4**, respectively (see **APPENDIX**). This indicates that **SX3** had the lowest-energy TS on the path from T_1-MIN, although **SX1** was the lowest-energy structure among the intermolecular C–C-bonded type S_0/T_1-MESX structures. The most stable **SX1** had the largest barrier because the reaction path to **SX1** was long (the path length was 13.17 Å) and large displacements of benzene molecules were required in the path. In contrast, the pathway to **SX3** was relatively short (7.07 Å) and it had the lowest-energy TS. It should be emphasized that the S_0/T_1-MESX that can be reached from T_1-MIN through a low energy barrier was important in ISC. **SX3** was the most important structure among **SX1**–**SX4**. It should be noted that the meta-IRC calculations for the S_0 state from each S_0/T_1-MESX point confirm that the S_0 potential energy surface was downhill to the S_0-MIN structure, where the S_0 state was a closed-shell singlet state. The excited benzene crystal can therefore return to the initial ground state structure through these intermolecular C–C-bonded type S_0/T_1-MESXs.

Fig. 6-2 summarizes the T_1 potential energy profile toward the S_0/T_1-MESX structures. These reaction routes correspond to the ISC pathways because S_0/T_1-MESX is the critical point at which the nonadiabatic transition effectively occurs. For simplicity, only the lowest-energy pathways to the intermolecular C–C-bonded type,

intermolecular H-atom-transferred type, and out-of-plane bent C–H type S_0/T_1-MESX structures are shown. The benzvalene type and broken-ring type S_0/T_1-MESX structures were located at high energies (>1 eV above T_1-MIN) and are omitted here. As discussed above, **SX3** was the most important structure of the intermolecular C–C-bonded type S_0/T_1-MESX.

For the same reason, **SX8** was used as the representative structure for the intermolecular H-atom-transferred type S_0/T_1-MESXs (**SX5**–**SX14**, **SX18**, **SX19**) instead of the lowest-energy **SX5**. In terms of the reaction coordinate, **SX3** and **SX8** were far from T_1-MIN because they required chemical bond rearrangements between two adjacent benzene molecules via the TSs. In contrast, almost all of the out-of-plane bent C–H type S_0/T_1-MESX structures were located close to T_1-MIN. The meta-IRC calculations for the T_1 surface showed that the out-of-plane bent C–H type S_0/T_1-MESX structures (except **SX15**) were directly connected to T_1-MIN, without any TSs. From **SX15** the T_1 meta-IRC converged to a different T_1 minimum structure ($MIN_{bent\_C–H}$, at 3.60 eV) in which a C–H bond was bent. The subsequent DS-AFIR calculation gave a small barrier $TS_{bent\_C–H}$ (at 3.63 eV), which connects $MIN_{bent\_C–H}$ and T_1-MIN. Our investigation showed that $MIN_{bent\_C–H}$ was also located on the path to **SX3** (with the intermolecular C–C-bonded type S_0/T_1-MESX structure). The DS-AFIR calculation for the pathway between T_1-MIN and $MIN_{C–C\_bonded}$ (which is the terminal point of the T_1 meta-IRC from **SX3**) showed two TSs along the reaction coordinate, and the first TS and intermediate minimum structure were identical to $TS_{bent\_C–H}$ and $MIN_{bent\_C–H}$, respectively. The energies of $TS_{C–C\_bonded}$ (3.81 eV) and **SX15** (3.83 eV) were almost same; therefore the ISC pathway through **SX3** (via $TS_{C–C\_bonded}$) and that through **SX15** could compete. The $TS_{C–C\_bonded}$ had the lowest energy barrier; therefore this reaction path could be the most important in the mechanism of the ISC process in the benzene crystal. **SX8** (the intermolecular H-atom-transferred type S_0/T_1-MESX) also had energy barriers from T_1-MIN; the lowest TS among them was $TS_{H\_transfer}$ (3.96 eV) and this reaction pathway was different from that to **SX3** or **SX15**. The $TS_{H\_transfer}$ energy was more than 0.1 eV higher than those for $TS_{C–C\_bonded}$ (3.81 eV) and **SX15** (3.83 eV); therefore this ISC pathway could be a minor route. This minor ISC route would compete with the ISC pathways through the out-of-plane bent C–H type S_0/T_1-MESXs (except **SX15**), because the lowest-energy **SX16** was located at 3.96 eV, without energy barriers.

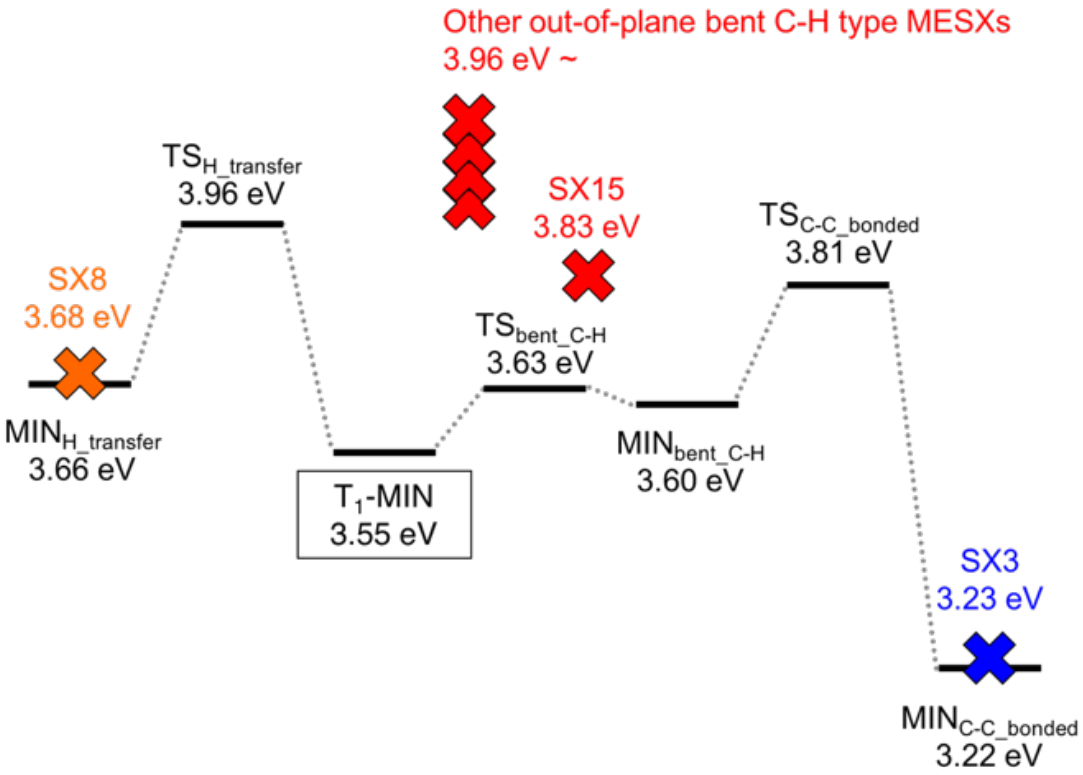

Figure 6-2. Potential energy profile of ISC pathways from lowest triplet state (T_1-MIN). Low-lying S_0/T_1-MESX structures are indicated by X mark. Note that all meta-IRC calculations for the S_0 state starting from these S_0/T_1-MESXs converged to S_0-MIN.

We estimated the rate constants for formation of the S_0/T_1-MESX structures for the most important reaction pathways from T_1-MIN to **SX3** or **SX15** via the intermediate T_1 minimum ($MIN_{bent\_C–H}$):

$$T_1\text{-MIN (A)} \rightleftarrows MIN_{bent\_C–H} \text{ (B)} \rightarrow \textbf{SX3} \text{ or } \textbf{SX15} \text{ (C)}. \quad (4)$$

The calculated overall energy barrier to **SX3** was 0.26 eV, and the rate constant of the reaction was estimated to be 5.07×10^8 s^{-1} (at 273 K) or 9.73×10^{-5} s^{-1} (at 77 K). In the same way, the overall energy barrier to **SX15** was 0.27 eV, and the rate constant was 2.17×10^8 s^{-1} (at 273 K) or 4.78×10^{-6} s^{-1} (at 77 K). At high temperature (273 K), the reaction rates are large enough ($<10^8$ s^{-1}) for ISC to occur at the S_0/T_1-MESX points. In contrast, the reaction rates at low temperature (77 K) become small ($<10^{-6}$ s^{-1}). Then T_1-MIN survives long enough for phosphorescence to compete with ISC. The rate constants were of the same order of magnitude as the reported theoretical ISC rates of 9.04×10^{-5} s^{-1} (Burland and Robinson)[29] and 7.4×10^{-4} s^{-1} (Fisher and Schneider).[31] However, they were smaller than the experimentally estimated nonradiative decay rates of 2.38×10^{-2} s^{-1} (at 4.2 K, in rare-gas matrices)[24] and 0.12 s^{-1} (at 77 K, in liquid glasses).[27] The results differ from those from the theoretical models in refs. 29 and 31 because those models neglected anharmonicity of the potential, but in this study such harmonic potential models were never used and the anharmonicity was taken into account in terms of molecular deformations (especially for the MESX structures). At 77 K, the rate constant, 0.12 s^{-1}, corresponds to an energy barrier of 0.21 eV in equation (5), and the difference between the barrier and calculated barrier in this study (0.26–0.27 eV) is just 0.05–0.06 eV; the error is within the chemical accuracy (~1 kcal mol^{-1}) of potential energies. The error might therefore arise from the DFT calculations. Another possible reason for the difference is that we assumed that ISC can occur when a molecule reaches the MESX point; ISC might occur in the S_0/T_1 crossing seam region where the two potential surfaces nearly degenerate over a wide range of geometries and the coupling is relatively strong (not only at the minimum point).[48,49] Such phenomena could accelerate ISC. In addition, the experimental rate constants were observed in rare-gas matrices or in liquid glasses, not in a pure benzene crystal. We therefore can compare these experimental values with the rate constant for **SX15** rather than **SX3**, because in rare-gas matrices or in liquid grasses each benzene molecule is likely to be isolated from the other benzene molecules. To further examine the ISC pathways

through the intermolecular-type MESXs, experimental efforts to measure the ISC rate in a pure benzene crystal will be required. The goal of theoretical chemistry is not only to reproduce experimental results but also to provide general relationships and correlations. Here, we propose a procedure for systematically searching for S_0/T_1-MESX structures in a crystalline environment, and for screening the most important pathways. In this context, further studies of molecular crystals are needed.

6-4. CONCLUSIONS

In this study, the ISC pathways of an excited benzene crystal were investigated through theoretical calculations. The GP/SC-AFIR method was used to systematically search for low-lying S_0/T_1-MESX structures, and quantum chemistry calculations with PBCs were used to describe the molecular crystal system.

The results of the systematic search for S_0/T_1-MESX structures of the benzene crystal were discussed. For the stationary structure in the first triplet state, or T_1-MIN, the exciton was localized on a benzene molecule. The S_0/T_1-MESX structures in the crystal basically resembled those of the isolated molecule; out-of-plane bent C–H type, benzvalene type, and broken-ring type S_0/T_1-MESX structures were observed under both isolated and crystalline conditions. Intermolecular C–C-bonded type and intermolecular H-atom-transferred type S_0/T_1-MESXs were characteristic structures of the crystal and they were more stable than the other S_0/T_1-MESX structures. Finally, for the benzene crystal, a GP/SC-AFIR systematic search identified 39 independent S_0/T_1-MESX structures.

The intermolecular C–C-bonded type S_0/T_1-MESX was the lowest-energy structure among all the MESXs; however, such S_0/T_1-MESX structures were located far from T_1-MIN in terms of the reaction coordinate and some energy barriers existed because chemical bond rearrangements between two adjacent benzene molecules via TSs were required. The lowest-energy TS ($TS_{C–C\_bonded}$) between the intermolecular C–C-bonded type S_0/T_1-MESX (**SX3**) and T_1-MIN was found at 3.81 eV. This $TS_{C–C\_bonded}$ structure had the lowest energy barrier; therefore **SX3** and this reaction path could be the most important in the mechanism of the ISC process in the benzene crystal. Our calculations also showed that the reaction path to **SX3** through $TS_{C–C\_bonded}$ (3.81 eV) could compete with the pathway to **SX15** (3.83 eV), the intramolecular out-of-plane bent C–H type S_0/T_1-MESX structure. Transition-state theory and the steady-state approximation were used to calculate the overall energy barriers to **SX3** and **SX15** from T_1-MIN, namely 0.26 and 0.27 eV, respectively. The rate constants for **SX3** and **SX15** formation were estimated to be 5.07×10^8 and 2.17×10^8 s^{-1} (at 273 K), respectively, or 9.73×10^{-5} and 4.78×10^{-6} s^{-1} (at 77 K), respectively, i.e., the upper limits of the ISC rate constants through the S_0/T_1-MESX. At 273 K, close to the benzene crystal melting point (278.5 K), **SX3** and **SX15** are easily accessible from T_1-MIN because the reaction rates are fast enough ($<10^8$ s^{-1}) for ISC to occur through the S_0/T_1-MESX points. In

contrast, at 77 K, the rate constants become small ($<10^{-6}$ s^{-1}) and T_1-MIN survives long enough for phosphorescence to compete with ISC.

6-5. APPENDIX

The results of the GP/SC-AFIR search for the S_0/T_1-MESXs of the isolated benzene molecule (constructed as a slab model) were reported as preliminary results to those for the crystal system, and we discussed how the computational level of theory used in this study works. The unit-cell size dependence of the electronic structure of the benzene crystal was evaluated. The primitive unit cell (Z = 4) and three types of extended unit cell models (Z = 8) were considered; however, almost no differences among the electronic structures and energies were observed. The primitive cell (Z = 4) was therefore used as the unit cell in subsequent computations.

A6-1. S_0/T_1-MESX structures and ISC pathways for isolated benzene molecule

The benzene molecule has the D_{6h} symmetry structure in the S_0 state (S_0-MIN), and in the T_1 state the D_{6h} symmetry is lowered to D_{2h} symmetry (T_1-MIN). The calculated T_1-S_0 vertical excitation energy of the S_0-MIN structure was 3.87 eV, which is in good agreement with the experimental value (3.95 eV),[50] since the PBE functional systematically underestimates the energy of the excited state.[51] The optimized T_1-MIN structure corresponded to the anti-quinoid structure,[37][52,53] in which the bond lengths $r_{C–C}$ (long), $r_{C–C}$ (short), and $r_{C–H}$ were 1.53, 1.41, and 1.11 Å, respectively, and the energy relative to S_0-MIN was 3.69 eV. The GP/SC-AFIR systematic search found nine S_0/T_1-MESX structures around the T_1-MIN structure of the isolated benzene molecule. **Fig. A6-1** shows all the S_0/T_1-MESX structures in ascending order of electronic energy. At T_1-MIN, the benzene molecule had the D_{2h} symmetry and structure. These S_0/T_1-MESXs were categorized into four groups: out-of-plane bent C–H type (**SX1**^{iso}, **SX3**^{iso}), intramolecular H-atom-transferred type (**SX2**^{iso}), benzvalene (out-of-plane bent C–C–C) type (**SX4**^{iso}, **SX5**^{iso}), and broken-ring type (**SX6**^{iso}– **SX9**^{iso}). The lowest-energy S_0/T_1-MESX, **SX1**^{iso}, is an artifact in which the T_1 state accidentally crosses the closed-shell electronic ground state; for the **SX1**^{iso} geometry, the closed-shell singlet state (3.74 eV) was unstable with respect to the open-shell singlet state (3.51 eV). Such a singlet instability was checked by restricted and unrestricted CCSD calculations with the Gaussian 09 program.[54] The closed-shell singlet wavefunction converged at 3.77 eV for the **SX1**^{iso} geometry, but the open-shell singlet wavefunction converged at 3.52 eV for the same geometry. It was also

confirmed that **SX3^{iso}** in our GP/SC-AFIR search was the open-shell singlet/triplet crossing point. Plots of the spin density differences between α and β spins are shown in **Fig. A6-2**. There was no isosurface to plot in the closed-shell singlet state, but the open-shell singlet wavefunction indicated non-zero spin densities even in the singlet state. In this study, to evaluate such singlet instabilities in the S_0/T_1-MESX structure, we checked the spin difference density in the S_0 state. Here, only the **SX1^{iso}** structure was rejected from the list, because of its instability.

The lowest-energy S_0/T_1-MESX, **SX2^{iso}**, was located at only 0.10 eV above T_1-MIN, but there was a large energy barrier (about 1.5 eV) between T_1-MIN and **SX2^{iso}** because a H atom must be transferred to the next carbon atom in the pathway. The second-lowest-energy S_0/T_1-MESX, **SX3^{iso}**, was located 0.33 eV above T_1-MIN and there was no TS between T_1-MIN and **SX3^{iso}**. The ISC pathway via the second-lowest-energy **SX3^{iso}** is therefore favored rather than that via the lowest-energy structure, **SX2^{iso}**. The molecular structure of **SX3^{iso}** is in good agreement with the previously reported S_0/T_1-MESX structure (**Fig. A6-3**). [13]

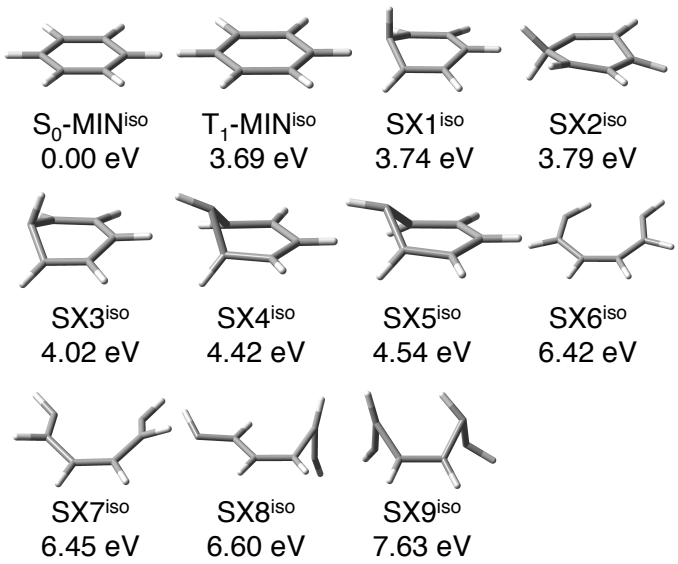

Figure A6-1. S_0/T_1-MESX structures obtained by GP/SC-AFIR search of isolated benzene molecule.

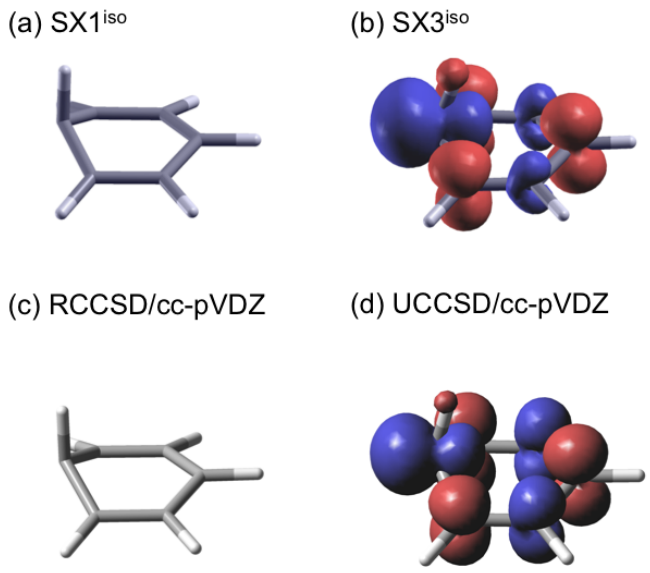

Figure A6-2. Plots of spin density differences between α and β spins for S_0 state for (a) **SX1**^{iso} and (b) **SX3**^{iso}, which were obtained by GP/SC-AFIR search using SIESTA program; (c) optimized S_0/T_1-MESX structure obtained at RCCSD/cc-pVDZ level of theory and (d) optimized S_0/T_1-MESX structure obtained at UCCSD/cc-pVDZ level of theory, computed with Gaussian 09 program. In these S_0/T_1-MESX structures, the closed-shell singlet wavefunction (a and c) was unstable.

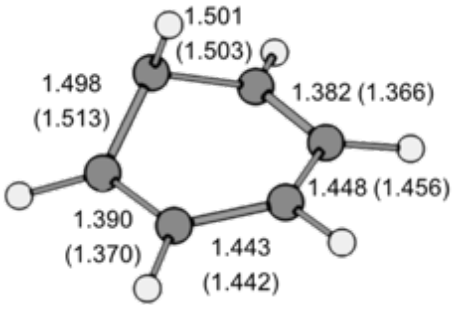

Figure A6-3. Optimized geometry of **SX3**^{iso} compared with that of S_0/T_1-MESX structure (at the CAS(6,6)/4-31G level) reported in Ref. 13. Figures in parentheses are values reported in Ref. 13.

A6-2. Molecular geometries and electronic states of benzene crystal

The S_0-MIN structure of the benzene crystal was obtained by geometry optimization; the optimization was initiated from the X-ray crystallographic structure data for the benzene (phase I) crystal.[44] The experimentally resolved primitive unit cell contained four benzene molecules (Z = 4), and the unit-cell size dependence of the electronic structure was carefully examined. Four models were prepared: the original size (Z = 4, model **I**), and double-sized unit cells along the a (Z = 8, model **II**), b (Z = 8, model **III**), or c (Z = 8, model **IV**) vector. If model **I** (Z = 4) is insufficient to describe the energy-minimum structure, the geometry optimization calculation leads to a different S_0-MIN structure from those for models **II**–**IV**, and the energy differences among these models may not be negligible. **Table A6-1** lists the electronic energies of the S_0 state for the S_0-MIN structure for models **I**–**IV**; the maximum energy difference was less than 0.01 eV. This result clearly shows that all these models converged to the same S_0-MIN structure. Model **I** (Z = 4) can therefore reasonably describe the molecular geometry and electronic structure for the ground state. The molecular structure of S_0-MIN in model **I** is shown in **Fig. A6-4 (a)**. In the S_0-MIN structure, all four benzenes are symmetrically equivalent to each other because the unit cell belongs to the *Pbca* space group (D_{2h} point group in Shönflies notation).

Table A6-1. Electronic energies of ground states (S_0) for S_0-MIN structures in models **I**–**IV**.

Model	E(S_0) / hartree	Difference[a] / eV
I: Z = 4	−314.881353721016[b]	0
II: Z = 8 (along a vector)	−314.881003536864	9.53×10^{-3}
III: Z = 8 (along b vector)	−314.881356624211	-7.90×10^{-5}
IV: Z = 8 (along c vector)	−314.881087619280	7.24×10^{-3}

[a] Energy difference from model **I** (Z = 4).

[b] Energy value per eight benzene molecules (the calculated energy was doubled).

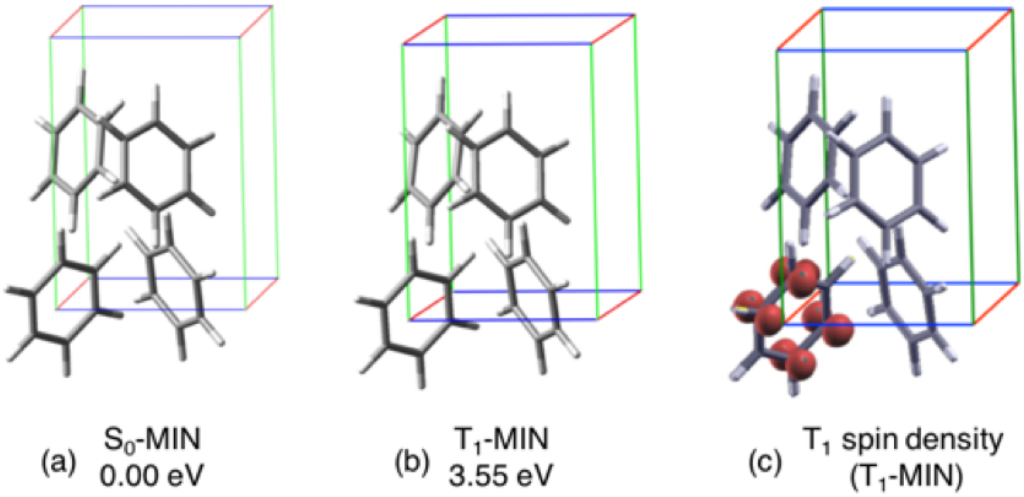

Figure A6-4. Optimized structure for (a) S_0 state (S_0-MIN) and (b) T_1 state (T_1-MIN), and (c) calculated spin density difference between α and β spins in T_1 state for T_1-MIN structure (for model **I**, $Z = 4$).

The unit-cell size dependence of the electronic structure was also examined for the T_1 state. For each model **I**–**IV**, the T_1-MIN structure was optimized starting from the S_0-MIN structure. **Fig. A6-4 (b)** and **Fig. A6-4 (c)** show the T_1-MIN structure and spin density difference, respectively, for model **I**. For T_1-MIN in every model, the calculated spin density difference between the α and β spins was located on a benzene molecule, and the unit cell consisted of four or eight benzene molecules. An electronically excited benzene molecule in the T_1 state was surrounded by benzene molecules in the S_0 state, and an exciton was not spread over two adjacent molecules. Using model **I**, it is assumed that 25% of benzene molecules in the crystal are electronically excited in the T_1-MIN structure. This situation resembles a high-density coherent excitation of the crystal and seems unrealistic. However, **Table A6-2** shows the electronic energies of the excited (T_1) and ground (S_0) states for the T_1-MIN structure for each model **I**–**IV**, and there are almost no energy differences among these models. In addition, the exciton was localized on a benzene molecule in each model. This result implies no significant interactions between excitons in the system, and model **I** can describe a realistic benzene crystal. In this study, the primitive unit cell ($Z = 4$) was therefore used in all calculations.

Table A6-2. Electronic energies of excited (T_1) and ground (S_0) states for T_1-MIN structures in each model **I**–**IV**.

Model	$E(T_1)$ / hartree	$E(S_0)$ / hartree	$\Delta E(T_1\text{-}S_0)$ / eV
I: $Z = 4$	−157.310048763759	−157.422172885868	3.051
II: $Z = 8$ (along *a* vector)	−314.750725293523	−314.863510572427	3.069
III: $Z = 8$ (along *b* vector)	−314.750471429306	−314.862623591137	3.051
IV: $Z = 8$ (along *c* vector)	−314.750440339392	−314.862852759820	3.059

As in the case of T_1-MIN of the isolated molecule (see section III.A), the excited benzene molecule in the T_1-MIN crystal took the anti-quinoide structure. The bond lengths $r_{C–C}$ (long), $r_{C–C}$ (short), and $r_{C–H}$ were 1.52, 1.40, and 1.10 Å, respectively. The energy of T_1-MIN relative to that of S_0-MIN was 3.55 eV. This is in good agreement with the literature value, which is 3.68 eV for benzene crystals,[55] considering that the PBE functional systematically underestimates the energy of the excited state.[51] Compared with the isolated benzene case, the T_1 state energy was stabilized by 0.14 eV in the crystalline environment. This might arise from dipole and induced-dipole interactions between the benzene molecules in the T_1 and S_0 states; however, we did not explore this point further.

A6-3. Energies of 39 S_0/T_1-MESX structures obtained by GP/SC-AFIR search

Table A6-3. Energies of 39 S_0/T_1-MESX structures obtained by GP/SC-AFIR search in benzene crystal. Energies of TSs between each S_0/T_1-MESX and T_1-MIN are also listed. Energy values in parentheses are approximate TSs (top point of LUP path), and the lowest-energy structures among the approximate TSs for each type of S_0/T_1-MESXs were selected and optimized to give accurate TSs.

	E (SX) / eV	E (TS) / eV		E (SX) / eV	E (TS) / eV
SX1[a]	3.134	(4.387)	**SX21**[c]	4.103	4.103[†]
SX2[a]	3.152	(3.905)	**SX22**[c]	4.103	4.103[†]
SX3[a]	3.226	3.806 (3.816)	**SX23**[c]	4.106	4.106[†]
SX4[a]	3.229	(3.822)	**SX24**[c]	4.192	4.192[†]
SX5[b]	3.557	(4.904)	**SX25**[c]	4.194	4.194[†]
SX6[b]	3.649	(4.194)	**SX26**[c]	4.195	4.195[†]
SX7[b]	3.679	(4.621)	**SX27**[c]	4.219	4.219[†]
SX8[b]	3.680	3.962 (3.927)	**SX28**[d]	4.621	(4.815)
SX9[b]	3.680	(4.193)	**SX29**[d]	4.625	(4.821)
SX10[b]	3.707	(5.044)	**SX30**[d]	4.637	(4.745)
SX11[b]	3.711	(5.071)	**SX31**[d]	4.644	(4.730)
SX12[b]	3.753	(4.188)	**SX32**[d]	4.761	(4.831)
SX13[b]	3.763	(4.215)	**SX33**[d]	4.762	(4.791)
SX14[b]	3.783	(4.850)	**SX34**[d]	4.843	(4.843)
SX15[c]	3.827	3.634 (3.649)	**SX35**[d]	4.846	(4.846)

SX16[c]	3.960	3.960[†]	**SX36**[d]	4.877	(4.896)
SX17[c]	3.961	3.961[†]	**SX37**[d]	4.895	(4.904)
SX18[b]	3.966	(4.324)	**SX38**[d]	4.923	(4.925)
SX19[b]	4.001	(4.292)	**SX39**[e]	5.754	(6.120)
SX20[c]	4.042	4.042[†]			

[a]Intermolecular C–C-bonded type. [b]Intermolecular H-atom-transferred type. [c]Out-of-plane bent C–H type. [d] Benzvalene (out-of-plane bent C–C–C) type. [e]Broken-ring type.

[†]No TS was found between T_1-MIN and S_0/T_1-MESX; therefore the energy of S_0/T_1-MESX was regarded as the potential barrier.

A6-4. The gradient difference vectors (GDV) between the T_1 and S_0 potential energy surfaces

Table A6-4 lists the norms of the gradient difference vectors (GDV) between the T_1 and S_0 potential energy surfaces for each of the low-lying S_0/T_1-MESX structures, and that for TVs were not trivial. This implies that the S_0/T_1-MESX energy might be overestimated if the lattice vectors were frozen during geometry optimization.

Table A6-4. Norms of gradient difference vectors between gradients of T_1 and S_0 surfaces for **SX1**, **SX5**, **SX15**, **SX28**, and **SX39**.

	Atoms	TVs
SX1	0.0424	0.0071
SX5	0.0653	0.0048
SX15	0.0709	0.0166
SX28	0.0776	0.0149
SX39	0.0571	0.0075

6-5. REFERENCE

[1] Z. He, W. Zhao, J. W. Y. Lam, Q. Peng, H. Ma, G. Liang, Z. Shuai, and B. Z. Tang, Nature Communications **8**, 416 (2017).

[2] H. Uoyama, K. Goushi, K. Shizu, H. Nomura, and C. Adachi, Nature **492**, 234 (2012).

[3] N. Koga and K. Morokuma, Chem. Phys. Lett. **119**, 371 (1985).

[4] F. Bernardi, M. Olivucci, and M. A. Robb, Chem. Soc. Rev. **25**, 321 (1996).

[5] D. R. Yarkony, J. Phys. Chem. A **103**, 6658 (1999).

[6] J. N. Harvey, Wiley Interdisciplinary Reviews-Computational Molecular Science **4**, 1 (2014).

[7] S. Maeda, K. Ohno, and K. Morokuma, J. Phys. Chem. A **113**, 1704 (2009).

[8] Y. Harabuchi, T. Taketsugu, and S. Maeda, Phys. Chem. Chem. Phys. **17**, 22561 (2015).

[9] Y. Harabuchi, T. Taketsugu, and S. Maeda, Chem. Lett. **45**, 940 (2016).

[10] S. Maeda, T. Taketsugu, and K. Morokuma, J. Comput. Chem. **35**, 166 (2014).

[11] K. Saita, Y. Harabuchi, T. Taketsugu, O. Ishitani, and S. Maeda, Phys. Chem. Chem. Phys. **18**, 17557 (2016).

[12] Y. Harabuchi, T. Taketsugu, and S. Maeda, Chem. Phys. Lett. **674**, 141 (2017).

[13] M. J. Bearpark, M. A. Robb, and H. B. Schlegel, Chem. Phys. Lett. **223**, 269 (1994).

[14] Y. Harabuchi, K. Saita, and S. Maeda, Photochemical & Photobiological Sciences **17**, 315 (2018).

[15] S. Maeda, Y. Harabuchi, M. Takagi, K. Saita, K. Suzuki, T. Ichino, Y. Sumiya, K. Sugiyama, and Y. Ono, J. Comput. Chem. **39**, 233 (2018).

[16] S. Ruiz-Barragan, K. Morokuma, and L. Blancafort, J. Chem. Theory Comput. **11**, 1585 (2015).

[17] X.-L. Peng, S. Ruiz-Barragan, Z.-S. Li, Q.-S. Li, and L. Blancafort, Journal of Materials Chemistry C **4**, 2802 (2016).

[18] M. Hatanaka, Y. Hirai, Y. Kitagawa, T. Nakanishi, Y. Hasegawa, and K. Morokuma, Chemical Science **8**, 423 (2017).

[19] L. W. Chung *et al.*, Chem. Rev. **115**, 5678 (2015).

[20] M. J. Bearpark, S. M. Larkin, and T. Vreven, J. Phys. Chem. A **112**, 7286 (2008).

[21] A. Bhattacharya and E. R. Bernstein, J. Phys. Chem. A **115**, 4135 (2011).

[22] M. Takagi, T. Taketsugu, H. Kino, Y. Tateyama, K. Terakura, and S. Maeda, Phys. Rev. B **95**, 184110 (2017).

[23] M. R. Wright, R. P. Frosch, and G. W. Robinson, J. Chem. Phys. **33**, 934 (1960).

[24] G. W. Robinson, J. Mol. Spectrosc. **6**, 58 (1961).

[25] T. E. Martin and A. H. Kalantar, J. Chem. Phys. **49**, 235 (1968).

[26] T. E. Martin and A. H. Kalantar, J. Chem. Phys. **48**, 4996 (1968).

[27] R. Li and E. C. Lim, J. Chem. Phys. **57**, 605 (1972).

[28] G. W. Robinson and R. P. Frosch, J. Chem. Phys. **38**, 1187 (1963).

[29] D. M. Burland and G. W. Robinson, J. Chem. Phys. **51**, 4548 (1969).

[30] B. R. Henry and W. Siebrand, J. Chem. Phys. **54**, 1072 (1971).

[31] S. Fischer and S. Schneider, Chem. Phys. Lett. **10**, 392 (1971).

[32] S. Fischer, Chem. Phys. Lett. **11**, 577 (1971).

[33] A. Nitzan and J. Jortner, Theor. Chim. Acta **30**, 217 (1973).

[34] B. Scharf, Chem. Phys. Lett. **68**, 242 (1979).

[35] W. Siebrand and M. Z. Zgierski, Chem. Phys. Lett. **72**, 411 (1980).

[36] O. S. Mortensen, W. Siebrand, and A. W. Tarr, Chem. Phys. **125**, 231 (1988).

[37] N. Zamstein, S. Kallush, and B. Segev, J. Chem. Phys. **123**, 074304 (2005).

[38] development version of GRRM.

[39] J. M. Soler, E. Artacho, J. D. Gale, A. García, J. Junquera, P. Ordejón, and D. Sánchez-Portal, J. Phys.: Condens. Matter 14, 2745 (2002); E. Artacho, J. M. Cela, J. D. Gale, A. García, J. Junquera, R. M. Martin, P. Ordejón, D. Sánchez-Portal, and J. M. Soler, SIESTA 3.2 , Fundación General Universidad Autónoma de Madrid, Spain, 2013,

see http://www.uam.es/siesta.

[40] J. P. Perdew, K. Burke, and M. Ernzerhof, Phys. Rev. Lett. **77**, 3865 (1996).

[41] D. SanchezPortal, E. Artacho, and J. M. Soler, Journal of Physics-Condensed Matter **8**, 3859 (1996).

[42] S. Grimme, J. Comput. Chem. **27**, 1787 (2006).

[43] GGA Pseudopotential Database, http://departments.icmab.es/leem/siesta/Databases/Pseudopotentials/periodictable-gga-abinit.html (Accessed accessed May 3, 2016).

[44] A. Katrusiak, M. Podsiadlo, and A. Budzianowski, Crystal Growth & Design **10**, 3461 (2010).

[45] K. Fukui, Acc. Chem. Res. **14**, 363 (1981).

[46] S. Maeda, Y. Harabuchi, Y. Ono, T. Taketsugu, and K. Morokuma, Int. J. Quantum Chem **115**, 258 (2015).

[47] C. Choi and R. Elber, J. Chem. Phys. **94**, 751 (1991).

[48] F. Sicilia, M. J. Bearpark, L. Blancafort, and M. A. Robb, Theor. Chem. Acc. **118**, 241 (2007).

[49] R. S. Minns, D. S. N. Parker, T. J. Penfold, G. A. Worth, and H. H. Fielding, Phys. Chem. Chem. Phys. **12**, 15607 (2010).

[50] J. P. Doering, J. Chem. Phys. **51**, 2866 (1969).

[51] J. M. Crowley, J. Tahir-Kheli, and W. A. Goddard, III, J. Phys. Chem. Lett. **7**, 1198 (2016).

[52] Y. Osamura, Chem. Phys. Lett. **145**, 541 (1988).

[53] G. Bergamini, A. Fermi, C. Botta, U. Giovanella, S. Di Motta, F. Negri, R. Peresutti, M. Gingras, and P. Ceroni, Journal of Materials Chemistry C **1**, 2717 (2013).

[54] M. J. Frisch, G. W. Trucks, H. B. Schlegel, G. E. Scuseria, M. A. Robb, J. R. Cheeseman, G. Scalmani, V. Barone, B. Mennucci, G. A. Petersson, H. Nakatsuji, M. Caricato, X. Li, H. P. Hratchian, A. F. Izmaylov, J. Bloino, G. Zheng, J. L. Sonnenberg, M. Hada, M. Ehara, K. Toyota, R. Fukuda, J. Hasegawa, M. Ishida, T. Nakajima, Y. Honda, O. Kitao, H. Nakai, T. Vreven, J. A. Montgomery, Jr., J. E. Peralta, F. Ogliaro, M. Bearpark, J. J. Heyd, E. Brothers, K. N. Kudin, V. N.

Staroverov, T. Keith, R. Kobayashi, J. Normand, K. Raghavachari, A. Rendell, J. C. Burant, S. S. Iyengar, J. Tomasi, M. Cossi, N. Rega, J. M. Millam, M. Klene, J. E. Knox, J. B. Cross, V. Bakken, C. Adamo, J. Jaramillo, R. Gomperts, R. E. Stratmann, O. Yazyev, A. J. Austin, R. Cammi, C. Pomelli, J. W. Ochterski, R. L. Martin, K. Morokuma, V. G. Zakrzewski, G. A. Voth, P. Salvador, J. J. Dannenberg, S. Dapprich, A. D. Daniels, O. Farkas, J. B. Foresman, J. V. Ortiz, J. Cioslowski and D. J. Fox, Gaussian 09, Revision D.01, Gaussian Inc., Wallingford CT, 2013.

[55] S. D. Colson and E. R. Bernstein, J. Chem. Phys. **43**, 2661 (1965).

Chapter 7.
General Conclusion

In this study, artificial force induced reaction (AFIR) method is extended to the periodic boundary conditions (PBCs) and its applications were performed.

In **Chapter 2**, I developed a new method for global search for low-lying crystal structures, by combining the artificial force induced reaction (AFIR) method and the periodic boundary conditions (PBCs). The AFIR method has been applied extensively to molecular systems to elucidate the mechanism of chemical reactions such as homogeneous catalysis. The present PBC/AFIR approach found 274 local minima for carbon crystals in the C_8/unit-cell described by the GGA/PBE functional. Among many newly predicted structures, three low-lying structures, which exhibit somewhat higher energy compared with those previously predicted, such as Cco-C_8 (*Z*-carbon) and *M*-carbon, are further discussed with calculations of phonon and band dispersion curves. Furthermore, approaches to systematically explore two- or one-dimensional periodic structures are proposed and applied to the C_8/unit-cell with the slab model. These results suggest that the present approach is highly promising for predicting crystal structures.

In **Chapter 3**, exhaustive search for small carbon crystal (C_1-C_{16}/unit-cell) by PBC/AFIR method were performed. As results, 14265 structural data of carbon crystal structures were generated and related poetries (sp^2/sp^3 ratio, density, band gap) were also calculated. The obtained structural data includes the previously reported structures. Moreover, even in carbon crystals that are well examined, many new structures were obtained. According to the energy distribution of the structures, efficient searches for low-lying structures were performed. By using this data list, interesting structures were found. By using this data list, some interesting structures were found with four search conditions based on properties. The vast amount of data obtained by this approach would be useful for materials informatics.

In **Chapter 4**, the phase transition network of C_4/unit-cell was generated by PBC/AFIR method. Even though such a small system, 95 local minima and 1087 transition states were obtained. The phase transition pathways from diamond were also discussed. The fastest decay path of diamond was diamond to graphite that was consistent with previous studies. In this framework, crystal structure search and phase transition pathway search are performed at the same time. Therefore it is able to apply this method to an unknown system. Any crystal phase transition such as heteroatoms or

molecular crystals could be treated by the same procedure.

In **Chapter 5**, the kinetic stability of the Cco-C_8 (or *Z*-carbon) that predicted theoretically by previous studies was discussed by PBC/AFIR methods. In such a small cell, there is cell shape dependence of decay paths. In this study, C_{16}-conv and its super cell C_{32}-conv has the lower energy pathways. The lifetime estimated by these pathways are 4.5 $\times 10^{20}$ [s] and these results indicate that Cco-C_8 will be kinetic stable, i.e. this structure might be synthesized. Note that there is a possibility that faster decay path exists in larger super-cells. As shown in this study, this approach can be discussed the kinetic stability of a material which predicted theoretically. The true lifetime of the material would be less than the lifetime estimated by targeted system because there is a possibility that it is exists that the faster decay path that could not described in targeted system. Therefore, it can be expected that it can be utilized as one of filters to estimate the lifetime of material.

In **Chapter 6**, the intersystem crossing (ISC) pathways of triplet benzene molecules in a benzene crystal were investigated theoretically. A combination of the gradient projection (GP) method, which is a standard method for optimizing the crossing seam of two potential energy surfaces, and the single-component artificial-force-induced reaction (SC-AFIR) method (GP/SC-AFIR) was used. This is the first reported use of a GP/SC-AFIR calculation using a density functional theory (DFT) calculation with periodic boundary conditions. A systematic search for the minimum-energy structures in the seams of crossing of the singlet (S_0) and triplet (T_1) potential energy surfaces (S_0/T_1-MESX structures) found 39 independent S_0/T_1-MESX structures. Energy barriers between the S_0/T_1-MESX and the stationary structure of the triplet state (T_1-MIN) were computed, and then two competing ISC pathways were extracted; the calculated overall energy barrier to the intermolecular C–C-bonded type (**SX3**) and the out-of-plane bent C–H type (**SX15**) S_0/T_1-MESX structures from T_1-MIN were 0.26 and 0.27 eV, respectively. The rate constants for **SX3** and **SX15** formation were estimated to be 5.07 $\times$ 10^8 and 2.17 $\times$ 10^8 s^{-1} (at 273 K), respectively, or 9.73 $\times$ 10^{-5} and 4.78 $\times$ 10^{-6} s^{-1} (at 77 K), respectively. At 273 K, which is close to the melting point of the benzene crystal (278.5 K), **SX3** and **SX15** are easily accessible from T_1-MIN, and ISC could occur through the S_0/T_1-MESX points. In contrast, at 77 K, T_1-MIN survives long enough for phosphorescence to compete with ISC.

In this study, I challenged to perform systematic crystal structure search and phase-transition path search. So, scientists who are not specialized in computational science will also be able to search for crystal structures and search for phase-transition paths by using this approach. Moreover, a discussion on material properties (kinetic stability, luminescence properties) that were difficult to discuss until now have been made possible by using this approach. For the purpose of an efficient material development, these approaches are expected to be become strong tools.

Acknowledgement

All the studies described in this dissertation were carried out under the supervision of Professor Satoshi Maeda, Department of Chemistry, Faculty of Science, Hokkaido University. I would like to express my acknowledgements to Professor Satoshi Maeda for his constant guidance, pertinent advice and helpful discussion.

Great acknowledgement is also made to Professor Tetsuya Taketsugu for his guidance and helpful discussion.

I would like to thank Assistant Professor Yu Harabuchi and Assistant Professor Kenichiro Saita for practical advice and helpful discussion.

I thank to Professor Toshihiro Shimada and Professor Jun-ya Hasegawa for serving my dissertation committee.

I thank you to Dr. Ryohei Uematsu for teaching me the basics of programming and researches.

I also thank you to Dr. Keisuke Niimi and Dr. Yusuke Kondo for teaching me the quantum chemistry.

I'm grateful to Ms. Kanami Sugiyama, Dr. Yosuke Sumiya, Dr. Masanori Ebina, Dr. Yusuke Kuroda, Dr. Yuriko Ono, and other members of Theoretical Chemistry Lab. and Quantum Chemistry Lab. for her/his encouragement.

I also thank to support by the Ministry of Education, Culture, Sports, Science and Technology through Program for Leading Graduate Schools (Hokkaido University "Ambitious Leader's Program") and JSPS Research Fellowships for Young Scientists (DC2).